U.PORTO
FEUP FACULDADE DE ENGENHARIA UNIVERSIDADE DO PORTO

inegi driving science & innovation

Mixed mode crack propagation:
Numerical and Experimental Study

Marco A. C. Ferreira

Dissertation submitted to
Faculdade de Engenharia da Universidade do Porto
for the degree of:

Mestre em Engenharia Mecânica

Advisor: Prof. Sérgio M. O. Tavares
Co-Advisor: Prof. Paulo M. S. Tavares de Castro

Departamento de Engenharia Mecânica
Faculdade de Engenharia da Universidade do Porto

Porto, 2017

The work presented in this dissertation was performed at the
Department of Mechanical Engineering
Faculty of Engineering
University of Porto
Porto, Portugal.

Marco A. C. Ferreira
E-mail: up201502893@fe.up.pt

Faculdade de Engenharia da Universidade do Porto
Departamento de Engenharia Mecânica
Rua Dr. Roberto Frias s/n
4200-465 Porto
Portugal

Abstract

The knowledged of the mechanical behavior of structures subjected to cyclic loading is a very important issue. It allows engineers to do a proper design, therefore the relevant mechanical properties and behavior must be well known and understood; This includes mixed-mode fracture mechanics problems.

The present research consists of a study about the path of fatigue crack propagation under mixed mode loading situations. Known geometries were modified to promote mode II crack propagation; the study involved numerical simulations which were compared with experimental results.

The aim of this study is to evaluate the capability of the extended finite element method to predict the crack propagation path under a mixed mode loading situation. All of the studied situations consist of plane mixed mode I-II. The extended finite element method was implemented on Abaqus software using the Paris law subroutine as propagation criterion. The natural neighbour radial point interpolation method was also used to model the problems. Additionally, experimental data was obtained and compared with the numerical results.

The experimental tests were performed in two different types of specimens, compact tension and three point bend. For both cases the initial geometry, which is standardized, suffered changes in order to induce the mixed mode loading.

Equivalent stress intensity factor was analysed considering the most common approaches: Richard/Henn, strain energy release rate, Tanaka and Chen. A comparison between them was performed taking into account the ratio of mode I and mode II stress intensity factors.

Also $da/dN = f(\Delta K_e)$ curves were determined for all equivalent stress intensity factors formulations. Results were compared among themselves and with the mode I original Paris law for the used material.

Reasonable agreement between numerical and experimental results was achieved for most of the cases studied. It should be noticed that heterogeneities are always part of the materials and were not considered in the numerical models, which may be one of the reasons for the differences found. It was also concluded that the geometrical changes in the specimens did not induced a significant mode II loading.

Keywords: Fracture mechanics, Extended finite element method, Mixed mode, Stress intensity factor

Resumo

O conhecimento do comportamento mecânico de estruturas sujeitas a carregamentos ciclos é um assunto bastante importante com vista a determinar as soluções de dimensionamento e projeto mais eficientes. Deste modo e importante conhecer e compreender as propriedades mecânicas associadas a este tipo de problemas. Entre elas conta-se o comportamento de possiveis fendas em condições de modo misto.

O presente trabalho consiste num estudo sobre a propagação de fendas em condições de fadiga considerando situações de carregamento em modo misto. Para esse objectivo foram alteradas geometrias correntes, por forma a originar modo II, e recorreu-se a simulações numéricas que foram comparadas com resultados experimentais.

O objetivo deste estudo é avaliar a capacidade do método dos elementos finitos estendido para prever a trajetória de fendas sujeitas a carregamentos em modo misto. Todas as situações abordadas consistem em carregamentos mistos I-II no plano. O método dos elementos finitos estendido foi implementado no software Abaqus usando como critério de propagação a lei de Paris. Também foi utilizado um metodo sem malha para a obtenção de trajéctorias para a propagação de fendas. Obtiveram-se ainda resultados experimentais para as situações simuladas, que serviram de avaliação dos resultados obtidos numericamente.

Foram utilizados provetes compactos (CT) e de flexão em três pontos (3PB) cuja geometria inicial é normalizada. Uma vez que estes provetes são utilizados para a caracterização de materiais em modo I, a sua geometria foi alterada por forma a existir também carregamentos em modo II na extremidade da fenda.

Os fatores de intensidade de tensão equivalentes foram determinados considerando as formulações mais comuns: Richard/Henn, taxa de libertação de energia, Tanaka e Chen. Estas formulações foram comparadas considerando diferentes valores para o rácio entre K_I e K_{II}.

As curvas $da/dN = f(\Delta K_e)$ foram obtidas para todas as formulações dos fatores de intensidade de tensão equivalente, permitindo a sua comparação e a comparação com a curva $da/dN = f(\Delta K_I)$ do material utilizado. Os resultados obtidos mostram uma boa concordância entre os modelos numéricos e os resultados experimentais apesar de ter sido considerado que o material era homogéneo, o que representa uma situação ideal uma vez que os materiais apresentam sempre diversas heterogeneidades. Verificou-se também que as modificações realizadas nos provetes não provocam uma contribuição de modo II significativa.

Palavras-Chave: Mecânica da Fractura, Método dos elementos finitos estendido , modo misto, factor de intensidade de tensão

Acknowledgements

I would like to express my biggest gratitude to my advisor Professor Sérgio Tavares and to my co-advisor Professor Paulo Tavares de Castro for all the motivation, guidance and for the transmitted knowledge during the realization of this thesis.

Also would like to thank to Professor José Dias Rodrigues for giving me the necessary motivation and skills to work on *LateX*.

A very special acknowledgment to Professor Jorge Belinha for the help in the meshless models and for all the availability shown.

I want to thank Engineer Miguel Figueiredo and Mr. Rui Silva for all the help and availability during the experimental work. Also would like to express my gratitude to Mr. José Almeida for the promptitude in the manufacture of all the specimens.

Contents

List of Figures

List of Tables

Chapter 1

Fracture mechanics basic concepts

1.1 Mixed mode fracture mechanics

A cracked structure can be loaded in three different modes, shown in figure 1.1 for a simple configuration. The mode one or the "opening mode" [1], occurs when the applied load is perpendicular to the crack surfaces and in this case the uncracked ligament is subjected to a normal stress. In mode II or in-plane shear, which can also be designated as "sliding mode" [1], the applied load is parallel to the crack surfaces and causes the crack surfaces to move in a direction which is perpendicular to the leading edge of the crack. In mode III also known as out-of plane shear or by "tearing mode" [1], the applied load is parallel to the crack surfaces and to the lead edge of the crack.

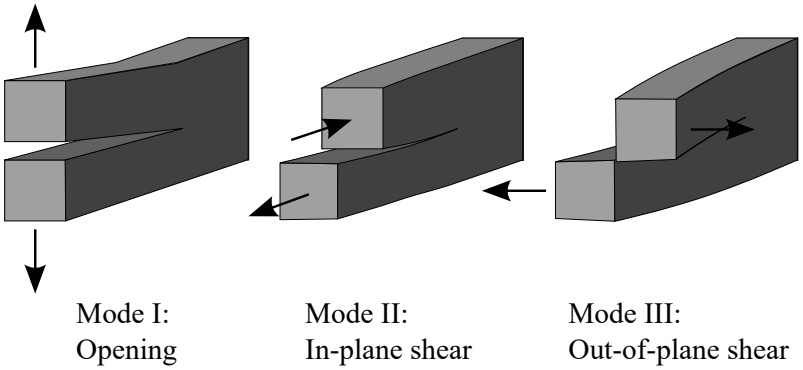

Figure 1.1: The three modes of loading.

Each one of the three loading modes is associated to a strain energy release rate, G_I, G_{II}, G_{III}, or the crack tip stress intensity factor, K_I, K_{II}, K_{III}, where the strain energy release rates are related with the corresponding stress intensity factor. According to Kanninen and Popelar, [2], in a general way the strain energy release rate is given by,

$$G = \frac{1}{E'}\left(K_I^2 + K_{II}^2\right) + \frac{1}{2\mu}K_{III}^2 \tag{1.1}$$

where $E' = E$ for plane stress and $E' = {}^{E}/_{(1-\nu^2)}$ for plane strain and μ is the shear modulus.

$$\mu = \frac{E}{2(1-\nu)} \tag{1.2}$$

If loading corresponds to mode I only, this implies that the values of K_{II} and K_{III} are equal to zero, so it can be concluded that for this situation the relation between the energy

release rate and the stress intensity factor is,

$$G_I = \frac{K_I^2}{E'} \tag{1.3}$$

In case of loading of mode II only, then K_I and K_{III} are equal to zero, therefore the relation between G_{II} and K_{II} can be described by,

$$G_{II} = \frac{K_{II}^2}{E'} \tag{1.4}$$

For pure mode III the relation between the stress intensity factor and the strain energy release rate is the following,

$$G_{III} = \frac{1}{2\mu} K_{III}^2 \tag{1.5}$$

1.1.1 Stress intensity factor under mixed mode loading

A cracked structure can be subjected to various combinations of loading modes, therefore it is desirable to determine an equivalent stress intensity factor, K_e, in order to correlate the behavior of the crack. It is also important to establish a relation between the different values of the stress intensity factors, which can be different for each loading mode. The concept of equivalent stress intensity factor will be further detailed in section 1.3.

1.2 Fatigue propagation

The behavior of a material when subjected to cyclic loading and the prediction of the service life of a component, whether it has a flaw or not, are important engineering problems. In case the component contains a flaw, for example a crack, it is important to predict the propagation velocity of the crack. In order to better understand this kind of problem Paris has proposed, in [3], a propagation law which is still being used nowadays. In this chapter the NASGRO equation, which is a more recent away to predict the velocity of crack propagation will also be described.

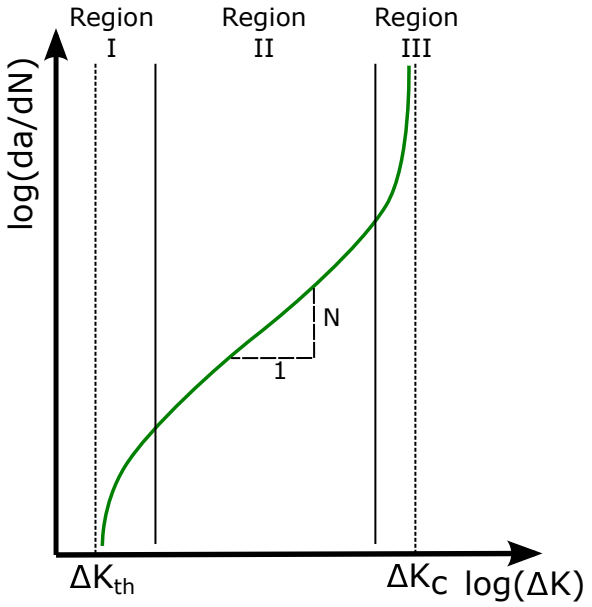

Figure 1.2: Typical fatigue crack propagation fitting curve.

Figure 1.2 shows the typical propagation curve for a metal. This curve can be divided in three different regions. In region I the crack growth rate is very small which implies a large number of cycles in order to induce a significant change on the crack size. The lower limit of ΔK, in this region, corresponds to the value of ΔK_{th} which is the minimum value for ΔK below which there is no propagation. Region II is the stable crack propagation region; in this region the slope of the curve, when represented in logarithmic scale, is approximately linear and it can be fitted by the equation proposed by Paris in [3], as it will be further discussed. Finally region III is the unstable crack propagation region which means that the variation of the crack length in a small number of cycles will be very significant; the higher limit of this region is given by the value of ΔK_c which corresponds to fracture toughness of the corresponding material, (or, for very ductile materials to the plastic collapse of the remaining ligament).

1.2.1 The Paris law

The Paris law is an empirical equation proposed by Paul Paris in 1963 [3], describing crack propagation behavior. It presents a prediction of the crack growth ratio of a fatigue loaded component as:

$$\frac{da}{dN} = C \cdot \Delta K^m \tag{1.6}$$

When plotted in a double-logarithmic plot, the above equation is shown in figure 1.3. It does not fit all of the experimental data but it is a very important relationship because it leads easily to an estimate of the number of cycles which a cracked structure will resist until failure due to fatigue.

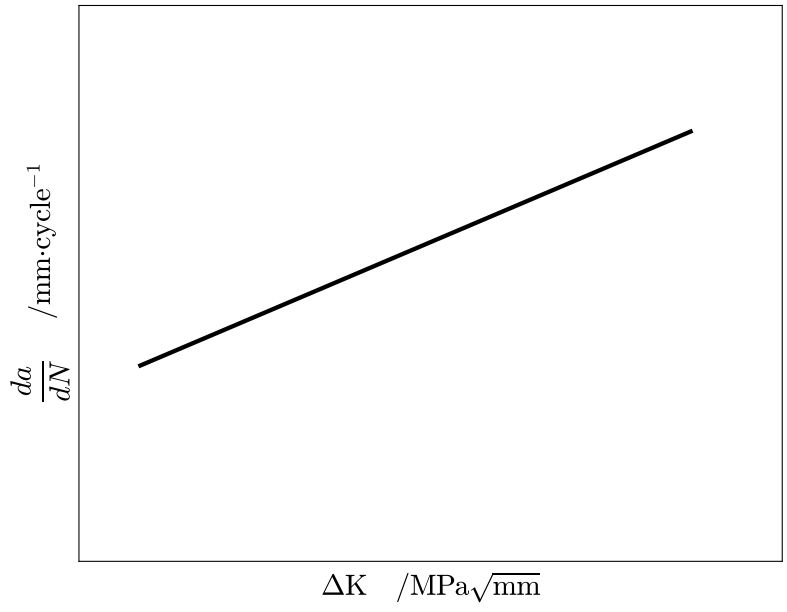

Figure 1.3: Typical representation of the Paris law equation 4.1 in a logarithmic scale.

The estimation made by Paris [3] and described by equation 4.1, is independent of the size of the crack or the amplitude of the load, therefore two different structures with different crack sizes and subjected to different stress levels will exhibit the same crack growth rate if the value of ΔK is the same for both. The equation above only depends of

the value of ΔK and it has to be calibrated for each value of the load ratio ($R = \sigma_{min}/\sigma_{max}$) as it can be observed in figure 1.4. For each value of R the constants C and m take different values too.

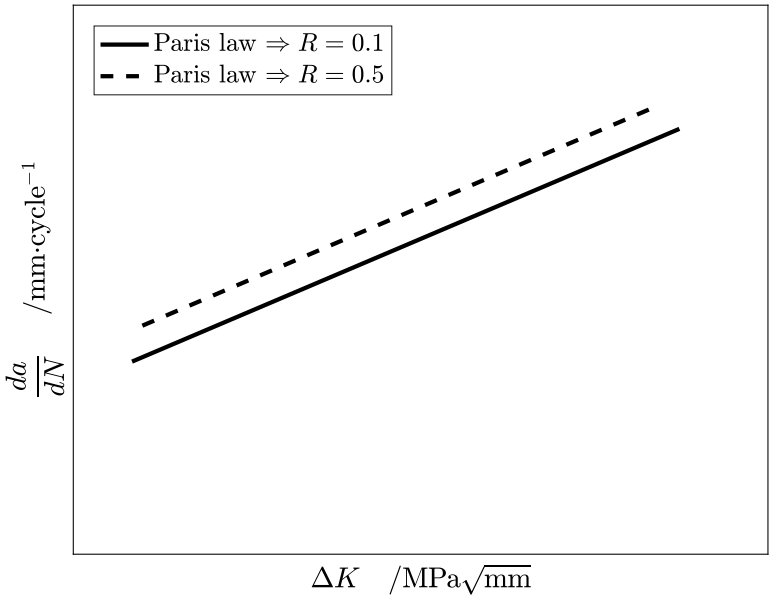

Figure 1.4: Schematic representation of Paris law for different values of R.

1.2.2 NASGRO law

The NASGRO law is a more recent relation to predict the fatigue crack growth of a cracked component when it is subjected to cyclic loading. It was initially developed by NASA. The NASGRO concept is based on a large material database which is available in a software, which according to the NASGRO manual [4], was developed by the National Aeronautics and Space Administration (NASA) and Southwest Research Institute (SwRI).

The NASGRO equation

The equation that describes this law is more complex than the one used by Paris [3] and also takes in consideration the number of cycles needed to propagate a crack when the related situation is characterized by region I and III of the figure 1.2. The inclusion of regions I and III is the biggest difference between the Paris law and the NASGRO law. A typical representation of the curve obtained using the NASGRO law equation can be observed in figure 1.5

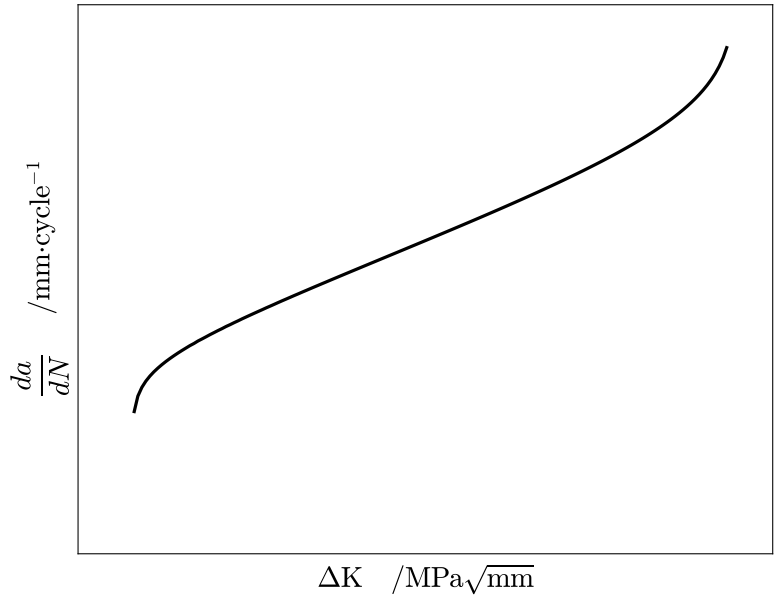

Figure 1.5: NASGRO law equation curve, (schematic representation).

According to the reference manual provided by NASGRO [4], the different elements of the NASGRO equation were developed by several authors form different institutions. The equation takes the following shape:

$$\frac{da}{dN} = C\left[\left(\frac{1-f}{1-R}\right)\Delta K\right]^n \frac{\left(1-\frac{\Delta K_{th}}{\Delta K}\right)^p}{\left(1-\frac{K_{max}}{K_c}\right)^q} \tag{1.7}$$

where N is the number of fatigue cycles, a is the crack length, R is the stress ratio, ΔK is the stress intensity factor range, and C, n, p and q are empirically derived constants, K_{th} is the threshold stress intensity factor, K_c is the fracture toughness of the used material and K_{max} is the maximum applied stress intensity factor. The variable f represents the crack opening function for plasticity-induced crack closure. This last function was originally defined by Newman in [5] as:

$$f = \frac{K_{op}}{K_{max}} = \begin{cases} max(R, A_0 + A_1 R + A_2 R^2 + A_3 R^3) & R \geq 0 \\ A_0 + A_1 R & -2 \leq R < 0 \end{cases} \tag{1.8}$$

and the coefficients are given by,

$$A_0 = (0.825 - 0.34\alpha + 0.05\alpha^2)\left[cos\left(\frac{\pi}{2}\cdot\frac{S_{max}}{\sigma_0}\right)\right]^{1/\alpha} \tag{1.9}$$

$$A_1 = (0.415 - 0.071\alpha)\frac{S_{max}}{\sigma_0} \tag{1.10}$$

$$A_2 = 1 - A_0 - A_1 - A_3 \tag{1.11}$$

$$A_3 = 2A_0 + A_1 - 1 \tag{1.12}$$

In the above equations S_{max}/σ is the ratio of the maximum applied stress to the flow stress and α is a plane stress, plane strain constraint factor.

Figure 1.6 is shows the typical Paris and NASGRO curves for the same material and load ratio (R). As expected, the Paris law is a partial representation of the NASGRO curve.

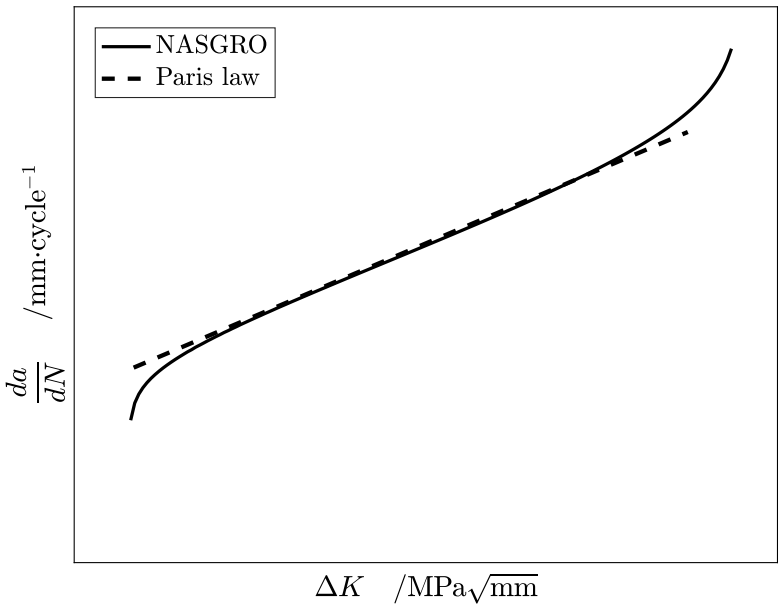

Figure 1.6: Comparison between typical Paris and NASGRO curves, (schematic representation).

1.3 Equivalent stress intensity factor

Different procedures have been proposed to calculate the equivalent stress intensity factor, which is an important variable in order to correlate the crack behavior when a cracked structure is subjected to mixed-mode loading. In this section four different approaches to determine the equivalent stress intensity factor will be presented, as well as a non dimensional comparison between them.

1.3.1 Energy approach

The equivalent stress intensity factor based on the strain energy release as a function of crack size variation $^{dU}/_{da}$:

$$G = -\frac{dU}{da} \tag{1.13}$$

As mentioned e.g. in Fajdiga, [6], the basic equation to determine the equivalent stress intensity factor (K_e) is given by,

$$K_e = \begin{cases} \sqrt{E \cdot G} & \text{plane stress;} \\ \\ \sqrt{\dfrac{E \cdot G}{(1-\nu^2)}} & \text{plane strain.} \end{cases} \tag{1.14}$$

Using the definition of stress intensity factor for every mode given in equations 1.3 to 1.5 and substituting the respective energy release rate in equation 1.14, the general form of the equivalent stress intensity factor based on the energy release rate approach is:

$$K_e = \begin{cases} \sqrt{(K_I^2 + K_{II}^2) + (1+\nu)K_{III}^2} & \text{plane stress;} \\ \\ \sqrt{(K_I^2 + K_{II}^2)(1-\nu^2) + (1+\nu)K_{III}^2} & \text{plane strain.} \end{cases} \tag{1.15}$$

1.3.2 Richard/Henn approach

The approach for equivalent stress intensity factor determination proposed by Richard and Henn in [7], for plane mixed-mode I-II loading, is described as:

$$K_e = \frac{K_I}{2} + \frac{1}{2}\sqrt{K_I^2 + 4(\alpha_1 K_{II})^2} \tag{1.16}$$

where α_1 is the ratio between K_{Ic} and K_{IIc},

$$\alpha_1 = \frac{K_{Ic}}{K_{IIc}}$$

For metals and non-composite materials K_{II_c} data is very limited and hard to determine experimentally, so in order to complete the equation 1.16, Richard proposed in [8] an approximation with a value of α_1 equal to 1.155. For the given value of α_1 the equation 1.16 can be rewritten,

$$K_e = \frac{K_I}{2} + \frac{1}{2}\sqrt{K_I^2 + 5.336 \cdot K_{II}^2} \tag{1.17}$$

The above form of the equation 1.16 is not the only one used to determine the equivalent stress intensity factor. Authors as Borrego *et al.*, in [9], and Henn, in [10], use the following form:

$$K_e = \frac{K_I}{2} + \frac{1}{2}\sqrt{K_I^2 + 6 \cdot K_{II}^2} \tag{1.18}$$

The approach proposed by Richard can be used for cases of spatial mixed mode loading cases, therefore the equation 1.19 proposed by Richard in [8] is a good approximation for those cases.

$$K_e = \frac{K_I}{2} + \frac{1}{2}\sqrt{K_I^2 + 4(\alpha_1 K_{II})^2 + 4(\alpha_2 K_{III})^2} \tag{1.19}$$

where α_2 is the ratio between K_{Ic} and K_{IIIc}. For this case Richard also proposed that a good approximation is achieved for values of α_1 equal to 1.155 and α_2 equal to 1 and, for those values equation 1.19 can be rewritten as follows,

$$K_e = \frac{K_I}{2} + \frac{1}{2}\sqrt{K_I^2 + 5.336K_{II}^2 + 4K_{III}^2} \tag{1.20}$$

In this thesis only plane mixed-mode cases will be treated. As the value of the parameter α_1 is of difficult characterization, a further study will be made in order to better understand the influence of this value in the behavior of the equation 1.16.

1.3.3 Chen and Keer approach

This approach is proposed by Chen and Keer in [11] and it is given by,

$$K_e = \left[\left(K_I^2 + 3 \cdot K_{II}^2\right)^3 \left(K_I^2 + K_{II}^2\right)\right]^{1/8} \tag{1.21}$$

1.3.4 Tanaka approach

This criterion is based in experimental work and in the Paris law equation. Tanaka in [12] proposed the equation 1.22 in order to give an approximation for the equivalent stress intensity factor for plane mixed-mode situation.

$$K_e = \left(K_I^4 + 4K_{II}^4\right)^{1/4} \tag{1.22}$$

1.3.5 Comparison of the different approaches

In this section a non-dimensional comparison between the four approaches presented in the previous sections will be made . The non-dimensional equations for each approach were obtained by dividing all the members of the equation by K_I and the resulting equations are:

- Energy:

$$\frac{K_{e_{Energy}}}{K_I} = \sqrt{1 + \left(\frac{K_{II}}{K_I}\right)^2} \tag{1.23}$$

- Richard:

$$\frac{K_{e_{Richard}}}{K_I} = \frac{1}{2} + \frac{1}{2}\sqrt{1 + 5.336\left(\frac{K_{II}}{K_I}\right)^2} \tag{1.24}$$

- Chen and Keer:

$$\frac{K_{e_{Chen}}}{K_I} = \left[\left(1 + 3\left(\frac{K_{II}}{K_I}\right)^2\right)^3 \cdot \left(1 + \left(\frac{K_{II}}{K_I}\right)^2\right)\right]^{1/8} \tag{1.25}$$

- Tanaka:

$$\frac{K_{e_{Tanaka}}}{K_I} = \sqrt[4]{1 + 8\left(\frac{K_{II}}{K_I}\right)^4} \tag{1.26}$$

Non dimensional stress intensity factor $^{K_e}/_{K_I}$ as function of $^{K_{II}}/_{K_I}$

The evolution of non-dimensional form of the presented approaches for the equivalent stress intensity factor is presented in figure 1.7 as a function of K_{II}/K_I.

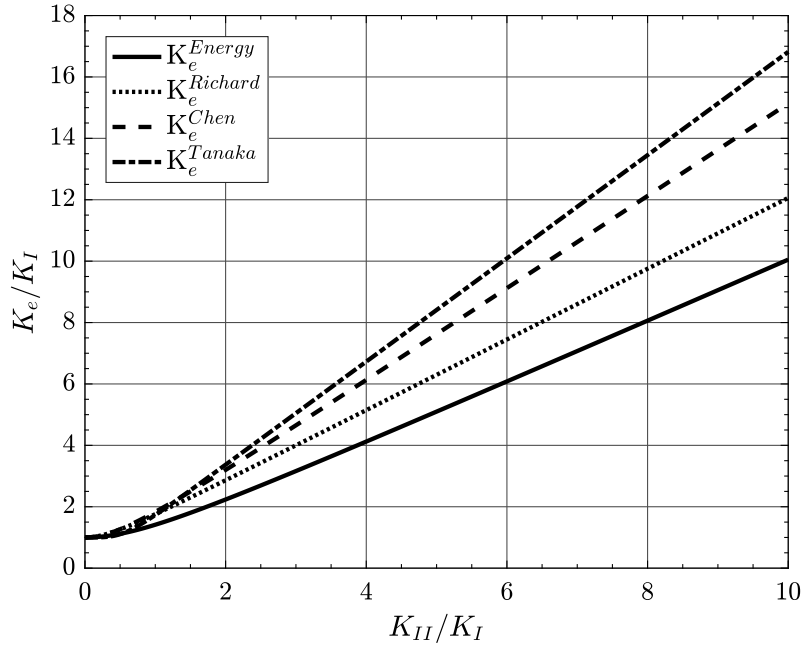

(a) Evolution of $^{K_e}/_{K_I}$ as function of $^{K_{II}}/_{K_I}$.

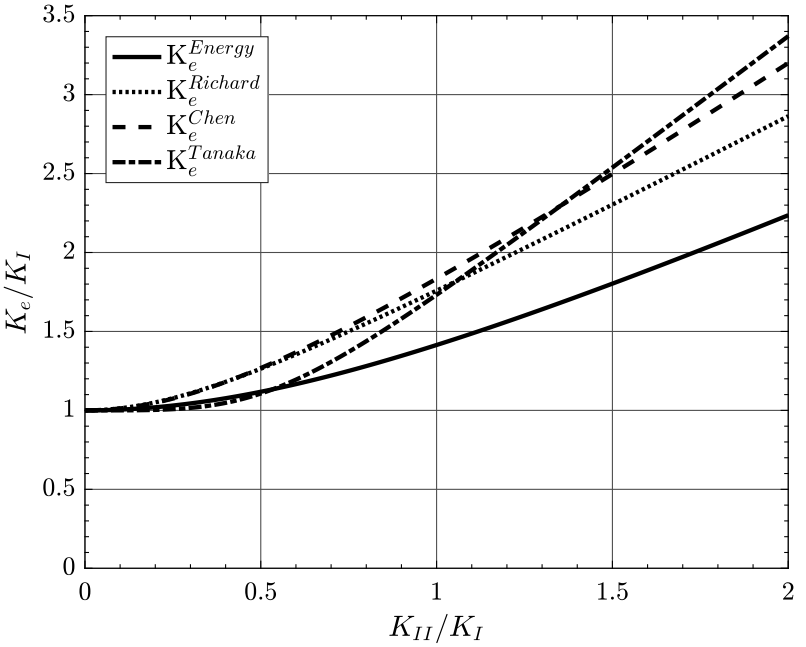

(b) Zoom of the evolution of $^{K_e}/_{K_I}$ as function of $^{K_{II}}/_{K_I}$.

Figure 1.7: Non dimensional $^{K_e}/_{K_I}$ as function of $^{K_{II}}/_{K_I}$.

In figure 1.7a a more general behavior can be observed. Figure 1.7bshows a region of particular interest because it displays the values of the non-dimensional stress intensity

factor for values of K_{II}/K_I smaller than two.

Non dimensional stress intensity factor $^{K_e}/_{K_I}$ as function of $^{K_I}/_{K_{II}}$

The curves for the different approaches to calculate the equivalent stress intensity factor but as function of K_I/K_{II} are now given in figure 1.8. As it was to be expected, when the values of K_I/K_{II} get bigger the value of the non-dimensional stress intensity factor tends to one, meaning that the values of K_{II} when compared with the values of K_I are of minor importance. For this situation mode I is predominant which implies values of K_e very similar to the values of K_I.

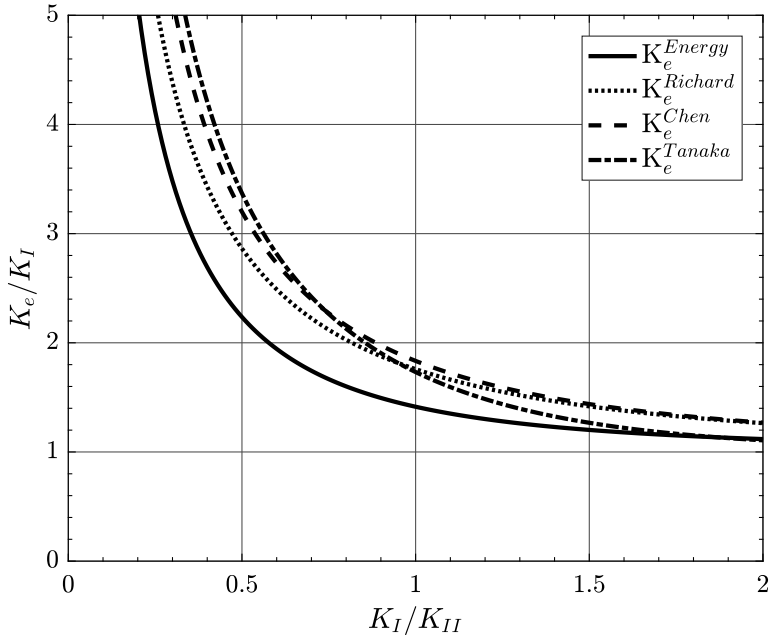

Figure 1.8: Non dimensional stress intensity factor $^{K_e}/_{K_I}$ as function of $^{K_I}/_{K_{II}}$.

Difference between approaches for $^{K_e}/_{K_I}$ as function of $^{K_{II}}/_{K_I}$

A good way to compare the different approaches to characterize and determine the equivalent stress intensity factor is to use one of them as reference, and evaluate what is the percentage difference between them as it is shown in equation bellow.

$$\frac{\frac{K_e^{Approach(x)}}{K_I} - \frac{K_e^{Ref.}}{KI}}{\frac{K_e^{Ref.}}{K_I}} = \frac{K_e^{Approach(x)} - K_e^{Ref.}}{K_e^{Ref.}} \tag{1.27}$$

In this specific case the Energy approach was used as reference, and the percentage differences obtained were plotted as a function of K_{II}/K_I, see figure 1.9.

Observing the plot presented in figure 1.9 it can be concluded that the approach that shows a smaller difference when compared with the Energy approach is the Richard approach even though the maximum percentage difference between them is almost 30%. The Tanaka and Chen approaches present differences much bigger than the Richard approach.

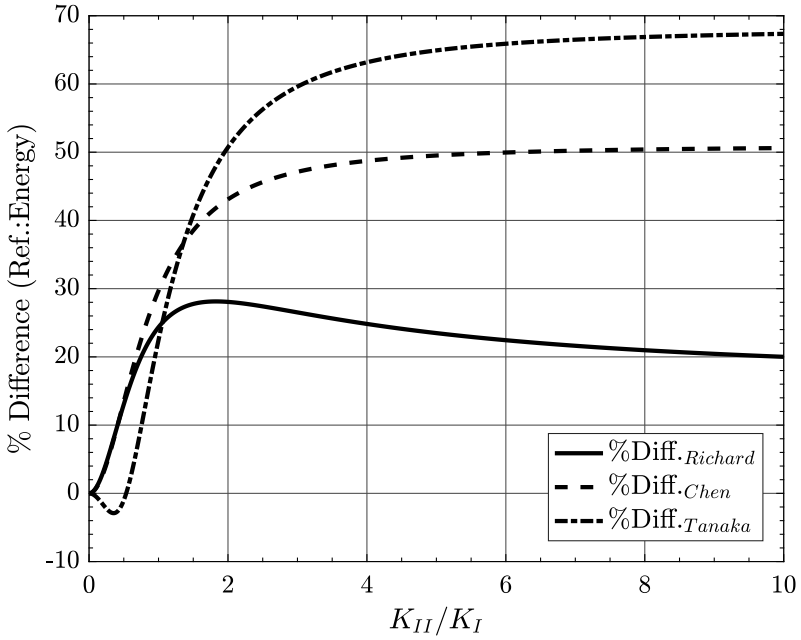

Figure 1.9: Percentage difference as function of $^{K_{II}}/_{K_I}$ using as reference the Energy approach.

Difference between approaches for $^{K_e}/_{K_I}$ as function of $^{K_I}/_{K_{II}}$

The percentage difference between approaches, using as reference the Energy one, was presented in figure 1.9 as a function of K_{II}/K_I. In this section will be determined the percentage difference also using the Energy approach as reference but as a function of K_I/K_{II} . The obtained results can be observed in figure 1.10. In this case the percentage difference is higher for small values of K_I/K_{II} and tends to get smaller for bigger values of K_I/K_{II}. For high values of K_I/K_{II}, bigger than 10, the percentage difference tends to zero. This is an expected result, since the values of all studied approaches for this range of values of K_I/K_{II} are near to the value of K_I as it was shown in figure 1.8

1.3.6 Influence of the α_1 in Richard approach

The Richard approach to determine the equivalent stress intensity factor in plane and spatial mixed-mode situations was presented in section 1.3.2. In this thesis only plane mixed-mode will be studied, so it is important to understand the influence of the empirical constant α_1 used by Richard in equation 1.17. In figure 1.11 several forms of the Richard approach are presented.

It can be concluded that the bigger the value of α_1 is, more conservative the Richard approach gets, because for the same value of K_I/K_{II} the value of K_e/K_I, i.e. K_e is higher.

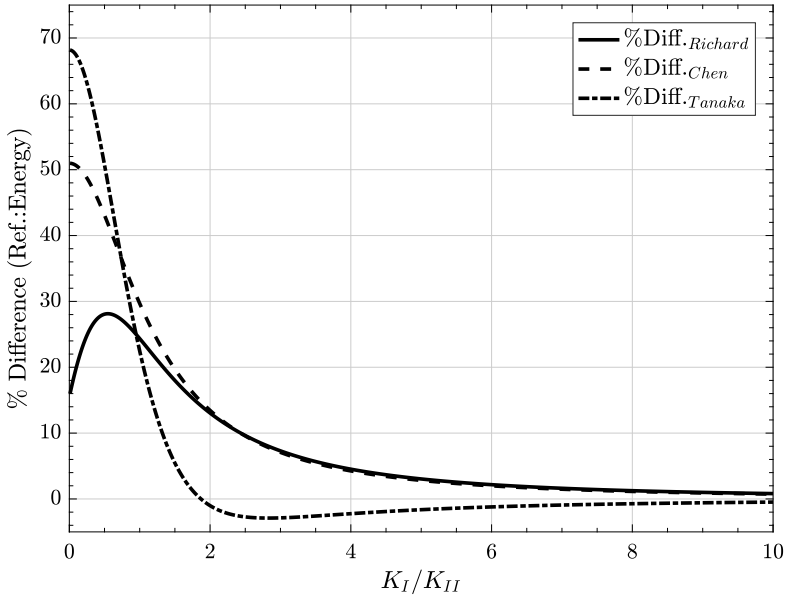

Figure 1.10: Percentage difference as function of $^{K_I}/_{K_{II}}$ using as reference the Energy approach.

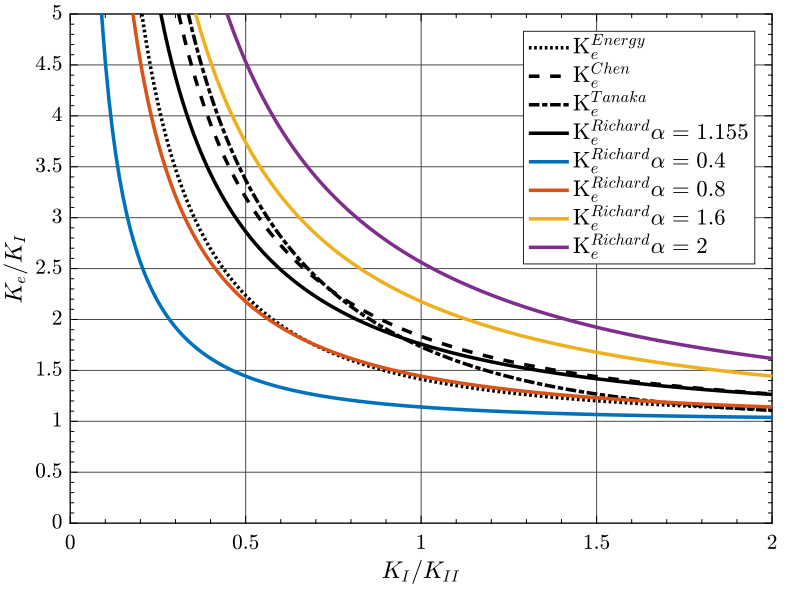

Figure 1.11: K_e/K_I as function of K_I/K_{II}.

1.4 The J integral

The J integral is a concept that allows to calculate an energy release rate even in cases where the plasticity can not be neglected. This integral is path independent which allows to obtain the same result for different contour integral paths. The initial form of the integral is given by Eshelby in [13], and it is based on the theorem of energy conservation, Broek in [1] defines it as:

$$J = \int_{\tau} \left(W dy - T \frac{\delta u}{\delta x} ds \right) \tag{1.28}$$

where W is the strain energy per volume unit, T is the traction tension vector, τ is the contour of the integral, u is the displacement and ds is an element of the contour τ. Figure shows the contour around a crack, as the integral solution is path independent that means that the value of integral resulting from the path τ is the same as the result of the integral for the path τ_t. Since the basis of the equation 1.28 is an energy conservation theorem,

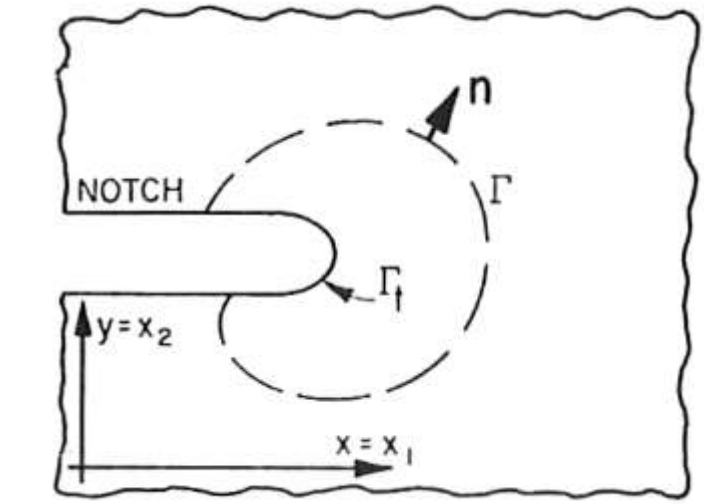

Figure 1.12: Contour around a crack, fig.1 of [14].

the J-integral is an energy related quantity. Rice in [14], has shown that the result of the J integral is equal to the change of the potential energy around the crack tip resulting of a virtual crack extension da; the resulting equation is mentioned eg. by Broek in [1], and has the following form:

$$J = -\frac{\delta V}{\delta a} \tag{1.29}$$

where V is the potential energy. In linear elastic cases the result of the integral is equal to energy release rate,

$$J = \frac{-\delta V}{\delta a} = G \tag{1.30}$$

1.5 Virtual Crack Closure Technique

The virtual crack closure technique (VCCT) is based on the crack closure concept introduced by Irwin when he proved the equivalency between G and K [15], mentioned by Broek in [1]. This method is based on the premise that the energy released when a crack

is extended by Δa from a to $a + \Delta a$ is similar to the quantity necessary to close the crack from $a + \Delta a$ to a. Figure 1.13 shows the crack extended from the initial node l to the node i.

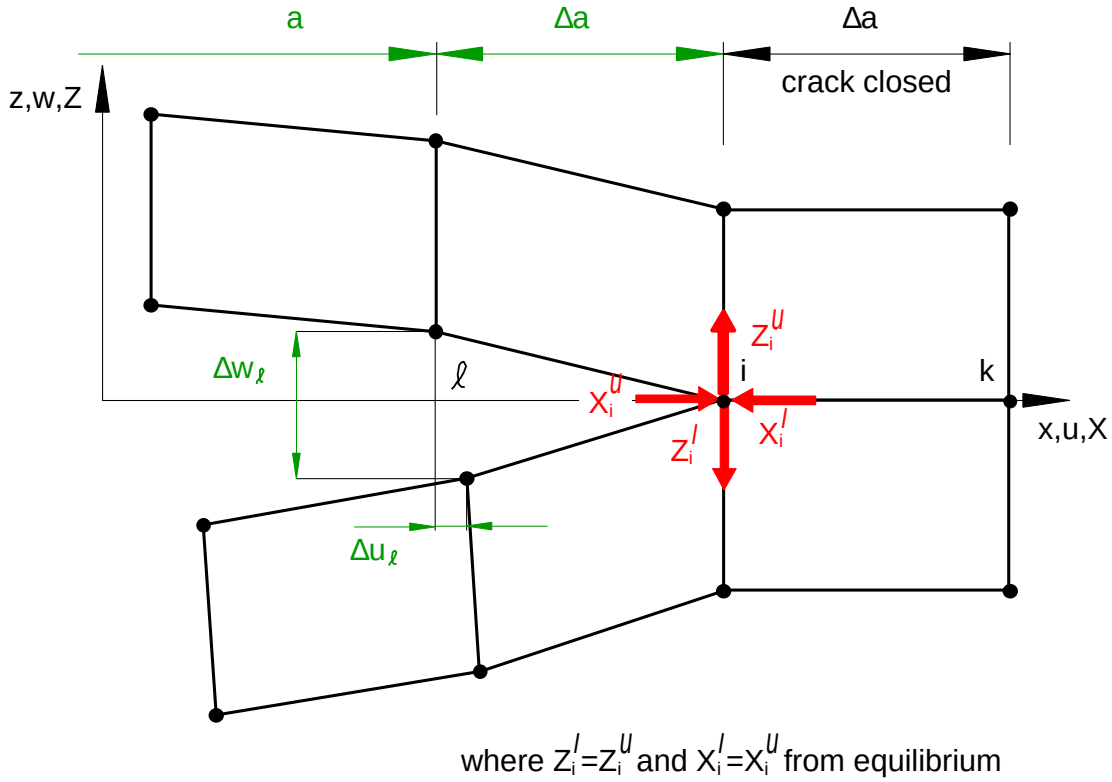

Figure 1.13: Crack closure method 2D model, fig.4 from [16].

For the situation represented in figure 1.13 the quantity of required work to virtually close the crack from i to l is presented by Krueger, [17], and:

$$\Delta E = \frac{1}{2}\left[X_i \cdot \Delta u_l + Z_i \cdot \Delta w_l\right] \tag{1.31}$$

where X_i and Z_i are the shear and opening forces at the nodal point i and Δu_l and Δw_l are the shear and opening displacements at node l. The relation between the work required to close the crack ΔE and the energy release rate G is:

$$G = \frac{\Delta E}{\Delta A} \tag{1.32}$$

where ΔA is the crack surface area. Figure 1.14 shows the model as well as the respective equilibrium forces and displacements needed to calculate the energy release rates G_I and G_{II}. From the relation established in equation 1.32 Krueger,[17], defines the energy release rates for modes I and II as:

$$G_I = -\frac{1}{2\Delta a} Z_i (w_l - w_{l*}) \tag{1.33}$$

$$G_{II} = -\frac{1}{2\Delta a} X_i (u_l - u_{l*}) \tag{1.34}$$

where Δa is the length of the element ate the crack front, X_i and Z_i are the equilibrium forces at the node i, u_l and w_l are the upper displacements at node l, w_l and u_l are the lower displacements at the node l too.

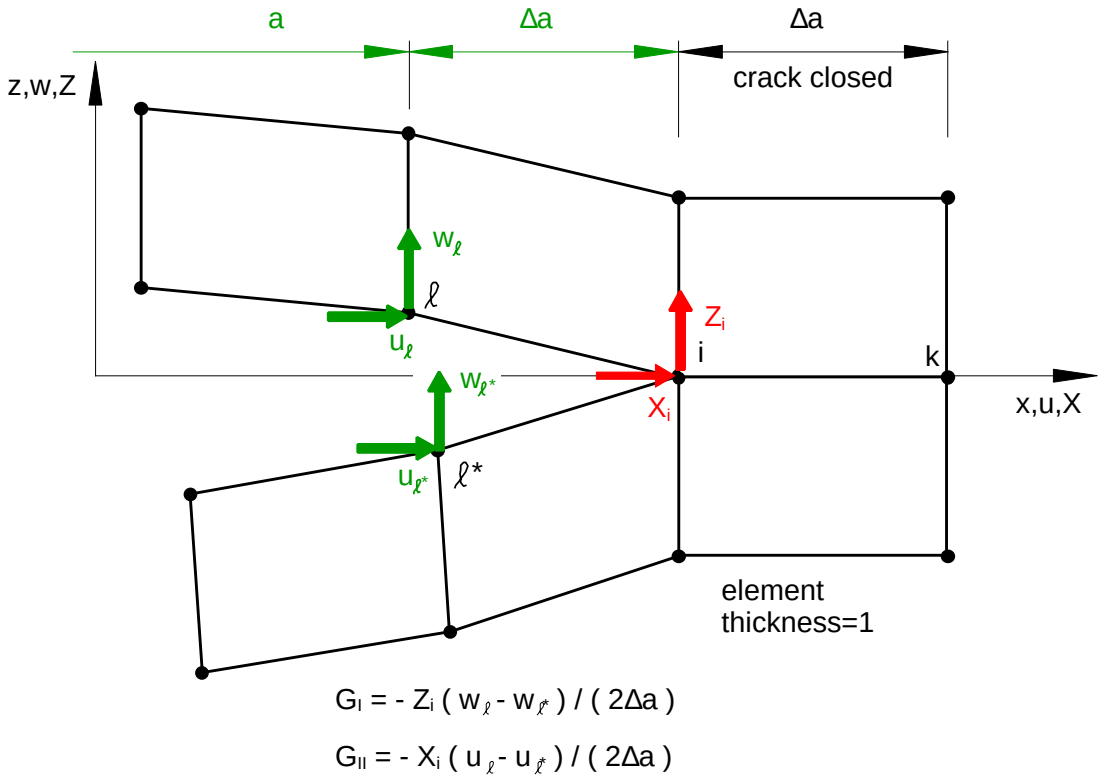

Figure 1.14: Model of the VCCT method for a four node element, fig.7(a) from [16].

The crack surface is considered to be Δa because it is assumed that the two-dimensional model has a unitary thickness so,

$$\Delta A = \Delta a * 1$$

and consequently,

$$\Delta A = \Delta a$$

For the eight nodes element the calculation procedure is very similar to the one used for a four nodes element. Figure 1.15 shows the model used as well as all the equilibrium forces and displacements. In this case Krueger, [17], defines the energy release rates for modes I and II through the following equations:

$$G_I = -\frac{1}{2\Delta a}\left[Z_i(w_l - w_{l*}) + Z_j(w_m - w_{m*})\right] \quad (1.35)$$

$$= \quad (1.36)$$

$$G_{II} = -\frac{1}{2\Delta a}\left[X_i(u_l - u_{l*}) + X_j(u_m - u_{m*})\right] \quad (1.37)$$

where w_l, u_l, w_m and u_m are the upper displacements in nodes l and m, w_{l*}, u_{l*}, w_{m*} and u_{m*} are the lower displacements at nodes l and m either. Also in this case the thickness of the model is considered to be unitary.

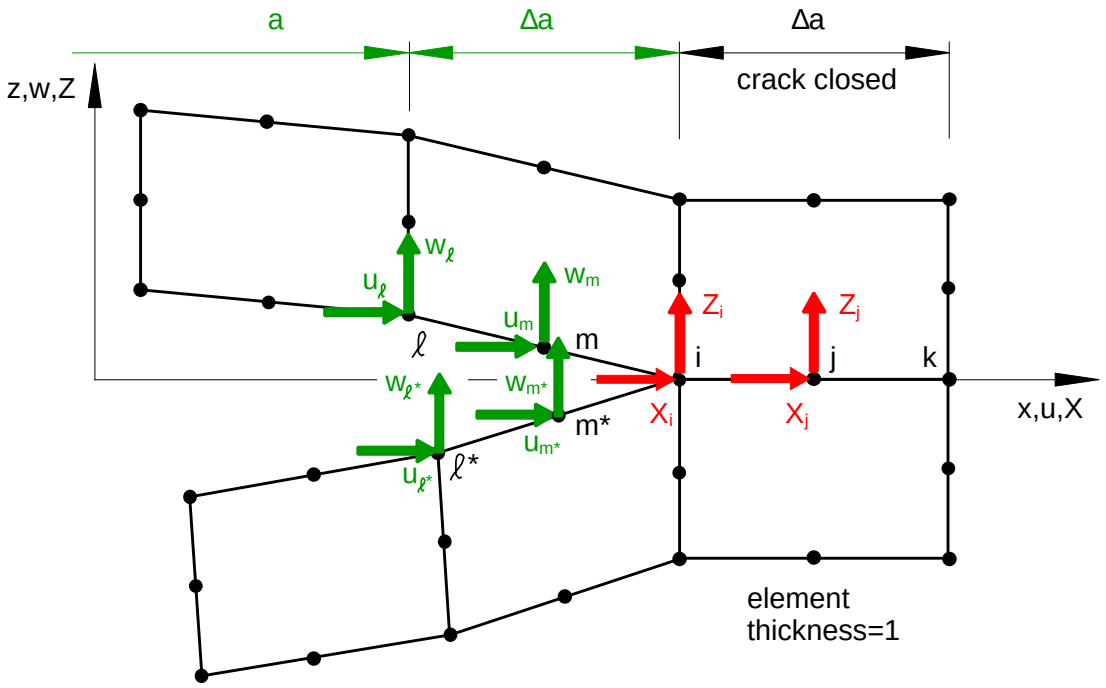

$$G_I = -[\, Z_i \,(\, w_\ell - w_{\ell^*} \,) + Z'_j \,(\, w_m - w_{m^*} \,) \,] \,/\, (\, 2\Delta a \,)$$

$$G_{II} = -[\, X_i \,(\, u_\ell - u_{\ell^*} \,) + X'_j \,(\, u_m - u_{m^*} \,) \,] \,/\, (\, 2\Delta a \,)$$

Figure 1.15: Model of the VCCT method for a eight node element, fig.7(b) from [16].

Chapter 2

Extended finite element method

In the past recent years, the need to accurately model discontinuities in finite element models lead investigators to develop techniques which try to model those discontinuities using structured meshes, in which the structured mesh has to be adapted to the discontinuity geometry. These techniques imply that the model has to be remeshed at every increment of the discontinuity. Alternatively, techniques that use functions to enrich the region which contains a discontinuous field, do not require to remesh all model or do not use the remeshing technique at all.

The modelling of cracks and crack growth using the finite element method with minimal remeshing was first introduced by Belytschko & Black, [18]. The approach was based on the partition unity property for finite elements which was presented by Melenk & Babuška, [19]. This property consists of the capability of the shape functions to reproduce a constant, which is crucial for convergence. It also uses enrichment functions on the nodes of the elements which contain the crack and crack tip. The approach made by Belytschko & Black, [18] was improved by Moës, Dolbow & Belytschko, [20] who developed a fully mesh independent technique to modeling cracks and named as the extended finite element method (xFEM). The extended finite element method, and its capability to model discontinuities without remeshing, suggests an application to fracture mechanics which uses strong discontinuities in order to simulate (macroscopic) cracks. Therefore the xFEM allows to study the evolution of a crack as well as the crack path propagation without remeshing at every crack increment, which is an advantage of xFEM when compared with the standard finite element method (FEM).

2.1 Basic theory of the extended finite element method

In this section a basic description of the theory behind the extended finite element method will be presented. A description of strong and weak discontinuities will be presented first; then the strong and weak forms for domains containing strong discontinuities will be presented, and finally the enrichment process as well as the used functions will be described.

2.1.1 Weak and strong discontinuities

The xFEM essential idea is the integration of a discontinuous displacement field into the standard finite element method model employing a local enrichment of the basic finite element method solution. This allows the modeling of discontinuities, such as cracks or dislocations, without requiring an explicit concretization of the discontinuity. Based on

the type of displacement discontinuity which can be a strong discontinuity in case of a crack or can be a weak discontinuity in case of a shear band or material interface. The schematic displacement field in one dimension is presented by Häusler [21] and it can be observed in figure 2.1.

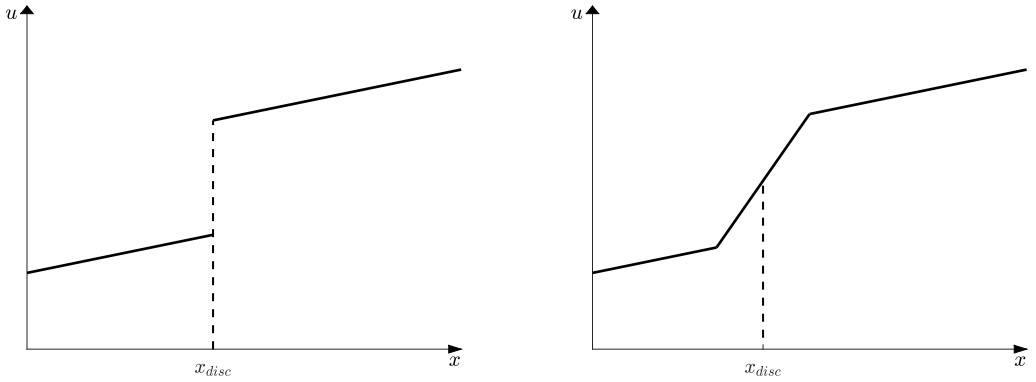

(a) Strong discontinuity.

(b) Weak discontinuity.

Figure 2.1: Schematic representation of the displacement field of a strong and weak discontinuity.

2.1.2 Problem formulation

In this subsection the problem formulation for a strong discontinuity will be described, presenting the strong form as well as its weak form when the xFEM is used.

Strong form

Considering the arbitrary domain Ω shown in figure 2.2 the equilibrium equations and boundary conditions and consequently the strong formulation of the problem are defined according to Moës, Dolbow & Belytschko in [20] as follows,

$$\nabla \cdot \boldsymbol{\sigma} = 0 \text{ in } \Omega \tag{2.1}$$

$$\boldsymbol{\sigma} \cdot \boldsymbol{n} = \bar{\boldsymbol{t}} \text{ on } \Gamma_t \tag{2.2}$$

$$\boldsymbol{\sigma} \cdot \boldsymbol{n} = 0 \text{ on } \Gamma_{c^+} \tag{2.3}$$

$$\boldsymbol{\sigma} \cdot \boldsymbol{n} = 0 \text{ on } \Gamma_{c^-} \tag{2.4}$$

where $\boldsymbol{n}$ is the unit outward normal, $\boldsymbol{\sigma}$ is the Cauchy stress tensor and $\boldsymbol{b}$ is the body force per unit of volume. Considering small displacements, the kinematics equations consists of the strain-displacement relation,

$$\boldsymbol{\varepsilon} = \boldsymbol{\varepsilon}(\boldsymbol{u}) = \nabla_{\boldsymbol{s}} \boldsymbol{u} \tag{2.5}$$

where $\nabla_{\boldsymbol{s}}$ is the symmetric part of the gradient operator. The boundary conditions of the problem are given by:

$$\boldsymbol{u} = \bar{\boldsymbol{u}} \text{ on } \Gamma_u \tag{2.6}$$

The fundamental relation is stated by Hooke's law:

$$\boldsymbol{\sigma} = \boldsymbol{C} : \boldsymbol{\varepsilon} \tag{2.7}$$

where $\boldsymbol{C}$ is the Hooke tensor.

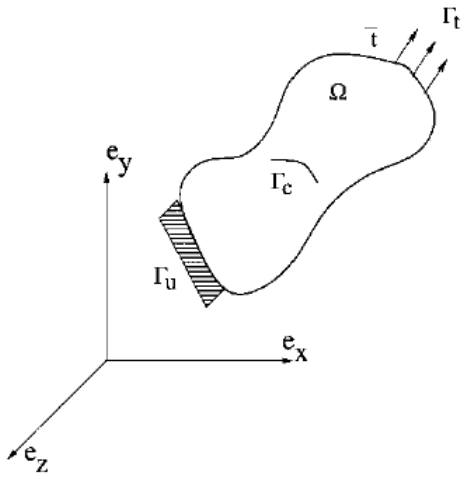

Figure 2.2: Body with internal discontinuity.

Weak form

In the previous subsection the strong form of a strong discontinuity was presented. In this section will be described the weak form of the strong discontinuity problem. The weak form for this case has been deduced based on the strong form of the problem by Moës, Dolbow and Belytschko [20]. The equation which describes the weak form of the problem is,

$$\int_{\Omega} \boldsymbol{\varepsilon}(\boldsymbol{u}) : \boldsymbol{C} : \boldsymbol{\varepsilon}(\boldsymbol{v}) \mathrm{d}\Omega = \int_{\Omega} \boldsymbol{b} \cdot \boldsymbol{v} \mathrm{d}\Omega + \int_{\Gamma_t} \bar{\boldsymbol{t}} \cdot \boldsymbol{v} \mathrm{d}\Gamma \qquad \forall \boldsymbol{v} \in u_0 \tag{2.8}$$

where u_0 is the test function space and $\bar{\boldsymbol{t}}$ is the traction forces vector. It is proved by Belytschko an Black [18] that the equation 2.8 is equivalent to the strong form, equation 2.1, for approximations which use a nodal enrichment and that also satisfy the traction-free boundary condition on the crack faces when the domain contain a crack.

2.1.3 Modelling a crack with local enrichment

Considering the weak form solution (2.8) and bearing in mind that the obtained solution is valid to represent domains containing traction-free cracks, the applicability of enrichment function which lead to a discontinuous displacement field along the crack and crack tips will now be analysed.

The solution for the displacement field using the standard finite element method u^h is given by,

$$\boldsymbol{u}^h = \sum_{i=1}^{10} \boldsymbol{u}_i \phi_i \tag{2.9}$$

where $\boldsymbol{u}_i$ is the nodal displacement vector at the node i and ϕ_i is the shape function associated with the same node.

Based on standard finite element method in which the crack is modeled by the structural mesh elements Moës, Dolbow and Belytschko [20] presented a solution of modeling a discontinuous displacement field, in the specific case a crack, using a Heaviside function ("jump function") $H(x)$, shown in equation 2.11. When the enrichment is only made using the jump function, the crack tip as to be coincident with an element edge otherwise the

finite element method will not be capable of represent the displacement field ate the crack tip, for this case the general solution for the displacement field is given by,

$$\boldsymbol{u}^h(x) = \sum_{i=1}^{n} \boldsymbol{u}_i \phi_i(x) + \sum_{j=1}^{k} \phi_j(x) \boldsymbol{c}_j H(x) \tag{2.10}$$

where the first term on the right side of the above equation is the displacement field of the elements which are not intersected by the crack, and the second term is the displacement field of the elements which are intersected by the crack. The variable n represent the total number of elements which are not intersected and will no be enriched, k is the total number of nodes to be enriched and $\boldsymbol{c_j}$ represent the additional degrees of freedom included in the enriched sets of nodes.

$$H(x) = \begin{cases} 1 & \text{for } y > 0 \\ -1 & \text{for } y < 0 \end{cases} \tag{2.11}$$

Figure 2.3a shows the case described above, in which the enriched nodes are the circled ones, in other words are the nodes which belong to the elements intersected by the crack. The value of $H(x)$ function is equal to one if the element is above the crack or takes de value of minus one if the element is situated below the crack.

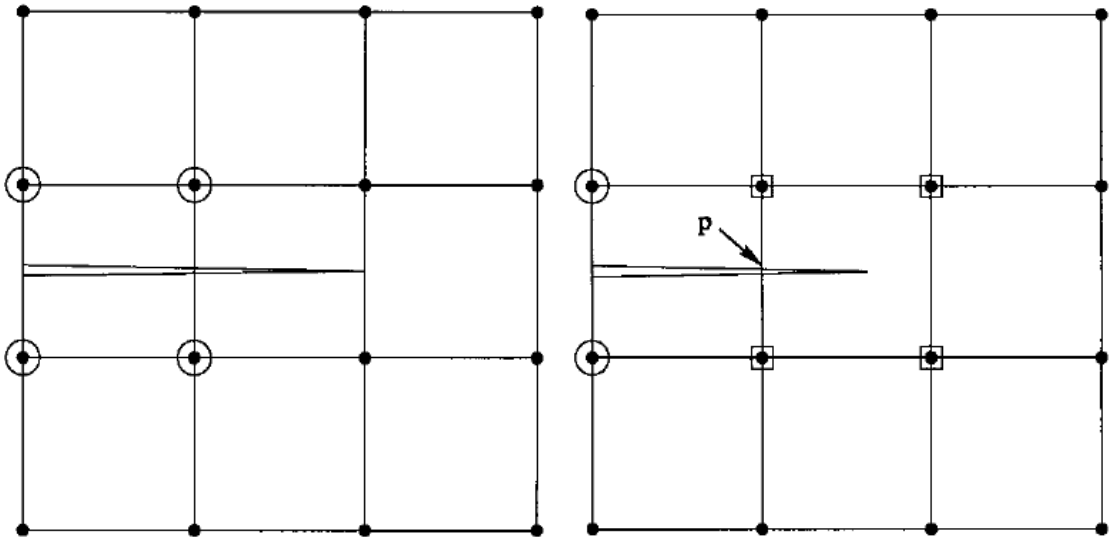

(a) Schematic model of a crack modeling with jump functions enrichment.

(b) Schematic model of a crack modeling with jump functions and asymptotic functions enrichment.

Figure 2.3

The process of local enrichment using the Heaviside function does not allow to simulate cracks which are not coincident with an element edge as shown in figure 2.3b. In order to simulate that type of cracks the enrichment process has to be modified and the asymptotic crack tip functions have to be added to the equation 2.10.

The asymptotic crack tip functions according to Häusler in [21] were originally established for representation of the asymptotic crack tip field in element free Galerkin method. Those functions are defined in the local polar coordinates r and θ and have the following form and are represented in figure 2.4,

$$\Phi_\beta(x_i) = \Phi_\beta(r,\theta) = \left\{ \sqrt{r} \cdot \sin\frac{\theta}{2}, \sqrt{r} \cdot \cos\frac{\theta}{2}, \sqrt{r} \cdot \sin\frac{\theta}{2} \cdot \sin\theta, \sqrt{r} \cdot \cos\frac{\theta}{2} \cdot \sin\theta, \right\} \tag{2.12}$$

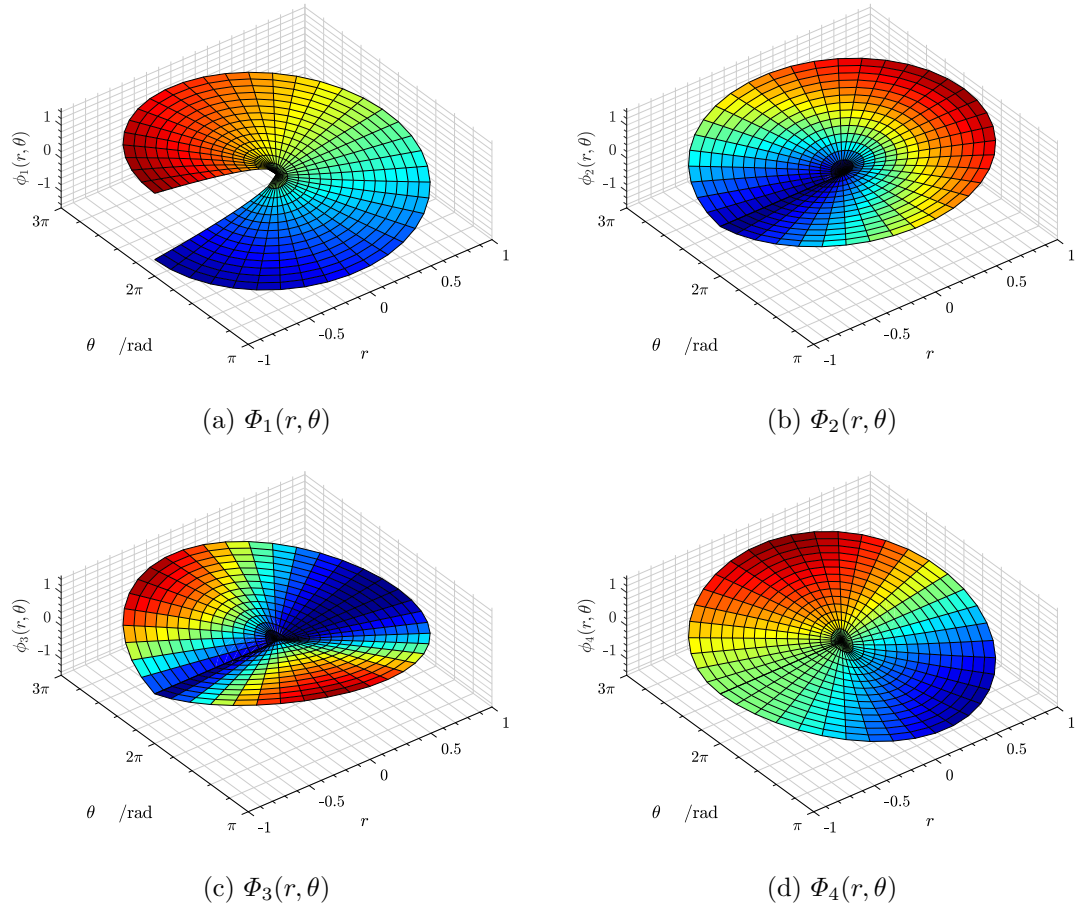

(a) $\Phi_1(r,\theta)$ (b) $\Phi_2(r,\theta)$

(c) $\Phi_3(r,\theta)$ (d) $\Phi_4(r,\theta)$

Figure 2.4: Representation of the asymptotic crack tip functions

According to Moës, Dolbow and Belytschko [20] for edge crack as shown in figure 2.3b the approximation of the displacement field is given by,

$$\boldsymbol{u}^h(x) = \sum_{i=1}^{n} \boldsymbol{u}_i \phi_i(x) + \sum_{j=1}^{k} \phi_j(x) \boldsymbol{c}_j H(x) + \sum_{g=1}^{f} \Phi_g(x) \left(\sum_{\beta=1}^{4} \boldsymbol{d}_\beta^g \Phi_\beta(x) \right) \tag{2.13}$$

where f is the total number of nodes to be enriched with asymptotic crack tip funtions, in figure 2.3b are the squared nodes, and the variable $\boldsymbol{d}_\beta^g$ are the additional degrees of freedom that belong to the nodes which are enriched with asymptotic crack tip functions.

For a general case in which the crack has two tips, according to [20] the approximation takes the following form,

$$\begin{aligned} \boldsymbol{u}^h(x) = & \sum_{i=1}^{n} \phi_i(x) \boldsymbol{u}_i + \sum_{j=1}^{k} \phi_j(x) \boldsymbol{c}_j(x) H(x) \\ & + \sum_{g_1=1}^{f_1} \Phi_{g_1}(x) \left(\sum_{\beta=1}^{4} \boldsymbol{d}_\beta^{g_1} \Phi_\beta^1(x) \right) + \sum_{g_2=1}^{f_2} \Phi_{g_2}(x) \left(\sum_{\beta=1}^{4} \boldsymbol{d}_\beta^{g_2} \Phi_\beta^2(x) \right) \end{aligned} \tag{2.14}$$

where the third and the fourth members of the right side of the above equation correspond to the nodal enrichment of the crack tips with the asymptotic functions. One example of a domain containing crack which the solution can be approximated using the equation 2.14

can be observed in figure 2.5 where an arbitrary crack is placed on a mesh domain and the enriched nodes are identified, the circular ones are the nodes enriched with the Heaviside function and the squared ones are enriched with the crack tip asymptotic functions.

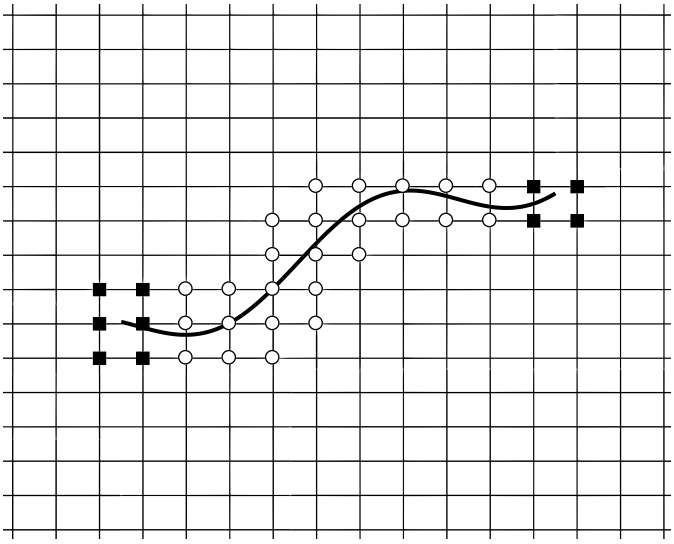

Figure 2.5: Arbitrary crack placed on a mesh.

Numerical integration of the weak form

The standard finite element method uses in general the standard Gauss quadrature in order to integrate the displacement field defined by the weak form of a continuous problem. When the domain of integration becomes discontinuous the standard Gauss quadrature may not adequately integrate the displacement field. Therefore Moës, Dolbow and Belytschko in [20] made a modification in the standard Gauss quadrature which consists of dividing the elements intersected by the crack in triangles, as can be observed in figure 2.6, in order to introduce additional degrees of freedom to better integrate the discontinuous field above and below the crack edges. Those additional degrees of freedom are only for integration purposes, they are not associated to a modification on the structural mesh.

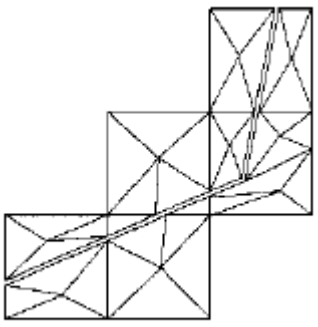

Figure 2.6: Division of the elements cut by a crack in triangles in order to integrate the discontinuous field, figure 10(c) from [20].

Chapter 3

Meshless methods

In this chapter a brief introduction to the meshless methods will be done, more particularly for the natural neighbour radial point interpolation method (NNRPIM).

3.1 Natural Neighbour Radial Point Interpolation Method

The natural neighbour radial point interpolation method (NNRPIM) is a meshless method which is based on a local weak form. In this meshless method the nodal connectivity is defined by the sub-domains which support the weak form of the problem. The Voronoï diagram is used in order to define the natural neighbours of a node. More details about the nodal connectivity and the use of the Voronï diagram for determination of the natural neighbours are given by Azevedo in [22].

Figure 3.1 shows how the nodal connectivity is determined making use of the Voronoï diagram.

The first degree influence-cell define natural neighbours which are neighbours of the chosen node. The second degree influence-cell is composed by nodes which are neighbours nodes of the nodes which define the first degree influence-cell.

When a problem is analysed using the NNRPIM method, the first or second degree of influence-cell can be chosen. Higher the degree of the influence cell, higher is the number of nodes which are used to define the sub-domain.

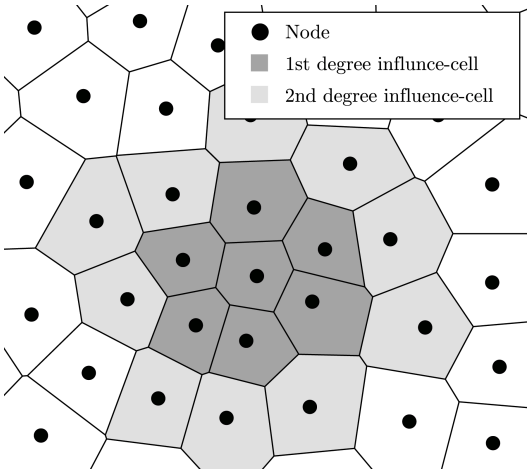

Figure 3.1: Example of application of the Voronoï diagram, figure 2.4 from [22]

This is just a brief description of the NNRPIM metehod, Azevedo, [22], describes all the procedures of the method, from the nodal connectivity to the integration process and the application of the method to the fracture mechanics.

Chapter 4

Material Characterization

In this chapter the mechanical properties of the material used will be described. All the specimens that were tested in the experimental component of this work were of an aluminum alloy: AA6082 T6.

4.1 Fatigue properties for AA6082 T6

4.1.1 Mechanical properties

In this section the non-fracture mechanics related properties will be presented. The mechanical properties which are presented in table 4.1 are given in [23], [24] and [25].

AA6082-T6	
Young modulus [E] /GPa	69
Yield strength [σ_{Yield}] /MPa	>260
Ultimate strength [σ_U] /MPa	310
Poisson ratio	0.33 [26]

Table 4.1: Mechanical properties of the aluminium alloy 6082-T6.

4.1.2 Fatigue propagation laws

In order to prepare the experimental procedure and determine the load which will be used to obtain the experimental results it is needed to characterize the used material. Using the NASGRO software it is possible to obtain da/dN as a function of ΔK for the used aluminum alloy (AA6082 T6) and from that curve the constants needed to characterize the Paris for the given material can be determined.

As it can be observed in figure 1.6, the Paris law is a partial representation of the NASGRO fitting curve, therefore consulting the available data from the NASGRO material database and from the respective fitting curve, for the interval where the relationship is linear (region II of figure 1.2), it is possible to read two values and determine the Paris law constants for the chosen material. The chosen values are presented in table 4.2.

Table 4.2: Two points of the region II obtained from NASGRO fitting curve for AA6082-T6 LT.

ΔK /MPa·$\sqrt{\text{mm}}$	$\frac{da}{dN}$ /mm·cycle^{-1}
584.53	0.0020
281.37	$1.284 \cdot 10^{-4}$

Matching the two pairs of values of the table 4.2 with the equation 1.6 it is possible to determine the values of C and m which allow to characterize the Paris law for the AA6082. The values of C and m are:

$$\begin{aligned} C &= 85.41 \cdot 10^{-15} \\ m &= 3.76 \end{aligned}$$

Therefore the Paris law which is given by equation 1.6 can now be written as follows,

$$\frac{da}{dN} = 85.41 \cdot 10^{-15} \cdot \Delta K^{3.76} \tag{4.1}$$

In figure 4.1 the NASGRO and the Paris law curves for the used aluminum alloy are shown. The load ratio is equal to 0.1, the load ratio used in the experimental procedure.

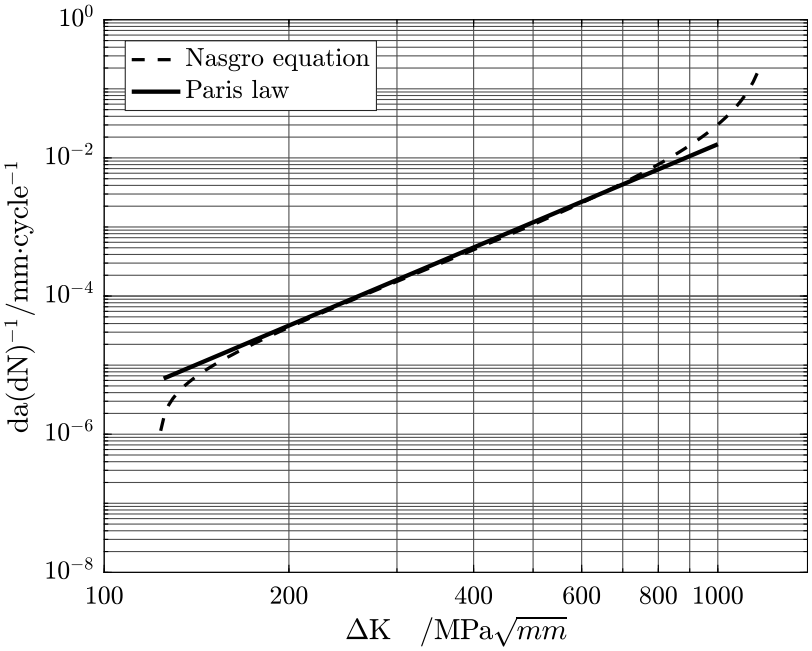

Figure 4.1: NASGRO fitting curve and Paris law approximation curve.

Crack propagation domain limits

The values of the fracture toughness stress intensity factor and of threshold stress intensity factor are not easily found in the literature, nevertheless they can be estimated for the given material consulting the NASGRO database material.

The higher value of the NASGRO database for the range of the stress intensity factor was used to estimate the value of the fracture toughness of the material. The lowest value of the same material database was used to estimate the threshold value. The values are:

$$\Delta K_{max} = 1177.9 \text{ MPa}\sqrt{\text{mm}} \quad \Delta K_{min} = 123.6 \text{ MPa}\sqrt{\text{mm}}$$

The load ratio is 0.1 implies that

$$\begin{cases} \dfrac{K_{min}}{K_{max}} = 0.1 \\ \\ K_{max} - K_{min} = \Delta K = 0.9 \cdot K_{max} \end{cases} \tag{4.2}$$

The values of the fracture toughness and threshold stress intensity factor are the values of K_{max} resulting from solving the system of equations present in 4.2 for the values of ΔK_{max} and ΔK_{min}. The resulting values are the following,

$$K_c \cong 1295.7 \quad \text{MPa}\sqrt{\text{mm}} \tag{4.3}$$
$$K_{th} \cong 136 \quad \text{MPa}\sqrt{\text{mm}} \tag{4.4}$$

or

$$K_c \cong 41 \quad \text{MPa}\sqrt{\text{m}} \tag{4.5}$$
$$K_{th} \cong 4.3 \quad \text{MPa}\sqrt{\text{m}} \tag{4.6}$$

Chapter 5

Abaqus implementation and preliminary studies

Now that the extended finite element method as been presented it is important to describe its implementation in the numerical models of the present work.

In this chapter, some preliminary studies will also be made in order to ensure that the defined parameters lead to reasonable results which will allow to compare the numerical and the experimental results that will be presented.

5.1 Abaqus implementation

Some crucial aspects have to be mentioned and explained in order to fully characterize the extended finite element method implementation in Abaqus. Some of those aspects are the crack propagation criterion, material properties as well as the laws used to determine equivalent stress intensity factors.

5.1.1 Material Properties

In this section the material properties used in numerical models will be defined. As the numerical models and experimental tests only include linear elastic fracture mechanics considerations, there is no need to characterize the plastic behavior of the used material. All the mechanical properties used to define the numerical models were already presented in the previous section, more precisely in table 4.1. The first mechanical properties to be defined are the Young modulus and the Poisson ratio followed by the "Damage for Traction Separation laws". In figure 5.1 are shown printscreens of Abaqus. The damage evolution for traction separation laws fields is shown in figure 5.1a, and the damage evolution sub-option definitions in figure 5.1b.

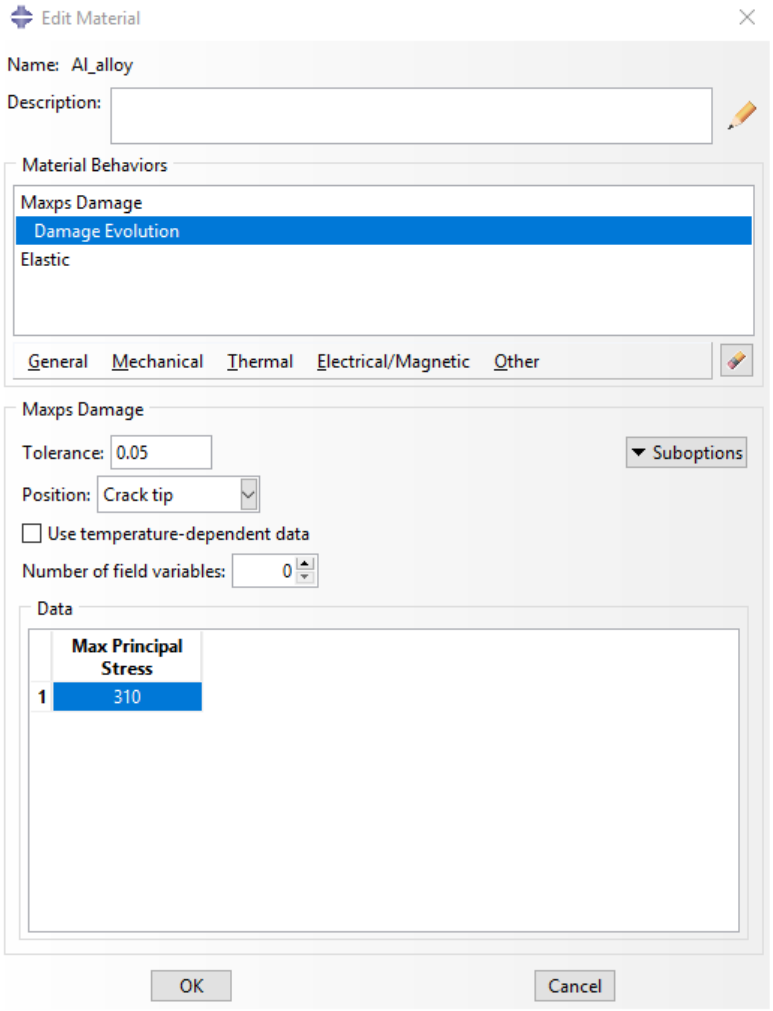

(a) Damage evolution for traction separation laws fields.

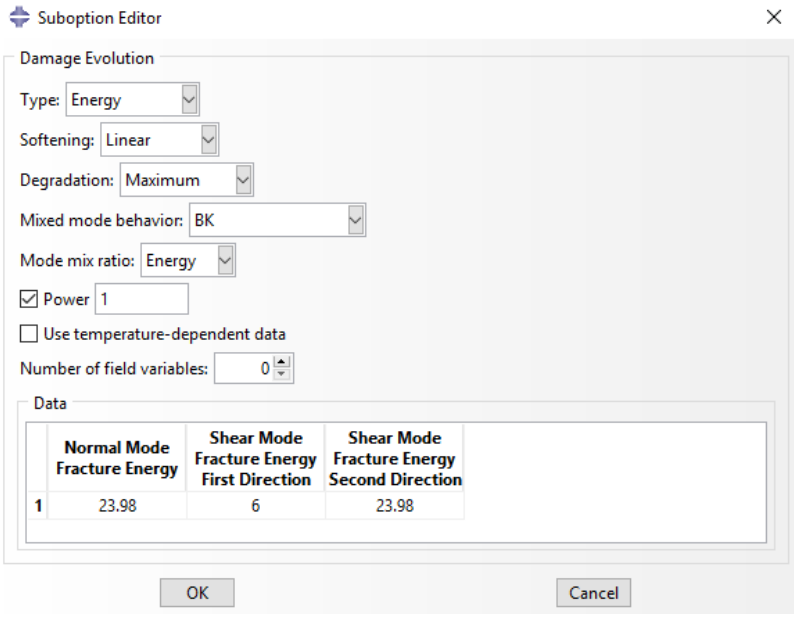

(b) Damage evolution suboptions definitions.

Figure 5.1: Defined mechanical properties for numerical models.

According to Abaqus documentation [27], crack propagation occurs when the following condition is reached,

$$f = \frac{G_{equiv}}{G_{equiv_c}} \geq 1 \tag{5.1}$$

where f is the fracture damage criterion, G_{equiv} is the equivalent strain energy release rate calculated at the node and G_{equiv_c} is the critical equivalent energy release rate which is calculated based on the mixed-mode behavior parameter. The available laws are three and are summarized below.

- BK law
  The BK law according to Abaqus manual [27] is described by the following equation

  $$G_{equiv_c} = G_{I_c} + (G_{II_c} - G_{I_c}) \cdot \left(\frac{G_{II} + G_{III}}{G_I + G_{II} + G_{III}} \right)^{\eta} \tag{5.2}$$

  In order to define a model using the mixed-mode law of the previous equation, G_{I_c}, G_{II_c}, G_{III_c} and η should be provided.

- Power law
  The power law equation is given in Abaqus manual [27] as:

  $$\frac{G_{equiv}}{G_{equiv_c}} = \left(\frac{G_I}{G_{I_c}} \right)^{\alpha_m} + \left(\frac{G_I I}{G_{II_c}} \right)^{\alpha_n} + \left(\frac{G_I II}{G_{III_c}} \right)^{\alpha_o} \tag{5.3}$$

  Therefore it is necessary to define: G_{I_c}, G_{II_c}, G_{III_c}, α_m, α_n and α_o.

- Reeder law
  The Reeder law is given in [27] by the following equation:

  $$\begin{aligned} G_{equiv_c} =& G_{I_c} + (G_{II_c} - G_{I_c}) \cdot \left(\frac{G_{II} + G_{III}}{G_I + G_{II} + G_{III}} \right)^{\eta} \\ &+ (G_{III_c} - G_{II_c}) \cdot \left(\frac{G_{III}}{G_{II} + G_{III}} \right) \cdot \left(\frac{G_{II} + G_{III}}{G_I + G_{II} + G_{III}} \right)^{\eta} \end{aligned} \tag{5.4}$$

  This model requires as an input the values of G_{I_c}, G_{II_c}, G_{III_c} and η. It is only available for three-dimensional problems and in case the value of G_{II_c} is equal to the value of G_{III_c},it becomes similar to the BK law described by equation 5.2.

As it has been defined in section 4.1.2 the fracture toughness for mode I is approximately

$$K_{I_c} = 1295.7 \quad \text{MPa} \cdot \sqrt{\text{mm}}$$

which according to equation 1.3 corresponds to a value of critical energy release rate for mode I of,

$$G_{I_c} = 23.98 \quad \text{MJ} \cdot \text{mm}^{-1}$$

Since the mode II fracture toughness of a metal is hard to determine experimentally, it will be assumed that its value is half of the value of K_{I_c}, therefore

$$K_{II_c} = 647.85 \quad \text{MPa} \cdot \sqrt{\text{mm}}$$

which implies that the critical energy release associated with mode II is,

$$G_{II_c} \cong 6 \quad \text{MJ} \cdot \text{mm}^{-1}.$$

For mode III the value of fracture toughness will be the same as the value of K_{I_c}. Since it won't interfere in the crack path or in the propagation of the crack, this loading mode will not be studied.

5.1.2 Crack properties definition

First thing to do in this step of the numerical model definition is to define the crack domain. This domain can establish the set of nodes to be enriched with the nodal enrichment functions and it can be defined as the entire model or just a determined partition of the model. Then the crack location and the used option, can be chosen because in the studied cases there was a fatigue pre-crack which is the crack location on the numerical model; or instead let Abaqus determine the crack location making use of the crack initiation conditions which can be defined by the user, if that is the case.

After defining the geometrical aspects of the crack it is necessary to define its fracture mechanics properties: propagation law and its characteristics. The fracture propagation criterion available in Aabqus are: virtual crack closure technique (VCCT), enhanced VCCT or a user defined criterion.

Virtual Crack Closure Technique

The VCCT propagation criterion is based on linear elastic fracture mechanics (LEFM) so, it should be used when a brittle crack propagation along predefined surfaces occurs, [27]. The VCCT is based on the premise that the strain energy released when a crack propagates a precise quantity is the same that is needed to close the crack the same quantity. This technique and its application using the finite element method is mentioned in Abaqus documentation [27] and by Krueger in [17].

For this propagation criterion the mixed mode laws are the same which has been defined in the previous section and the fracture criterion the one defined in equation 5.1.

Enhanced VCCT

This criterion is very similar to the original VCCT criterion; the main difference between the two criteria is the fracture criterion. In this criterion two critical fracture energy release rates can be defined: G_c for the onset of a crack and the G_c^P for the growth of a crack. Citing the Abaqus manual when the enhanced VCCT criterion is used in the most general case involving all the loading modes, the quantity of dissipated energy associated with the crack propagation is controlled by the equivalent strain energy release rate necessary to propagate the crack, G_{equiv}^P, rather than by the equivalent strain energy release rate to initiate the crack, G_{equiv_c}. The equations and criteria used to calculate the G_{equiv}^P are similar to those used for G_{equiv_c}.

Low-cycle fatigue

The low-cycle fatigue[1] criterion is based upon the Paris law. This criterion only can be used in a low-cycle fatigue analysis using the direct cyclic approach. The stress intensity factors and consequently the strain energy release rates are calculated based on the virtual crack closure technique.

The Paris law can only be applied between some well defined values for the stress intensity factor as has been mentioned in section 1.2.1, therefore in figure 5.2 is shown the curve used by Abaqus, where G_{th} is the threshold value for the energy release rate, G_{pl} is the value of the upper limit for the Paris law and G_c is the equivalent critical energy release

[1] The low-cycle fatigue designation is commonly associated with fatigue studies correlating cyclic plastic deformation and number of cycles to rupture. Nevertheless, Abaqus documentation uses this term for fatigue crack propagation studies; in the present thesis that meaning is used.

rate which is calculated based on the user specified mixed-mode behavior, the mixed-mode behavior options are the same which as been defined above.

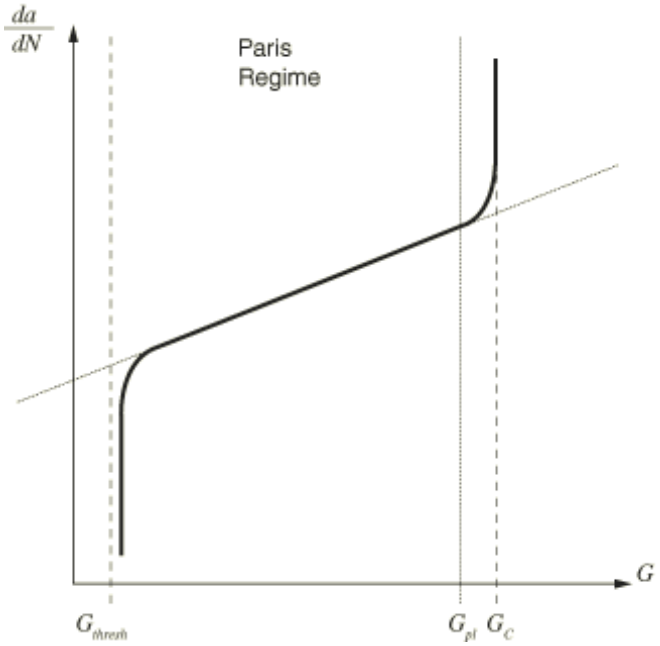

Figure 5.2: Fatigue crack growth law used in a low-cycle fatigue approach based on Paris law, figure from Abaqus documentation [27]

This propagation criterion it is not a default option so it has to be manually introduced in the input file of the model. The code lines available in Abaqus documentation [27], and that must be used, in case of the mixed-mode behavior is BK or Power, are represented above, where the c_1 and c_2 constants are determine the crack initiation, c_3 and c_4 are the Paris law constants for the used material, r_1 is given by $fracG_{th}G_c$ and according to Abaqus documentation [27] its default value is 0.01 , r_2 is given by $\frac{G_{pl}}{G_c}$ and it is also mentioned in [27] that its common value is 0.85, G_{I_c}, G_{II_c} and G_{III_c} are the critical energy release rate for each loading mode, and n is the exponent used in the mixed mode behavior.

```
fracture criterion, type=fatigue, mixed-mode behavior=BK/Power, tolerance=tol
c1,c2,c3,c4,r1,r2,GIc,GIIc,
GIIIc,n
```

Now, according to the code lines presented above, the used code lines with all parameters defined are presented.

```
fracture criterion, type=fatigue, mixed-mode behavior=BK, tolerance=0.1
0,0,85*10^-15,3.76,0.00,0.85,23.98,6,
23.98,1
```

The values of c_1 and c_2 are defined as zero because they only are used to determine the fracture criterion defined as

$$f = \frac{N}{c_1 \Delta G^{c2}} \geqslant 1.0$$

therefore if they are equal to zero implies that the above condition is always satisfied once the variable f will tend to infinite.

5.2 Preliminary studies

As the main objective of this thesis is to study the crack propagation path under mixed mode loading, it is important to do some preliminary studies which the solution is already known. Therefore the solution obtained with Abaqus can be compared with the known solution and the accuracy of the software is evaluated.

A considerable part of the experimental tests and numerical model which will be studied in this thesis work involve mixed-mode crack propagation induced by adding holes to a standard compact tension specimen. The preliminary study which will be presented is the comparison between the Abaqus solution and the solution presented by Rubinstein in [28].

In his work Rubinstein studies the influence of adding a hole to infinite plate containing an edge crack, as shown in figure 5.3.

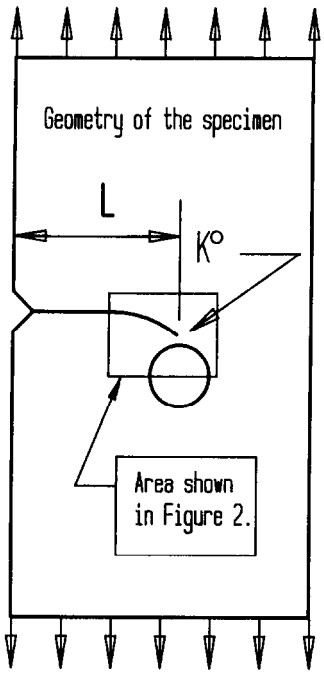

Figure 5.3: Infinite plane containing a edge and a hole, figure 1 a) of [28].

The highlighted area in figure 5.3 is shown in figure 5.4. The paths presented in this figure will be used as a comparison therm for the obtained crack path solutions using Abaqus. It has to be noticed that the crack paths presented as well as the ones which will be determined using numerical models, are obtained considering that the area of crack-hole influence is considerably smaller than the crack length, and smaller than the plate width; and that the ratio of the hole diameter and the plate width is 0.15, $d/W = 0.15$ where d is the hole diameter and W is the plate width.

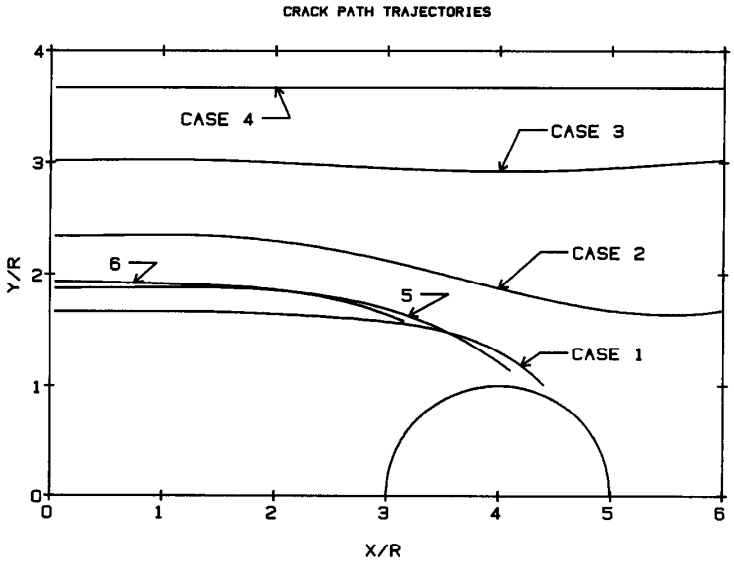

Figure 5.4: Crack path predictions presented by Rubinstein in [28], figure 2 from [28]

The used numerical model based on figure 5.3 and in the considerations related above is shown is figure 5.5, the distance between the notch of the plate and the center point of the hole is equal to $4 \cdot r$, where r is the radius of the hole. Therefor the distance between the notch and the center point of hole is 30 mm. The remaining 5 mm are used to simulate a pre-existing crack, which is used to establish the crack location into the numerical model.

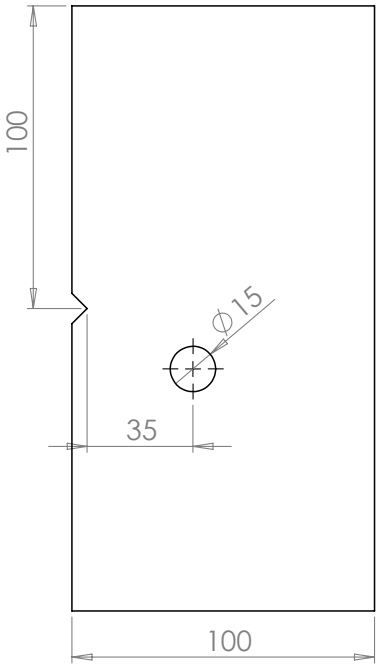

Figure 5.5: General dimensions of the numerical model.

In the numerical simulations the cases 2 and 5 of figure 5.4 will be studied. These are the most interesting ones in order to predict the mixed mode crack path. The meshed numerical model will similar to all of the numerical models, therefore the meshed model

can be observed in figure 5.6. The crack domain is meshed using a free mesh technique and all of the used elements are linear quadrilateral elements.

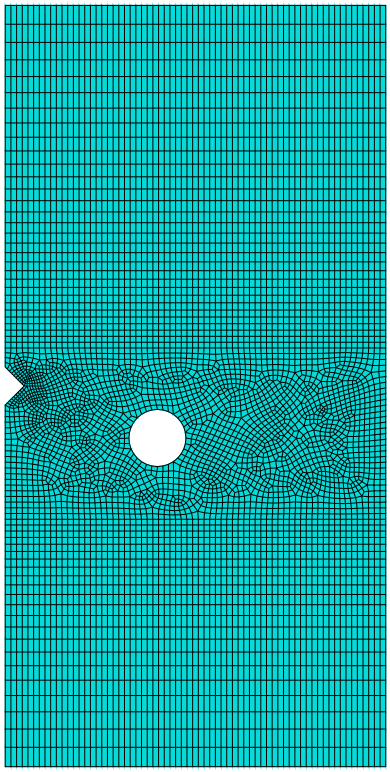

Figure 5.6: Meshed model of the infinite plate containing a hole.

The boundary conditions of the numerical model are exactly the same as shown in figure 5.3 and just one node has the horizontal displacement locked in order to fully constrain the model.

In figure 5.7 the numerical results from the Abaqus models are shown. It can be noticed that the use of plane stress elements is the appropriate for the case study. Since the first numerical models were the ones for case 5 for case 2 the numerical model using plane strain elements has not been done.

Figure 5.8 shows the comparison of the crack paths obtained with the numerical models, using plane stress elements, with the crack path from reference [28], which are shown in figure 5.4.

It can be noticed that the numerical models show a satisfactory agreement with the solution given in figure 5.4. The numerical models show a more precise solution for case 2 rather than for case 5. Also has to noticed be that the process to extract the crack path can increase the difference between the numerical models and the reference path.

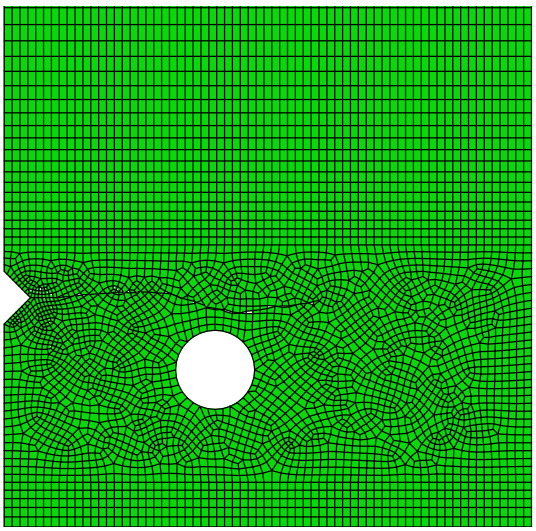

(a) 2D model for case 5 using plane strain elements.

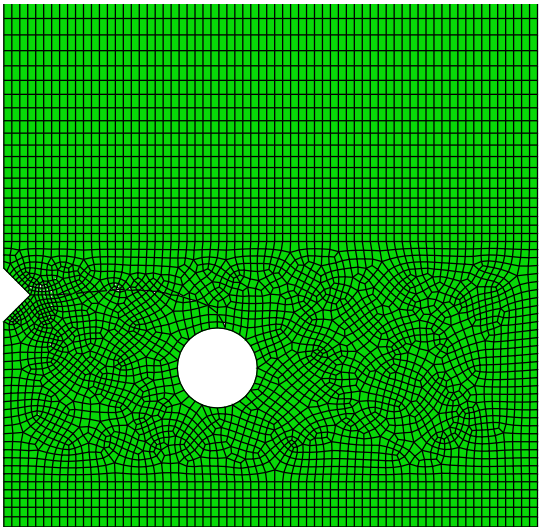

(b) Numerical results for case 5 using plane stress elements.

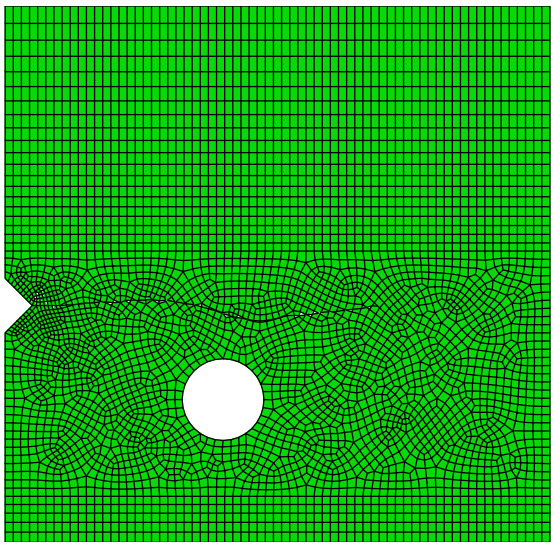

(c) Numerical results for case 2 using plane stress elements.

Figure 5.7: Numerical results from Abaqus models.

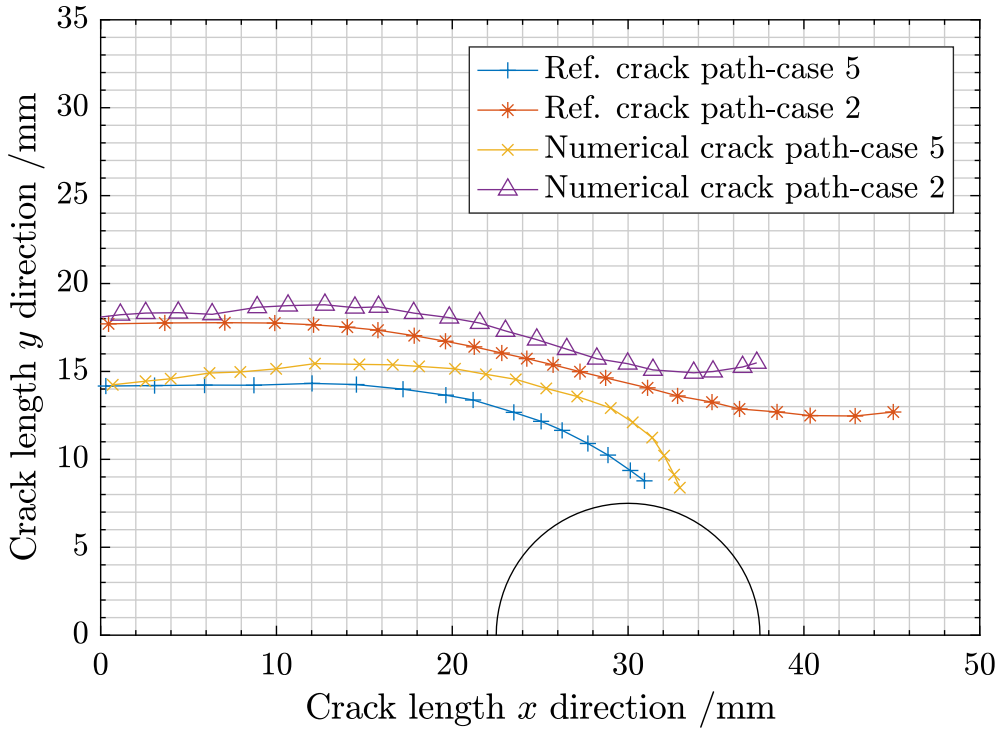

Figure 5.8: Comparison between the crack path from reference [28] and the numerical crack paths.

Nevertheless the results from the numerical models show the right tendency so it allows to conclude that the extended finite element method is a good tool to predict crack propagation paths under mixed mode. Further conclusions will be taken in the following chapters.

Chapter 6

Stress Intensity Factor calibration curve

Since this research requires the calculation of stress intensity factors (SIF) for complex situations using the finite element method (FEM), it was decided to evaluate the accuracy of the FEM in the determination of the SIF values using well documented cases: CT and 3PB specimens loaded in mode I.

The calibration curve for the specimens of interest was carried out using FEM, and compared with the ASTM E399 standard calibration.

The analyses using FEM were made using the virtual crack closure (VCCT) and the J integral tecnhiques which has been described before.

In the FEM analyses two different types of plane stress elements were used: four nodes linear elements and four nodes quadratic elements in order to compare which type of elements has better accuracy when compared with the ASTM E399 standard equation.

6.1 SIF calibration curve for Compact Tension specimen

For the compact tension (CT) specimen the geometry as well as its dimensions are shown in figure 6.1 presented below. The width of the specimen (W) is 80 mm, and the notch has 36 mm.

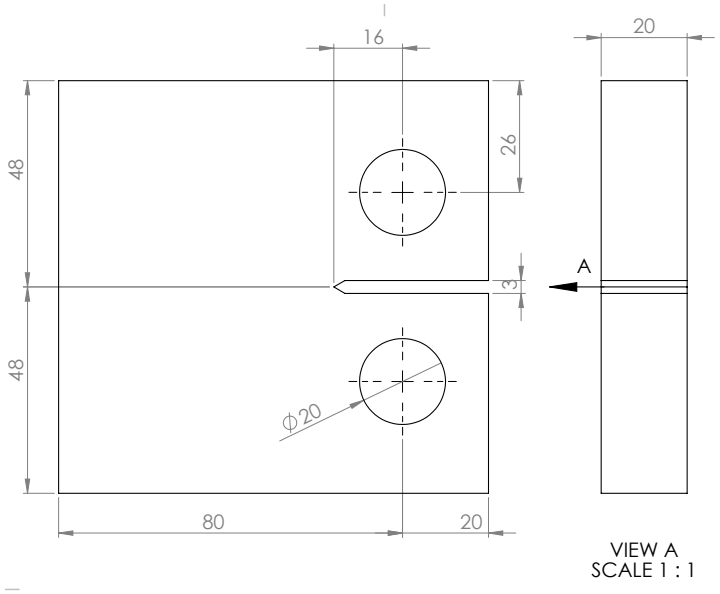

Figure 6.1: Dimensions of the studied CT specimen

The meshed model can be observed in figure 6.2. The utilized mesh consists of 1809 elements which corresponds to 57506 nodes if the used elements are quadratic (CPS8R), or to 19348 nodes if the elements are linear (CPS4R).

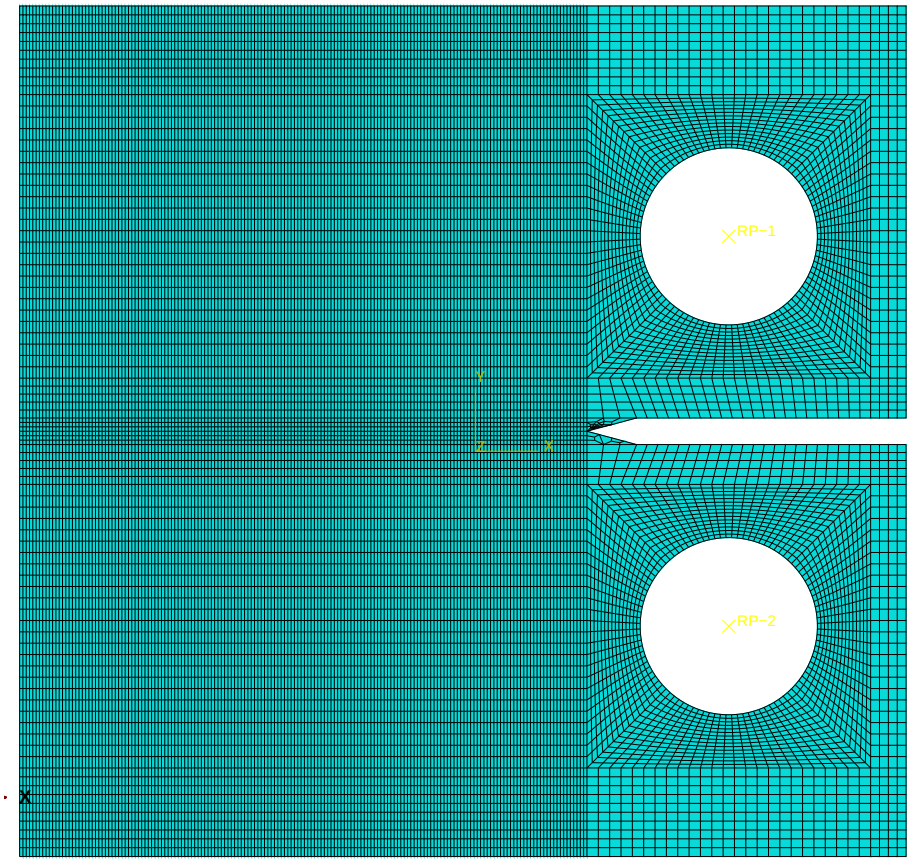

Figure 6.2: Meshed model of the CT specimen

In order to model the crack, the "seam" feature was used, and the total number of measured points was sixteen, corresponding to a maximum crack length of 64 mm and increments of the crack length of 3 mm.

Table 6.1 shows the values of the non-dimensional stress intensity factor obtained with the four nodes elements using the VCCT and the J integral, as well as with the expression from the ASTM E399 standard, where $\%\epsilon_1$ and $\%\epsilon_2$ are the percentage differences between the VCCT and ASTM E399 standard equation, and the J integral and the ASTM E399 standard equation, respectively.

Table 6.2 shows the values for the non-dimensional stress intensity factor obtained with the eight nodes element using the VCCT and the J integral techniques as well as the percentage difference between the FEM model and the ASTM E399 standard equation. Where $\%\epsilon_3$ and $\%\epsilon_4$ are the percentage difference between the VCCT and J integral techniques when compared with the ASTM E399 standard equation results, respectively.

Table 6.1: Non-dimensional SIF values for the different FEM analyses using CPS4R elements, and for the ASTM E399 standard equation.

$\frac{a}{w}$	VCCT $f(a/w)$	J Integral $f(a/w)$	ASTM E399 $f(a/w)$	$\%\epsilon_1$	$\%\epsilon_2$
0.24	4.76	4.76	4.76	0.09	0.09
0.28	5.27	5.27	5.27	0.07	0.01
0.31	5.81	5.81	5.81	0.02	0.01
0.35	6.39	6.39	6.39	0.03	0.02
0.39	7.03	7.03	7.04	0.24	0.08
0.43	7.76	7.76	7.78	0.36	0.25
0.46	8.61	8.61	8.64	0.40	0.39
0.50	9.62	9.62	9.66	0.33	0.39
0.54	10.85	10.85	10.89	0.27	0.39
0.58	12.39	12.38	12.42	0.14	0.34
0.61	14.33	14.32	14.35	0.06	0.21
0.65	16.85	16.83	16.86	0.05	0.13
0.69	20.20	20.19	20.19	0.08	0.02
0.73	24.79	24.77	24.77	0.05	0.00
0.76	31.34	31.30	31.32	0.06	0.06
0.80	41.04	41.12	41.20	0.38	0.21

Table 6.2: Non-dimensional SIF values for the different FEM analyses using CPS8R elements and for the ASTM E399 standard equation.

$\frac{a}{w}$	VCCT $f(a/w)$	J Integral $f(a/w)$	ASTM E399 $f(a/w)$	$\%\epsilon_3$	$\%\epsilon_4$
0.24	4.76	4.76	4.76	0.01	0.02
0.28	5.27	5.27	5.27	0.05	0.05
0.31	5.81	5.81	5.81	0.08	0.08
0.35	6.37	6.38	6.39	0.26	0.08
0.39	7.03	7.03	7.04	0.21	0.20
0.43	7.75	7.75	7.78	0.35	0.35
0.46	8.60	8.60	8.64	0.48	0.48
0.50	9.60	9.61	9.66	0.57	0.55
0.54	10.84	10.83	10.89	0.50	0.51
0.58	12.36	12.36	12.42	0.46	0.47
0.61	14.26	14.30	14.35	0.61	0.35
0.65	16.81	16.81	16.86	0.29	0.29
0.69	20.14	20.14	20.19	0.22	0.23
0.73	24.71	24.71	24.77	0.26	0.23
0.76	31.21	31.21	31.32	0.35	0.34
0.80	40.90	40.97	41.20	0.73	0.56

The percentage difference between FEM and ASTM E399 standard equation has been calculated using the following equation,

$$\%\epsilon = \frac{|SIF_{FEM} - SIF_{ASTME399}|}{SIF_{ASTME399}} 100 \tag{6.1}$$

The small percentage difference between methods indicates that the finite element method is a good way to determine stress intensity factors. Also it can be concluded that the difference is greater when using the CPS8R elements, which was not to be expected since it has more integrations points so the results should be more accurate. Nevertheless, the percentage difference is very small, around 0.6%, which validate the solutions obtained with the FEM models.

Figure 6.3 shows the ASTM curve for the non-dimensional stress intensity factor and the points that result from the FEM analyses, as function of a/W. The percentage difference between the FEM models and the values of the equation provided by the ASTM E399 standard are given as function of a/w in figure 6.4.

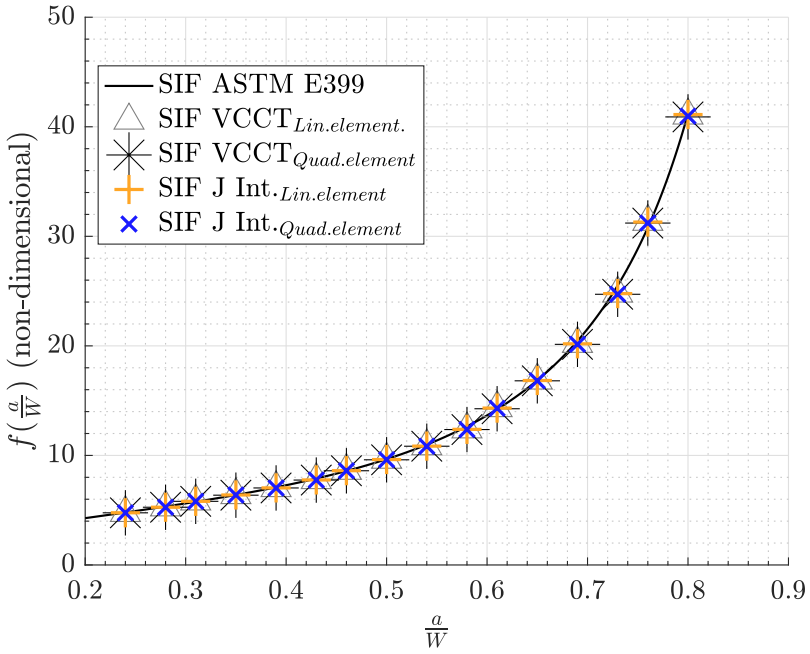

Figure 6.3: Non-dimensional SIF values obtained with FEM and the curve from ASTM E399 standard equation.

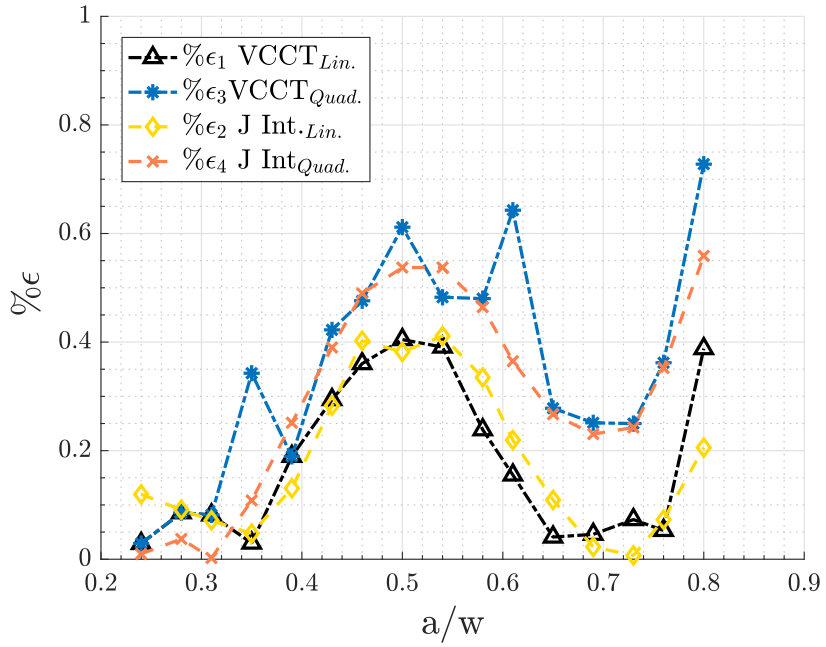

Figure 6.4: Percentage difference between the FEM results and the ASTM E399 standard equation.

6.2 SIF calibration curve for Three Point Bend specimen

The three point bend (3PB) specimen geometry and dimensions are shown in figure 6.5, the width (W) of specimen is 40 mm and the notch has 10 mm.

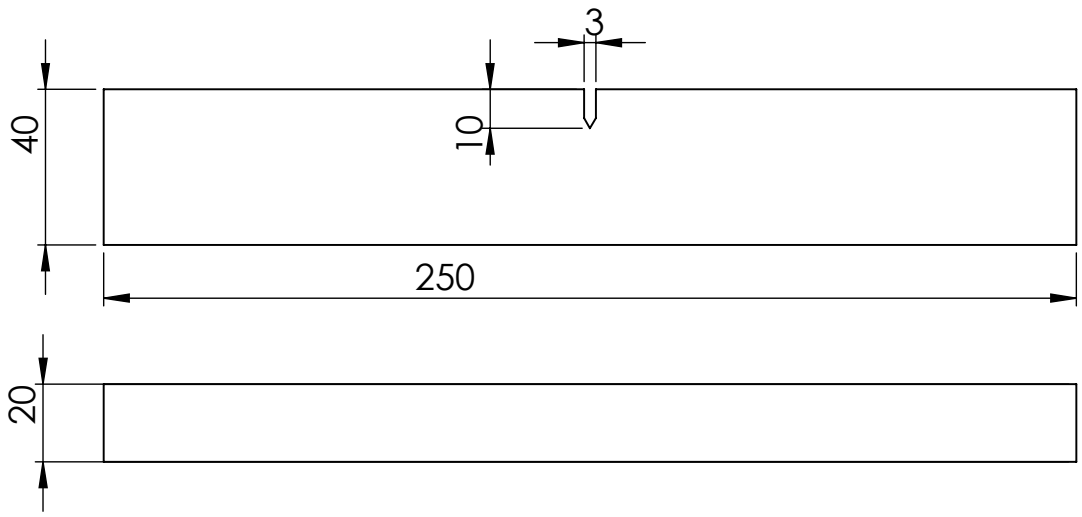

Figure 6.5: Three point bend specimen geometry and dimensions.

The used model can be observed in figure 6.6. The process to determine the non-dimensional stress intensity factors is very similar to the process used for the CT specimen. In this case the mesh was constituted by 26361 elements. If the mesh utilizes linear quadrilateral elements (CPS4R) it has 26821 nodes; if the elements are quadratic quadrilateral

(CPS8R), the mesh has 80002 nodes.

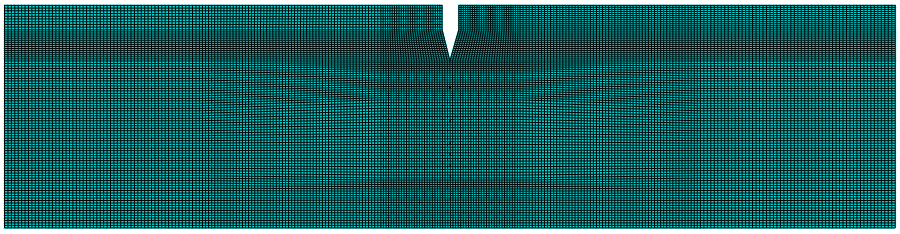

Figure 6.6: Three point bend meshed model.

The initial crack length has 13 mm which corresponds to an initial increment of 3 mm, the crack length is determined by sum the notch dimension with the length of the propagated crack. The other increments have the value of 2 mm and the final value of the crack length is 35 mm, for a total of 12 measuring points.

Table 6.3 shows the values obtained with the FEM analyses, using the CPS4R elements, and with the ASTM E399 standard equation for the 3PB specimen. The table also shows the difference between FEM and ASTM E399 standard equation, where $\%\epsilon_5$ and $\%\epsilon_6$ are respectively the percentage differences between the VCCT and J integral results compared with the ASTM E399 standard equation values.

Table 6.3: Non-dimensional SIF values for the different FEM analyses using CPS4R elements and for the ASTM E399 standard equation.

	VCCT	J Integral	ASTM E399		
$\frac{a}{w}$	$f(a/w)$	$f(a/w)$	$f(a/w)$	$\%\epsilon_1$	$\%\epsilon_2$
0.33	1.47	1.61	1.62	9.16	0.48
0.38	1.65	1.84	1.85	11.04	0.53
0.43	1.99	2.11	2.13	6.38	0.62
0.48	2.45	2.45	2.46	0.72	0.70
0.53	2.87	2.87	2.89	0.75	0.74
0.58	3.41	3.41	3.43	0.71	0.67
0.63	4.41	4.14	4.16	0.64	0.53
0.68	5.16	5.17	5.18	0.33	0.29
0.73	6.67	6.68	6.67	0.05	0.08
0.78	8.62	9.08	9.04	4.61	0.37
0.83	11.90	13.30	13.22	10.01	0.63
0.88	20.40	22.17	21.99	7.25	0.80

Table 6.4 shows the values obtained with the FEM analyses, using the CPS8R elements, and with the ASTM E399 standard equation for the 3PB specimen. The table also shows the difference between the FEM results and the ASTM E399 standard equation, where $\%\epsilon_7$ and $\%\epsilon_8$ are respectively the percentage differences between the VCCT and the J integral results compared with the ASTM E399 standard equation values.

The behavior of the non-dimensional stress intensity factor with the increase of the relation a/W can be observed in figure 6.7, where the results obtained with the finite element method and the curve from the ASTM E399 standard equation are presented.

Figure 6.8 shows the percentage difference distribution as function of a/W. Analyzing the error it can be concluded that in the case of 3PB specimen the VCCT technique shows a large dispersion when the a/W ratio is small; the same happens when it gets bigger,

Table 6.4: Non-dimensional SIF values for the different FEM analyses using CPS8R elements and for the ASTM E399 standard equation.

$\frac{a}{w}$	VCCT $f(a/w)$	J Integral $f(a/w)$	ASTM E399 $f(a/w)$	$\%\epsilon_1$	$\%\epsilon_2$
0.33	1.47	1.61	1.62	9.09	0.74
0.38	1.64	1.84	1.85	11.25	0.78
0.43	1.97	2.11	2.13	7.37	0.90
0.48	2.44	2.44	2.46	1.04	1.02
0.53	2.86	2.86	2.89	1.10	1.08
0.58	3.40	3.40	3.43	1.09	1.09
0.63	4.12	4.12	4.16	1.01	0.98
0.68	5.14	5.14	5.18	0.84	0.82
0.73	6.63	6.63	6.67	0.65	0.61
0.78	8.62	9.01	9.04	4.64	0.36
0.83	11.78	13.22	13.22	10.86	0.04
0.88	20.00	21.90	21.99	9.07	0.41

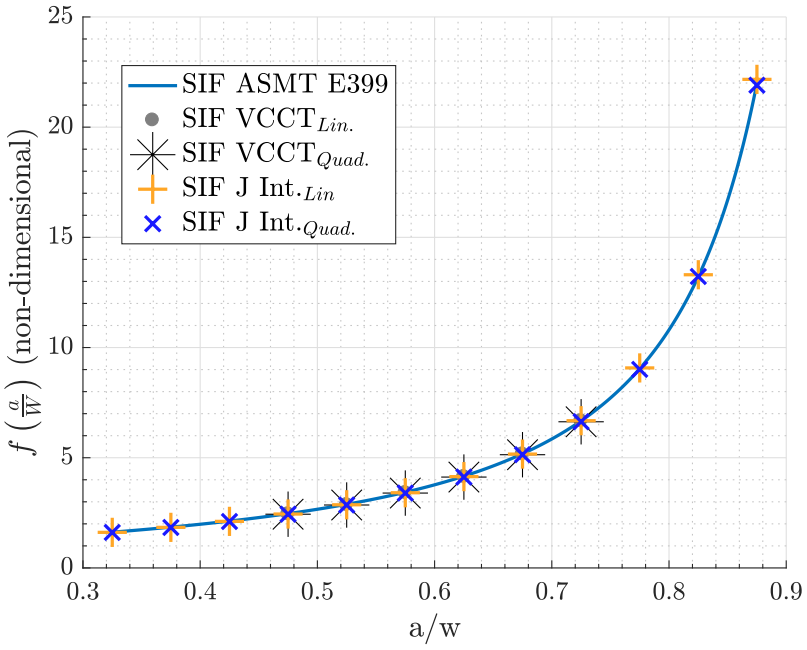

Figure 6.7: Non-dimensional SIF values obtained with FEM and the curve from the ASTM E399 standard equation.

which leads to a considerable percentage difference for values of a/W that do not belong to the range between 0.48 and 0.73.
When the J integral technique is used the results are always similar to the values of the ASTM E399 standard equation.

It can be concluded that the finite element method can be used to determine stress intensity factors for the 3PB specimen when the J integral technique is used. In case the chosen technique were the VCCT, the values of a/W should be between 0.48 and 0.73 in order to have values more identical to the values of the equation provided by the ASTM

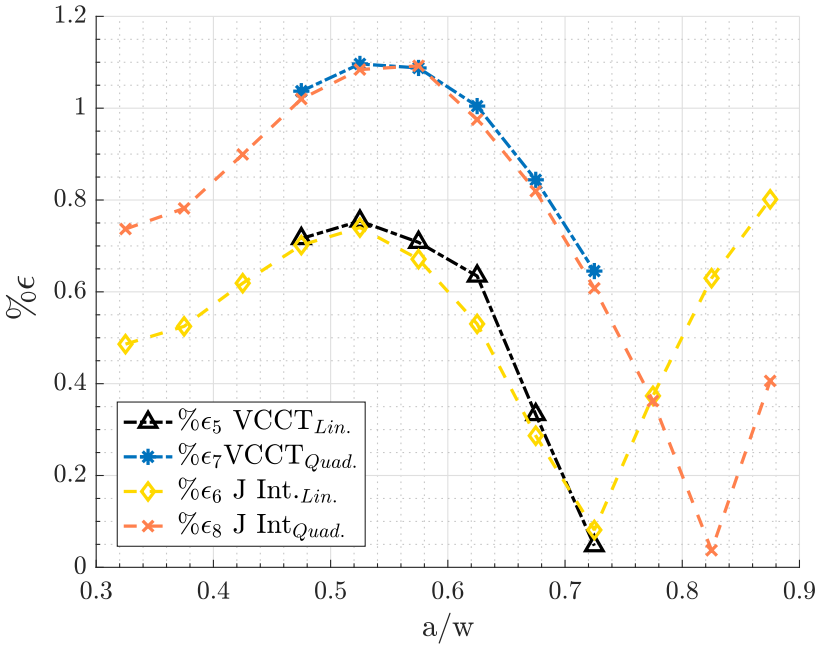

Figure 6.8: Percentage difference between the FEM results and the ASTM E399 standard equation.

E399 standard.

Chapter 7

Experimental validation procedure: pre-cracking

It was necessary to prepare the specimens before do the experimental procedure in order to determine the crack path under mix mode conditions. This preparation consists of adding a fatigue pre-crack grown under mode one loading. The recommendations of the ASTM E399 standard, [29], and BSI DD 19:1972 procedure, [30], were followed for this purpose.

7.1 Determination of the pre-cracking load

To ensure that the plastic region in the crack tip is small enough so it will not affect the mechanical properties of the material when the crack propagations test starts, it is necessary that during the fatigue pre-cracking process, in mode I, the value of the stress intensity factor, K_I do not exceed some reference values. According to ASTM E399 standard, [29], the maximum value for the stress intensity factor, K_{max}, during the process of fatigue pre-cracking shall not exceed 80% of the estimated value for the stress intensity factor K_Q. When the value of K_{max} is determined, it is possible to calculate the load P_{max} which will make the crack grow but ensures that the plastic zone will remain small.

Another way to determine the value of K_{max} exists, according to BSI DD19:1972 procedure, [30]. The value of K_I during the pre-cracking propagation should satisfy the condition of equation 7.1.

$$K < 0.63\sigma_{Yield}B^{\frac{1}{2}} \tag{7.1}$$

7.1.1 Compact tension specimen

Determination of P_{max} according to ASTM E399 standard

The stress intensity factor for the CT specimen is given by, [29]:

$$K = \frac{P}{BW^{\frac{1}{2}}} f\left(\frac{a}{W}\right) \tag{7.2}$$

where B is the thickness of the specimen, W is the specimen width and $f\left(a/W\right)$ is the non-dimensional stress intensity factor calibration, given by:

$$f\left(\frac{a}{W}\right) = \frac{\left(2+\frac{a}{W}\right)\left[0.76+4.8\frac{a}{w}-11.58\left(\frac{a}{W}\right)^2+11.43\left(\frac{a}{W}\right)^3-4.08\left(\frac{a}{W}\right)^4\right]}{\left(4-\frac{a}{W}\right)^{\frac{3}{2}}} \tag{7.3}$$

The length of the fatigue pre-crack according to ASTM E647 standard, [31], for the CT specimen must satisfy the next conditions,

$$\begin{aligned} a_i &= 0.1B \\ a_i &= h \\ a_i &= 1mm \end{aligned} \tag{7.4}$$

The fatigue pre-crack takes the greater value of the three. The variable h corresponds to the height of the notch.

For the CT specimen that is being studied, $B = 2$ mm and $h = 3$ mm, so the minimum value of the fatigue pre-crack will be 3 mm. The value of a used in equation 7.3 is given by the sum of the length of the fatigue pre-crack plus the distance a_n, as it can be observed in figure 7.1.

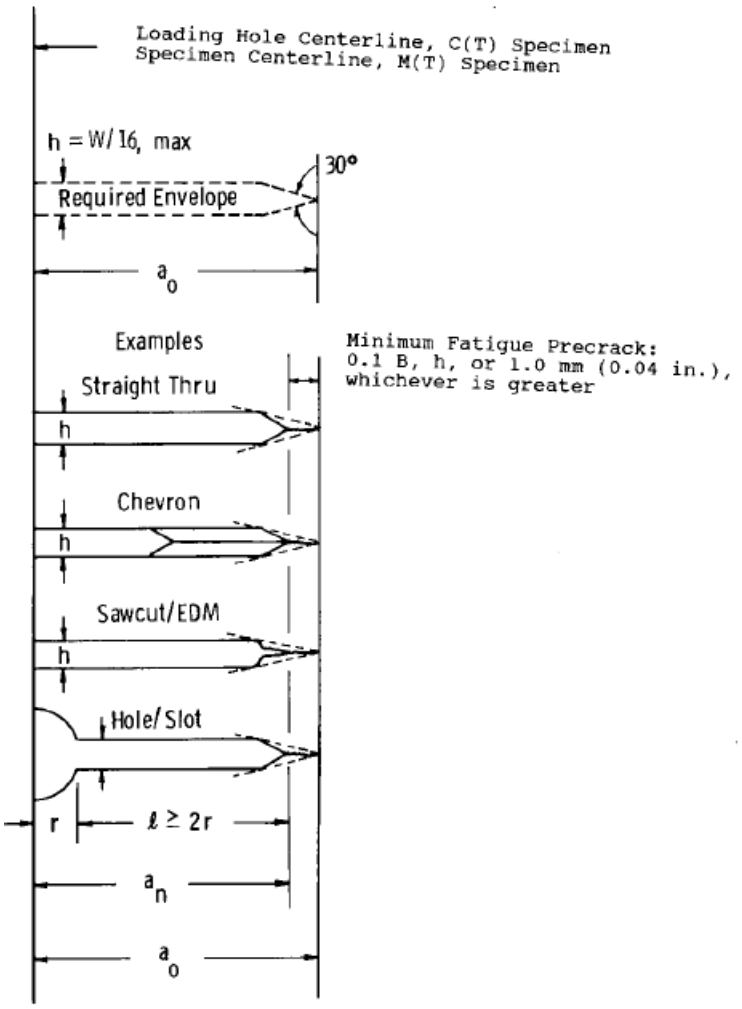

Figure 7.1: Notch detail. Source: ASTM E647, [31].

With all dimensions defined, as shown in figure 6.1, the value of maximum fatigue load P_{max} can be calculated. In order to determine the non-dimensional stress intensity factor the length of the fatigue pre-crack will be two times bigger than the minimum value determined according to the condition of equation 7.4. Therefore the crack length used

to calculate the non-dimensional stress intensity factor is 22 mm and the correspondent value is:

$$f\left(\frac{a}{W}\right) = 5.2655$$

For the used material the value of K_Q will be equal to the value of K_c given by the equations 4.3 or 4.5. Affecting it by a safety factor of 2 in order to guarantee that the load P_{max} do not cause a large plastic deformation ahead of the crack tip, the value of the estimated fracture toughness is $K_Q = 20.5$ MPa$\sqrt{\text{m}}$. Multiplying the value of K_Q by 0.8 the value of K_{max} is determined, which takes the value of 16.4 MPa$\sqrt{\text{m}}$.

Using the equation for the stress intensity factor for the CT specimen, equation 7.2, the value of the maximum pre-cracking fatigue load can be calculated, as follows:

$$16.4 \cdot 10^6 = \frac{P_{max}}{20 \cdot 10^{-3} \cdot (80 \cdot 10^{-3})^{\frac{1}{2}}} \cdot 5.2655 \tag{7.5}$$

Solving equation 7.5 results,

$$P_{max} = 17619 \quad \text{N}$$

Determination of P_{max} according to BSI DD 19:1972 procedure

According to this standard the maximum value of the stress intensity factor during the fatigue pre-crack process is given by equation 7.1, therefore,

$$K_{max} < 0.63 \cdot 260 \cdot \left(20 \cdot 10^{-3}\right)^{\frac{1}{2}} \tag{7.6}$$

which results in a value of K_{max} equal to 23.16 MPa$\sqrt{m}$.

Matching the result of equation 7.6 and the equation for the stress intensity factor of the CT specimen, equation 7.2, the maximum fatigue load P_{max} according to this standard is determined by solving,

$$23.16 = \frac{P_{max}}{20 \cdot 10^{-3} \cdot (80 \cdot 10^{-3})^{\frac{1}{2}}} \cdot 5.2655 \tag{7.7}$$

From the resolution of the equation 7.7 the maximum value for the fatigue pre-crack load is 24881 N.

7.1.2 Three points bend specimen

The maximum fatigue load P_{max} using the calculation methods of the ASTM E399, [29], and of BSI DD 19:1972, [30], standards will now be determined for the 3PB specimen.

The stress intensity factor calibration is given by,

$$K = \frac{P \cdot S}{B \cdot W^{\frac{3}{2}}} \cdot f\left(\frac{a}{W}\right) \tag{7.8}$$

where S is the distance between supports during the pre-crack procedure and, the non-dimensional SIF for the 3PB specimen is given by,

$$f\left(\frac{a}{W}\right) = 3 \cdot \sqrt{\frac{a}{W}} \cdot \frac{1.99 - \left(\frac{a}{w}\right) \cdot \left(1 - \frac{a}{w}\right) \cdot \left[2.15 - 3.93\frac{a}{W} + 2.7\left(\frac{a}{W}\right)^2\right]}{2 + \left(1 + 2 \cdot \frac{a}{w}\right) \cdot \left(1 - \frac{a}{W}\right)^{\frac{3}{2}}} \tag{7.9}$$

The 3PB specimen being studied is shown in figure 7.2; its geometry is slightly different from the geometry shown in figure 6.5. The difference consists of a change in the width of the specimen. For the geometry used in section 6.2 the width was 40 mm and for the present geometry it is 60 mm. This modification was made because the crack deviation due to mixed-mode loading is more visible for the 60 mm width specimen. In this case the length of the fatigue pre-crack will also be at least 3 mm, therefore and according to the considerations taken to determine P_{max} for the CT specimen, the fatigue pre-crack length used for calculations was 6 mm, which implies that the crack length a, utilized on the determination of the maximum fatigue load was 16 mm.

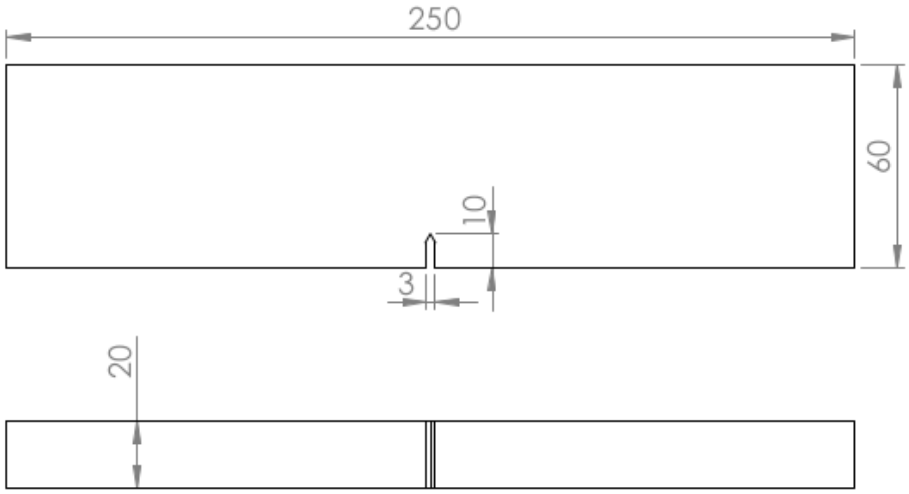

Figure 7.2: Three point bend specimen

Determination of P_{max} according to ASTM E399 standard, [29]

For the 3PB specimen of interest and for the given initial crack length the non-dimensional SIF takes the value of,

$$f\left(\frac{a}{W}\right) = 1.3973$$

The value of the variable S, according to the ASTM E399, [29], is equal to $4 \cdot W$ which results in a value of 240 mm, for safety reasons, since the displacement of the specimen is not constrained in the horizontal direction if the distance between supports was of 240 mm only remains 5mm of material on each side of the specimen what could cause the specimen to slide of the supports; and limitation of the specimen length the variable S will take the value of 230 mm. As the material of the CT specimen is the same of the 3BP specimen the value of the estimated fracture toughness is the same for both, K_Q =20.5 MPa$\sqrt{m}$. Bearing in mind the safety factor used in the calculation of P_{max} for the CT specimen, this implies that the maximum value for the stress intensity factor during the pre-crack process will be the same as the one used for the CT specimen.

Therefore the value of the maximum fatigue load is given by,

$$16.4 \cdot 10^6 = \frac{P_{max} \cdot 230 \cdot 10^{-3}}{20 \cdot 10^{-3} \cdot (40 \cdot 10^{-3})^{\frac{3}{2}}} \cdot 1.3973 \tag{7.10}$$

resulting in a value for

$$P_{max} \cong 15000\text{N}$$

Determination of P_{max} according to the BSI DD19:1972 procedure, [30]

Applying the same calculation procedure as it was used for the CT specimen the value of P_{max} is given by,

$$23.16 = \frac{P_{max} \cdot 230 \cdot 10^{-3}}{20 \cdot 10^{-3} \cdot (40 \cdot 10^{-3})^{\frac{3}{2}}} \cdot 1.3973 \tag{7.11}$$

Solving the equation 7.11 returns that,

$$P_{max} = 21183\text{N}$$

.

In both cases, CT and 3PB specimens, the used value for P_{max} was the lower value obtained for each specimen, which corresponds to a value of 17619 N for the CT specimen and 15000 N for the 3PB specimen. It is also noticed that the value of K_{max} is the same for both specimen, because it only depends on the mechanical properties of the material and on the thickness of the specimen, which are the same for both.

Chapter 8

Experimental validation procedure: crack-paths

All the steps of the experimental validation of the finite element method (FEM) models, will be presented in this chapter. The obtained experimental results will be now be presented and analysed. As mentioned before two different types of specimens were used. In the following subsections the final and used geometry, will be shown as well as the experimental results for each one.

8.1 Compact tension specimen - modified geometry

For the compact tension specimen, two different configurations where used in order to have different crack paths in each case and have more case studies to better validate (or not) the numerical model. Both configurations have the same origin, which is adding an hole to the CT specimen. The differences between them are the hole center point coordinates and the hole diameter. Figure 8.1 shows the hole center coordinates as well as the hole dimension; all other dimensions can be observed in figure 6.1.

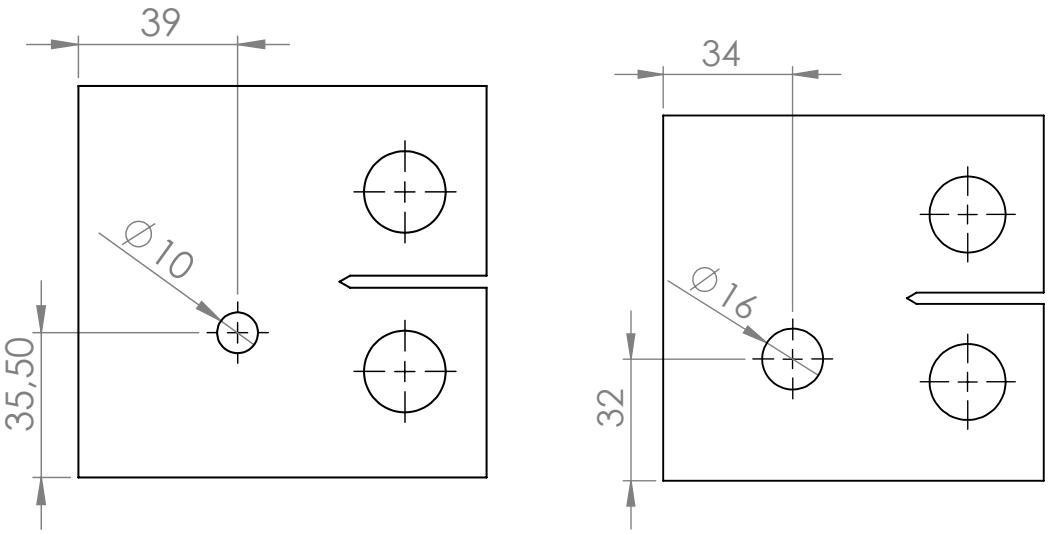

(a) CT specimen 10 mm hole configuration. (b) CT specimen 16 mm hole configuration.

Figure 8.1: CT specimen configurations.

Figure 8.2 shows the maximum principal stress field in a compact tension specimen without additional hole and in a compact tension specimen with an additional hole, those

stress fields were obtained for the same crack length as well as for the same load amplitude.

Using the J integral technique to determine the stress intensity factors for both represented situations the values are presented in the above table.

Therefore analysing the values of K_{II} it can be concluded that mode II loading is imposed by the additional hole.

Before conducting the fatigue tests to observe the crack path propagation on the modified specimens, it is necessary to evaluate the cyclic load for stable propagation.

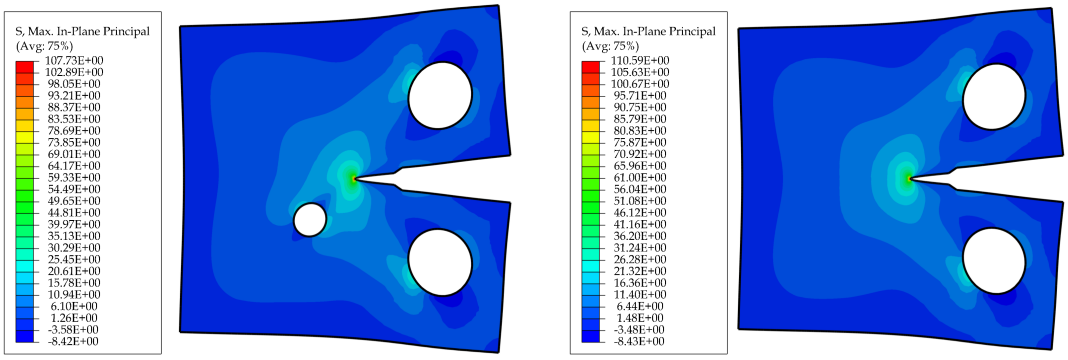

(a) CT specimen 10 mm hole configuration maximum stress field representation.

(b) Standard CT specimen maximum principal stress field representation.

Figure 8.2: CT specimen maximum principal stress (MPa) field distribution for different configurations.

Table 8.1: K_I and K_{II} values for the cases represented in figure 8.2

	K_I /MPa$\sqrt{\text{mm}}$	K_{II} /MPa$\sqrt{mm}$
Model 8.2b	107.2	$\cong 0$
Model 8.2a	112.1	-2.4

8.1.1 Determination of the maximum fatigue load during the crack propagation

According to the NASGRO material database, a crack growth rate approximately of 1 mm per 10 000 cycles is associated with a value of ΔK equal to 260 MPa$\cdot\sqrt{\text{mm}}$. Utilizing equations 7.2 and 7.3 it is possible to calculate the load related with this crack growth rate and the initial conditions of the specimen such as the fatigue pre-crack length and dimensions. The fatigue pre-crack for the studied specimens has a mean length of 6 mm; so from equation 7.3 results,

$$f\left(\frac{a}{w}\right) = 2.7175 \tag{8.1}$$

Consequently the result of equation 7.2 is,

$$P_{propagation} = 17115\text{N} \tag{8.2}$$

and applying a safety factor of 2 the applied load is approximately of 8500 N. The safety factor is applied because the material is not perfect and can contain some internal defects such as inclusions and it has to be taken in account that residual stress due to manufacturing process of the specimen may exist.

8.1.2 Experimental setup

Since mode II loading is only due to the additional hole, as it has been proved above by the results presented in table 8.1, the experimental setup is the same for the fatigue pre-crack propagation and for the crack propagation test and it is shown in figure 8.3.

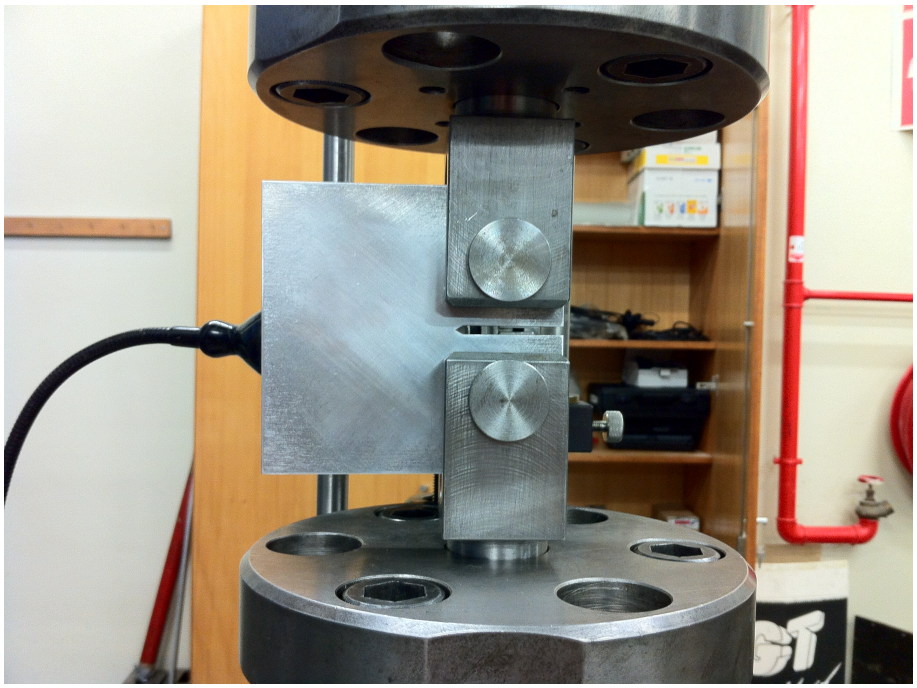

Figure 8.3: Experimental setup used for CT specimens.

8.1.3 Experimental crack path

The experimental crack paths are shown in figure 8.4 for both configurations. As it can be observed, in both cases the crack goes through the additional hole.

(a) CT specimen 10 mm hole configuration experimental crack path.

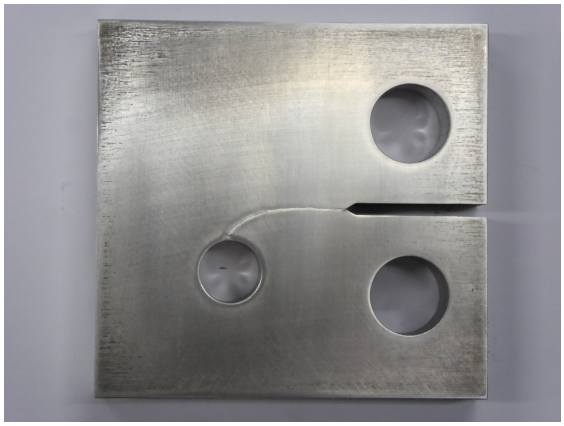

(b) CT specimen 16 mm hole configuration experimental crack path.

Figure 8.4: CT specimen crack path for different configurations.

Figure 8.5 shows the crack surface for both configurations. From the analysis of figures 8.5a and 8.5b it can be concluded that for the specimen with a 16 mm hole diameter the

propagation near the hole is unstable, and it can be observed the formation of "shear lips", which are an indication of plane stress crack propagation.

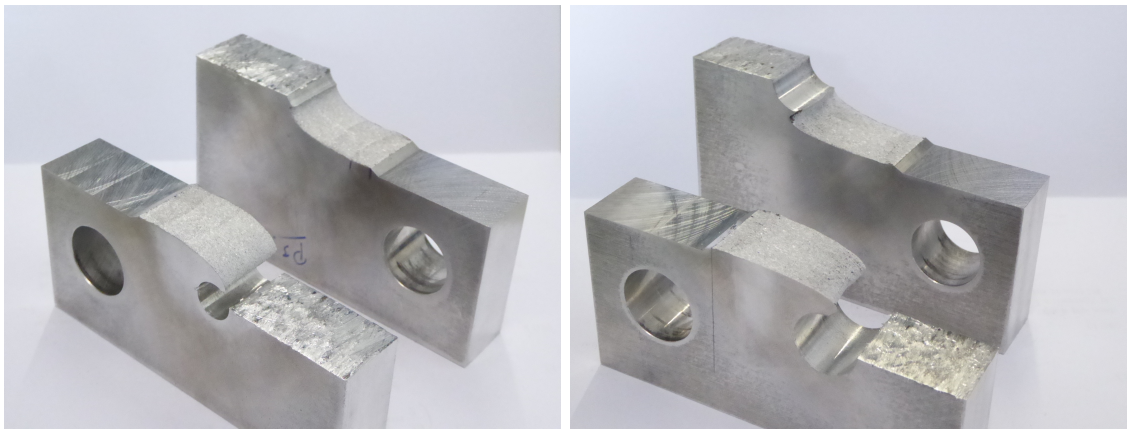

(a) CT specimen 10 mm hole configuration experimental crack surface.

(b) CT specimen 16 mm hole configuration experimental crack surface.

Figure 8.5: CT specimen crack surface for the studied configurations.

8.1.4 Numerical models and results

The numerical models and results will now be presented. Firstly the numerical model of the CT specimen which contains the 10 millimeter diameter hole will be presented, as well as a comparison between the numerical and experimental paths for this configuration.

Three-dimensional numerical models and results of the CT specimen with a 10 millimeter diameter hole.

Figure 8.6 shows the meshed models used to predict the crack path using the extended finite element method. The model represented in figure 8.6a is constituted only by a structured mesh where the crack domain contains elements with one millimeter length.

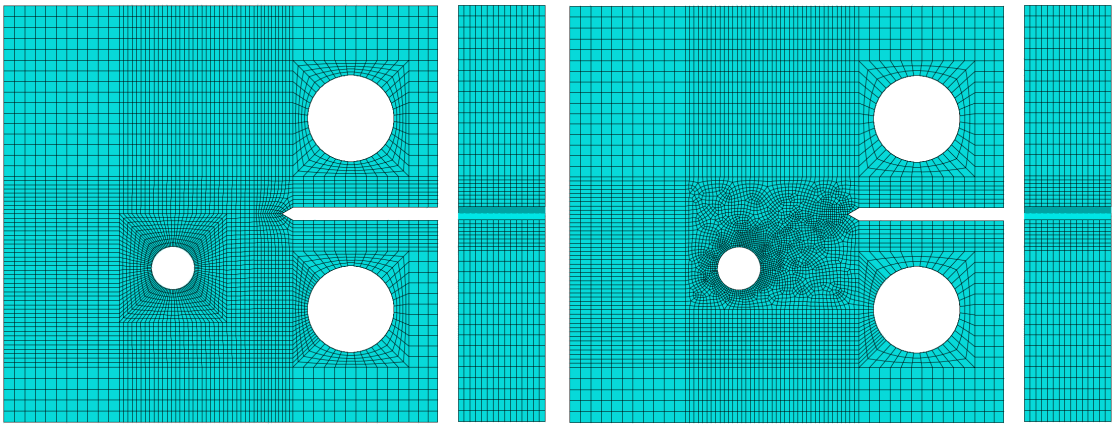

(a) Meshed model of a CT specimen 10 mm hole configuration, using a structural mesh on the crack domain.

(b) Meshed model of a CT specimen 10 mm hole configuration, using a free mesh on the crack domain.

Figure 8.6: CT specimen crack surface for the studied configurations.

On the other hand the model represented in figure 8.6b was meshed using as mesh control technique "free" on the crack domain regions, all the other regions were meshed using the structured technique.

It was to be expected that the results of the numerical models should be at least similar, independently of the used mesh control technique but the results are very different as it is shown in figure 8.7.

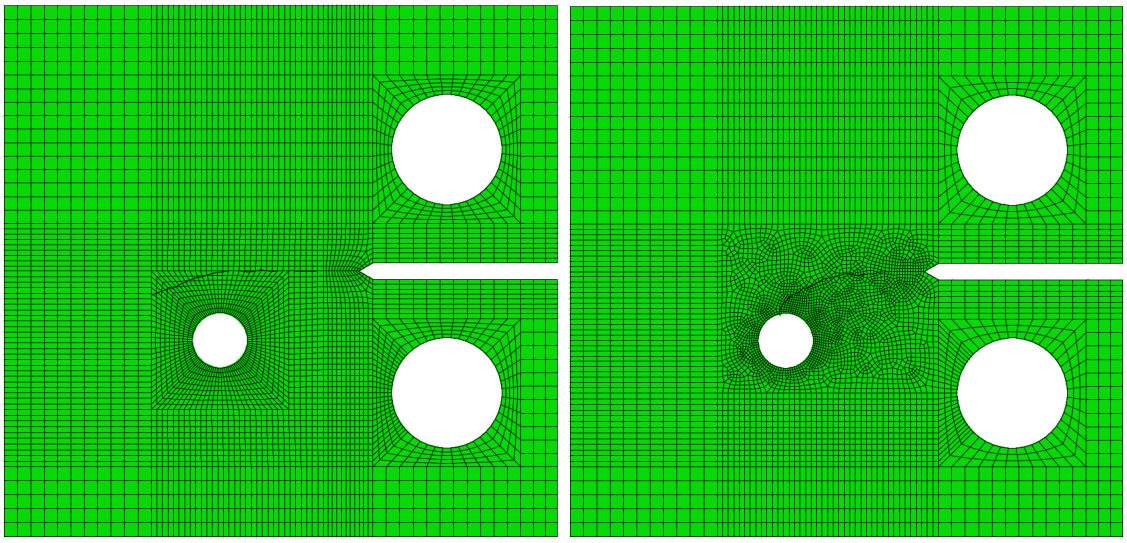

(a) Crack path for a full structural mesh control technique meshed model.

(b) Crack path for a free mesh control technique on the crack domain.

Figure 8.7: Numerical crack paths for a CT specimen with a 10 millimeter hole.

The crack path obtained with the model represented in figures 8.6a and 8.7a do not need a deeper comparison with the experimental path since it is completely different. This difference probably can be explained by the different type of enrichment functions used to calculate the stress intensity factors at the crack tip.

A completely different result was obtained with the model represented in figures 8.6b and 8.7b. In this case a more detailed comparison between the numerical and experimental results can be interesting. In order to do this comparison, the crack path points for each case were represented in the same plot, as it is shown in figure 8.8. As can be observed the 3D numerical model when using as mesh control technique, for the crack domain, free, shows a good agreement with the crack path obtained experimentally.

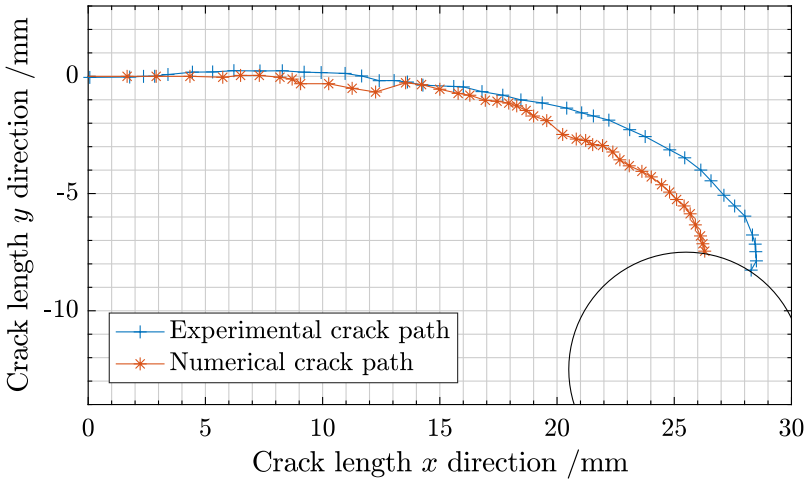

Figure 8.8: Crack path comparison between the path the model represented in figure 8.7b and the experimental path.

Two dimensional numerical models and results of the CT specimen with a 10 millimeter diameter hole.

Now the results for the CT specimen with an additional hole of 10 mm will be presented for two-dimensional numerical models. The two-dimensional numerical models were executed using two different methods, the extended finite element method, implemented in Abaqus, and the NNRPIM method, a meshless method as has been described above. As shown in the previous section, the numerical results for three-dimensional numerical models has a good agreement when compared with the experimental results, nevertheless if the two-dimensional numerical models also has a good agreement with the experimental results, it is possible to save computational time and consequently reduce the costs related to it.

Figure 8.9a shows the two-dimensional crack path. It can be observed that the path is very similar to the experimental path as shown in figure 8.4a. In order to have a better perception of the agreement between the two-dimensional model crack path results and the experimental crack path results, a comparison similar to the one made in figure 8.8 will be made for the present results. As can be observed in figure 8.10, the crack path resulting of the two-dimensional model is very similar to the one obtained in the experimental test. There is only one problem in the two-dimensional model crack path because it does not goes through the hole, figure 8.9a, which is not a realist representation but, this deviation happens on a point close to the hole so it allows to have a good perception of what will be the crack-path for the studied situation. The crack path resulting of the NNRPIM method shows that the crack path will be affected by the hole but also shows a bigger sensitivity to the effects of adding a hole to the specimen, since the crack intersects the hole earlier when compared with the experimental results.

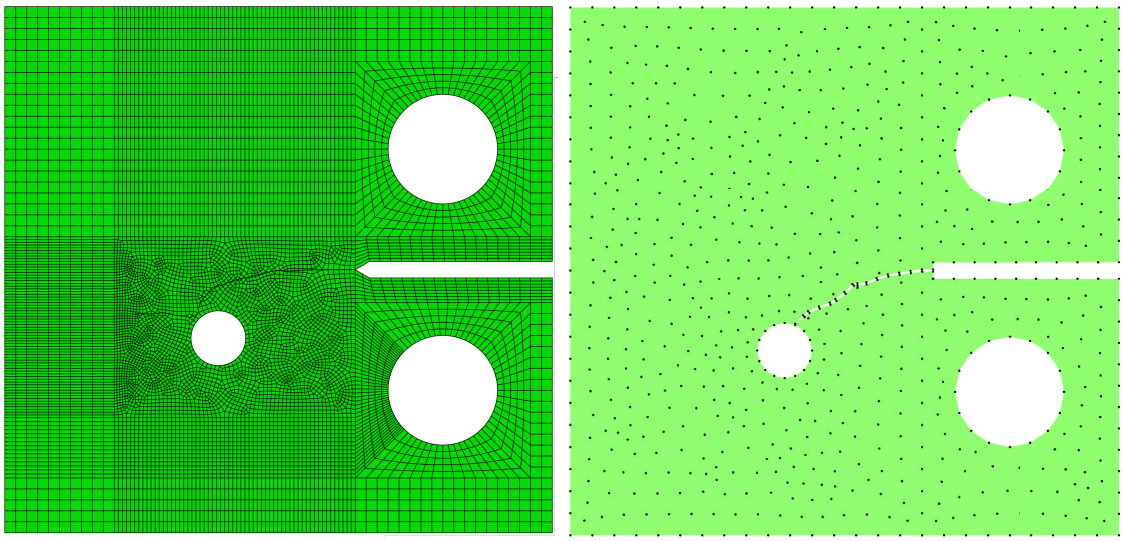

(a) Two-dimensional model crack path for a CT specimen with a 10 mm hole.

(b) Two-dimensional model crack path for a CT specimen with a 10 mm hole, using the NNRPIM method.

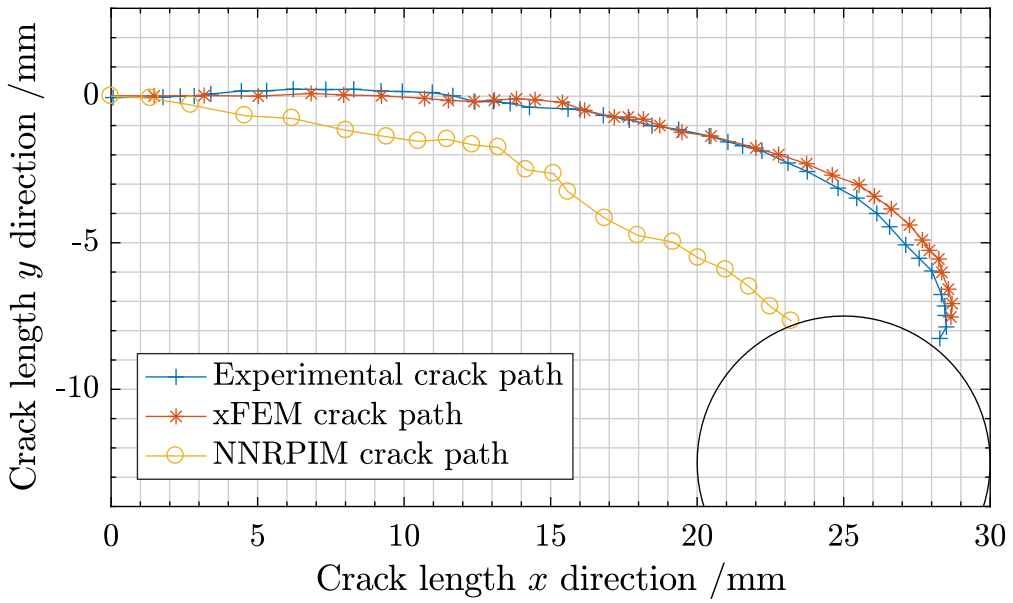

Figure 8.10: Crack path comparison between the path the 2D model represented in figure 8.9a and the experimental path.

Three-dimensional numerical models and results of the CT specimen with a 16 millimeter diameter hole.

The results of the 3 dimensional numerical models for the Ct specimen with a 16 mm hole will now be presented. Figure 8.11a shows the results of the numerical models where it is used a structured mesh and figure 8.11b shows the crack path result for a numerical model which use a unstructured mesh on the crack propagation domain.

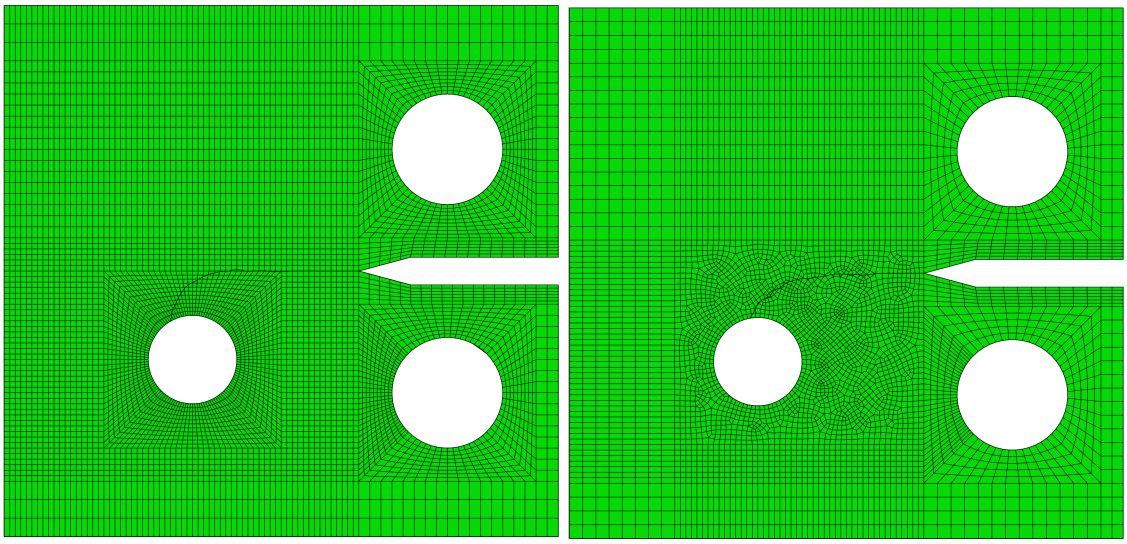

(a) Crack path for a full structural mesh control technique meshed model.

(b) Crack path for a free mesh control technique on the crack domain.

Figure 8.11: Crack path solution for the CT specimen with a 16 mm hole, 3D numerical models.

For this case both models show a good agreement with the experimental crack path result. It may occur because the hole influence on the stress field is bigger than in the case where a 10 mm hole is used, so the numerical model has more capability to predict the influence of the hole on the crack path. Therefore, a more precise comparison between the numerical and experimental results may be performed. Figure 8.12 shows the plot of the crack path resulting of the experimental procedure and, the results form the numerical models.

Analysing figure 8.12 it is possible to conclude that the model which uses a structured mesh on the crack propagation domain is also an acceptable solution for the problem, nevertheless the model which uses an unstructured mesh on the crack propagation domain is a more accurate solution when compared with the result obtained experimentally. It also can be noticed that the numerical solution for the present case is more precise than for the case of the CT specimen with a 10 mm hole, which allows to conclude that the bigger the influence of the hole in the stress field, the more accurate is the numerical solution.

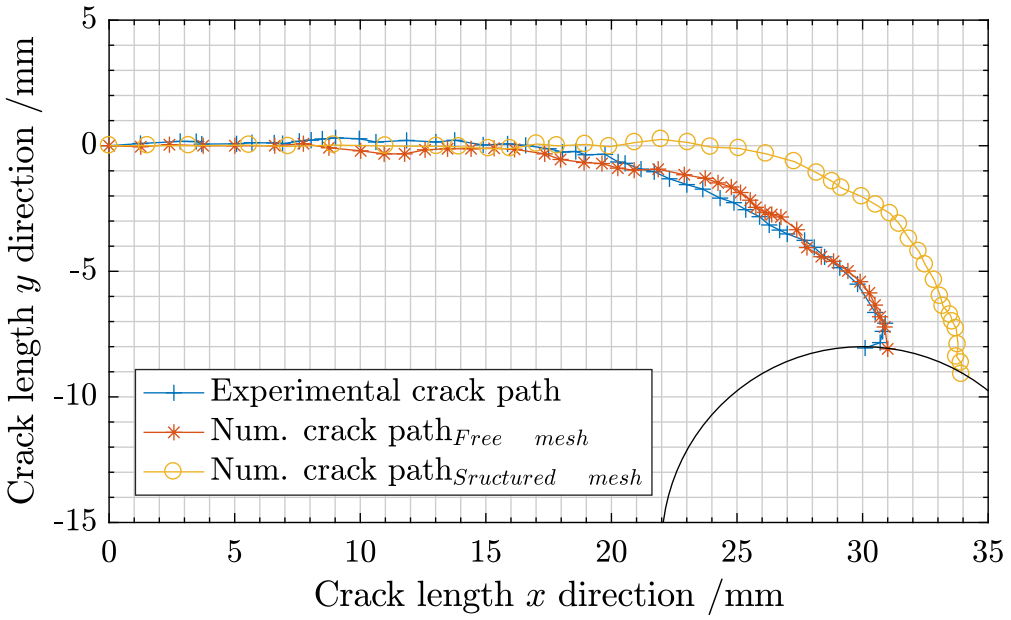

Figure 8.12: Crack path comparison between experimental procedure and numerical models results.

Two-dimensional numerical models and results of the CT specimen with a 16 millimeter diameter hole.

Similarly to the analysis performed for the CT specimen with a 10 mm hole diameter, a comparison between the experimental results and the results from the two-dimensional numerical models was also made. For the numerical analysis it were used the extended finite element (xFEM) and the NNRPIM methods. The results are shown in figures 8.13a and 8.13b for the xFEM and NNRPIM models, respectively.

It can be noticed that for this case the 2D extended finite element method model shows good agreement with the experimental results and, the NNRPIM solution is a reasonable approximation for this case. A more detailed analysis of the crack-path results of the both methods is shown in figure 8.14 where a comparison between the numerical solutions and the experimental one is done. As is shown in figure 8.14 the two-dimensional model from Abaqus shows a better agreement with the experimental result, the model solved using the NNRPIM method shows a good approximation of the crack path in particular for the point where the crack intersects the hole which is very similar to the point where the experimental path intersects it.

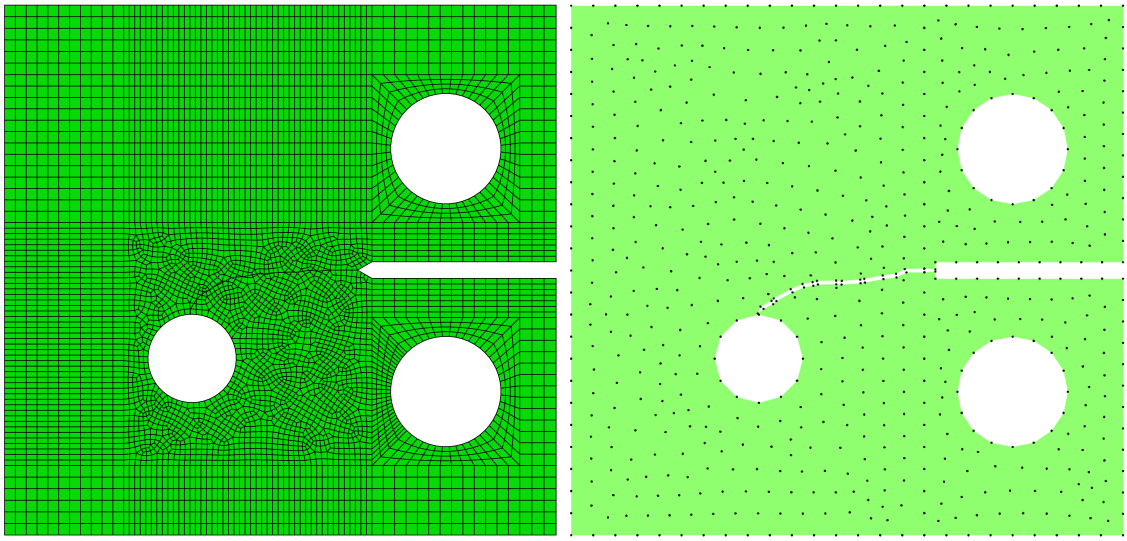

(a) Two-dimensional model for a CT specimen with a 16 mm hole, xFEM method.

(b) Two-dimensional model for a CT specimen with a 16 mm hole, NNRPIM method.

Figure 8.13: Results from the Two dimensional models for the CT specimen with a 16 mm hole.

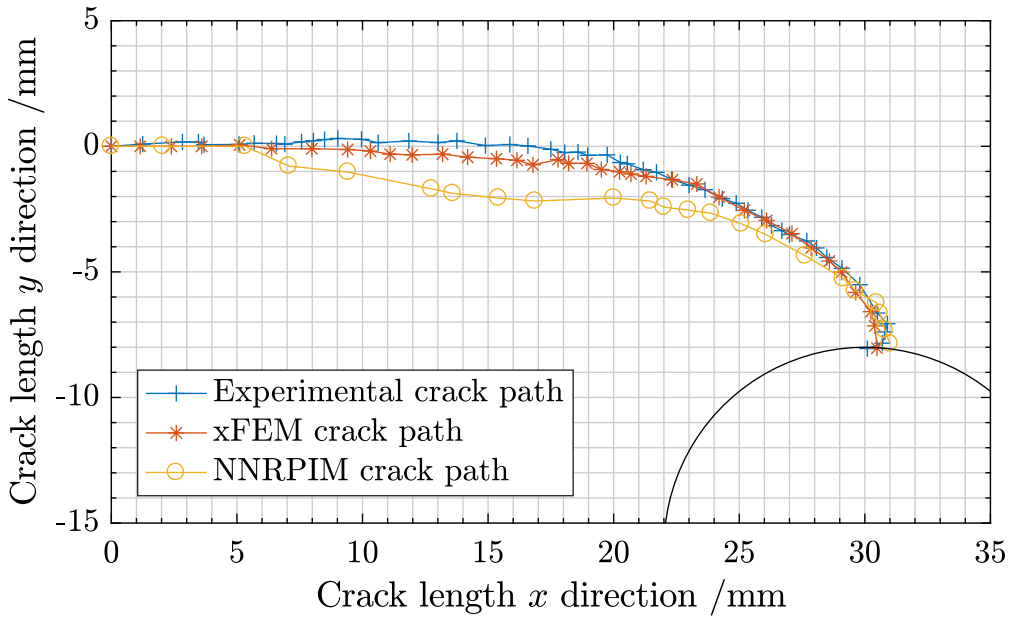

Figure 8.14: Comparison of the crack-path results of the 2D models with the experimental results.

8.1.5 Equivalent stress intensity factor determination.

Usually the available data for fatigue crack propagation are obtained for pure mode I which can lead to errors or imprecise results of the life prediction for a cracked component subjected to mixed mode loading. In order to understand if the approximation made when the fatigue life is determined using the data obtained for pure mode I and the loading subjects the cracked component to mixed mode, the stress intensity factors were determined for the modified CT specimen with a 16 mm hole. After the determination of K_I and K_{II}, equivalent stress intensity factor values were calculated. To compare the difference between using the data obtained for mode I and the data for mixed mode, the fitting resulting of the equivalent stress intensity factor points were compared with the original Paris law fitting. The procedure of data acquisition is explained in detail below.

During the experimental test, measurements of the crack length and the corresponding number of cycles were recorded. In order to calculate the values of K_I and K_{II} for each measured point, the two-dimensional model represented in figure 8.15a, the VCCT and the J integral techniques were used. Since the values obtained with each technique were very similar between them the subsequent calculations only use the values of the stress intensity factor obtained with the VCCT technique.

The obtained results are presented in table 8.2, where the values of ΔK_I, ΔK_{II}, crack length (a) and the corresponding number of cycles are shown. The crack length and number of cycles presented in table 8.2 are the mean values of the ones measured in the experimental procedure, this was made in order to determine the values of K_I and K_{II} in a mean point of the crack increment size. Also has to be noticed that the values of the crack length are an approximation of the real value and were obtained by

$$\sqrt{d_x^2 + d_y^2}$$

where d_x and d_y are respectively, the crack length measured in the horizontal and vertical directions, reference point to take all of this measures were the end of the notch. With the data available on table 8.2 is possible to determine the equivalent stress intensity factor and the crack growth ratio $^{da}/_{dN}$.

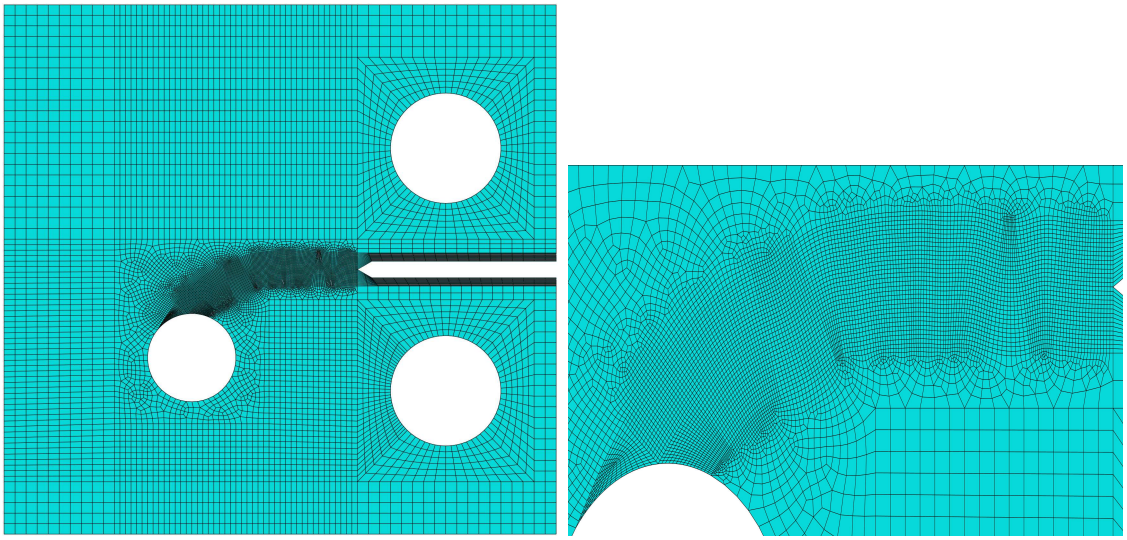

(a) Meshed model used to calculate K_I and K_{II}.

(b) Zoom of the meshed model on the crack neighborhood.

Table 8.2: Values of ΔK_I and ΔK_{II} and respective crack length value and number of cycles.

a /mm	ΔK_I MPa$\sqrt{\text{mm}}$	ΔK_{II} MPa$\sqrt{\text{mm}}$	Number of cycles
3.4	211.80	10.55	45000
4.4	234.22	13.58	95000
5.1	240.17	14.00	120000
7.4	247.75	5.53	145000
8.9	262.50	38.71	155000
10.6	279.19	2.60	165000
12.8	297.90	14.41	172500
13.6	306.64	3.82	177500
14.7	318.13	3.37	182500
16.4	342.43	2.16	186250
17.5	368.36	13.18	188750
18.6	385.59	4.33	191250
19.9	398.41	35.74	193750
21.4	410.03	126.32	196250
23.5	461.84	19.93	198750
25.2	505.42	18.41	201250
28.9	573.85	68.58	203000

Figure 8.16 shows the evolution of the crack length with the increase of the number of cycles. And as it would be to expect the higher are the number of cycles the bigger is the change on the crack size for a certain number of cycles.

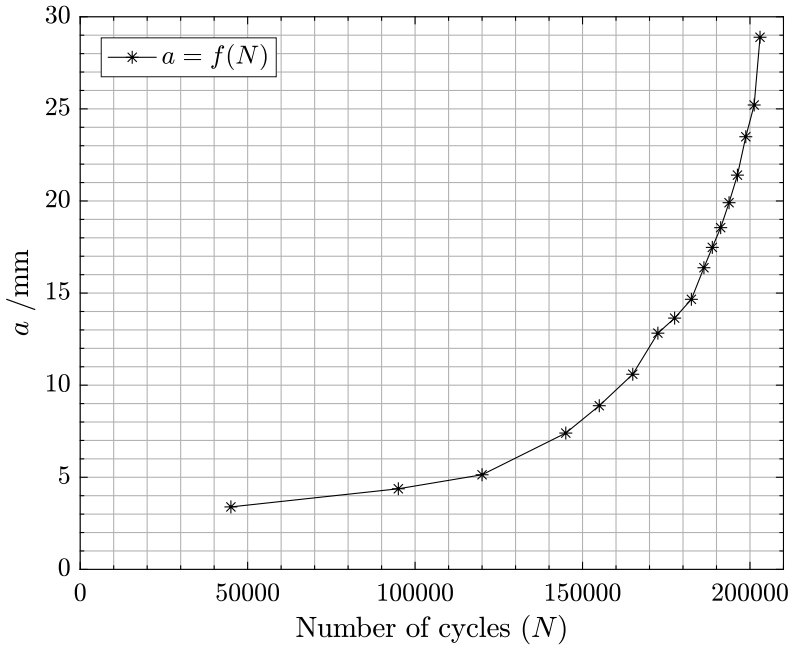

Figure 8.16: Evolution of the crack length with the increase of the number of cycles.

In order to visualize the behavior of ΔK_I and ΔK_{II} with the number of cycles, the

values of ΔK_I and ΔK_{II} were plotted as function of number of cycles. The resulting plot is shown in figure 8.18 and from its analysis it can be concluded that the values of K_I get bigger as the number of cycles increase and the values of K_{II} do not show a clear tendency. Also can be noticed that the values of ΔK_I are always much greater than the values of K_{II}.

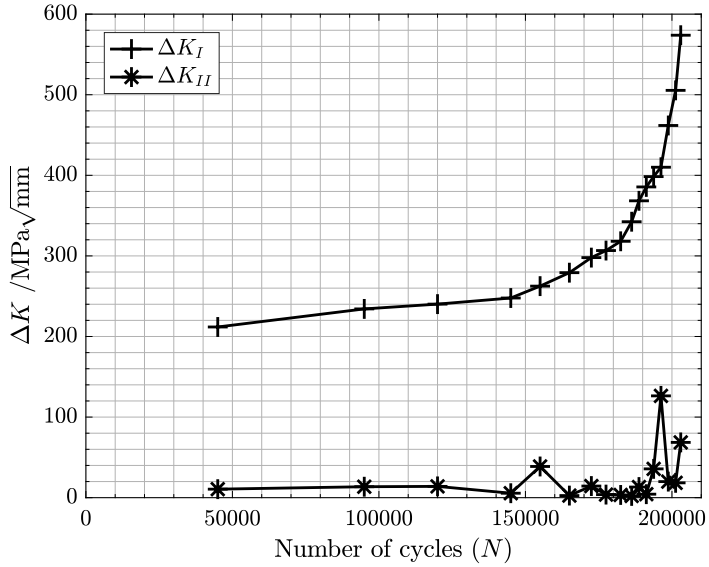

Figure 8.17: K_I and K_{II} as function of the number of cycles.

Figure shows the evolution of $\Delta K_e^{Richard}$ with the number of cycles. the evolution of $\Delta K_e^{Richard}$ is very similar to the evolution of ΔK_I in figure 8.18 as it is expected. Since $DeltaK_I$ is much grater than ΔK_{II}, the value of ΔK_e is similar to the value of ΔK_I, as shown in figure 1.8.

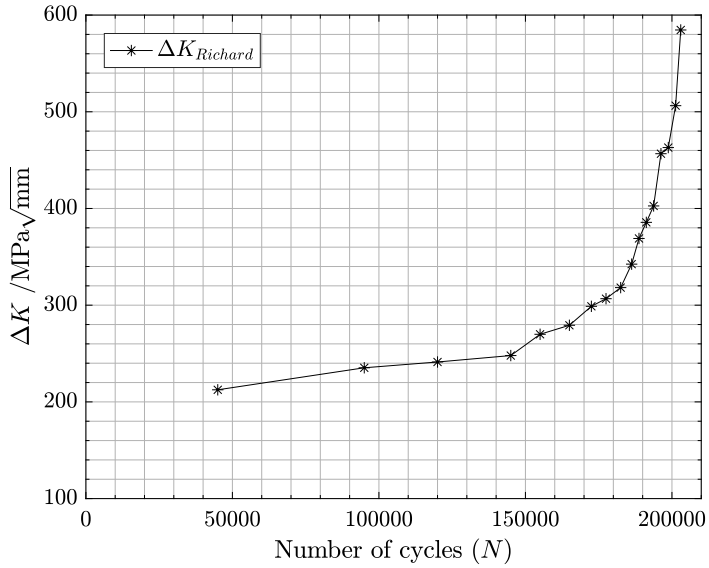

Figure 8.18: K_I and K_{II} as function of the number of cycles.

The equivalent stress intensity factor was calculated according to the approaches presented in section 1.3 and the results are presented in table 8.3. Plotting the data of table 8.3 in a double-logarithmic scale graphic are obtained the fatigue propagations curves for each approach.

Table 8.3: Values of the equivalent stress intensity factors according to the different approaches and values of the correspondent $^{da}/_{dN}$

$\frac{da}{dN}$ $/mm \cdot cycle^{-1}$	ΔK_e Richard /MPa$\sqrt{\text{mm}}$	ΔK_e Energy /MPa$\sqrt{\text{mm}}$	ΔK_e Tanaka /MPa$\sqrt{\text{mm}}$	ΔK_e Chen /MPa$\sqrt{\text{mm}}$
1.09E-05	212.5	212.1	211.8	212.5
7.61E-05	235.3	234.6	234.2	235.2
5.66E-05	241.3	240.6	240.2	241.2
0.000148	247.9	247.8	247.7	247.9
0.000171	269.9	265.3	262.5	269.5
0.000223	279.2	279.2	279.2	279.2
0.000163	298.8	298.3	297.9	298.8
0.000204	306.7	306.7	306.6	306.7
0.000343	318.2	318.2	318.1	318.2
0.000442	342.4	342.4	342.4	342.4
0.000429	369.0	368.6	368.4	368.9
0.000542	385.7	385.6	385.6	385.6
0.000599	402.6	400.0	398.4	402.4
0.000833	456.6	429.0	411.0	455.6
0.000689	463.0	462.3	461.8	462.9
0.001471	506.3	505.8	505.4	506.3
0.002266	584.6	577.9	573.9	584.0

Figure 8.19 shows the points of the values of da/dN as a function of ΔK_e for the used approaches as well as the respective fitting curve. The equations of each fitting curve are presented below:

$$\text{Paris law,} \quad \frac{da}{dN} = 85.409 \cdot 10^{-15} \Delta K^{3.7554} \tag{8.3}$$

$$\text{Richard,} \quad \frac{da}{dN} = 1 \cdot 10^{-14} \Delta K_e^{4.0929} \tag{8.4}$$

$$\text{Energy,} \quad \frac{da}{dN} = 1 \cdot 10^{-14} \Delta K_e^{4.1.1549} \tag{8.5}$$

$$\text{Tanaka,} \quad \frac{da}{dN} = 8 \cdot 10^{-15} \Delta K_e^{4.1858} \tag{8.6}$$

$$\text{Chen,} \quad \frac{da}{dN} = 1 \cdot 10^{-14} \Delta K_e^{4.096}. \tag{8.7}$$

Observing figure 8.19 it can be noticed that all the approaches are very similar to the original Paris law extracted from NASGRO material database. This is an expected results because the values of K_{II} are lower when compared with the values of K_I and for that reason the values of K_e will be near to the values of K_I, has was demonstrated in figure 1.8

where the value of the non-dimensional equivalent stress intensity factor (K_e/K_I) tends to one as the ratio K_I/K_{II} tends to infinite.

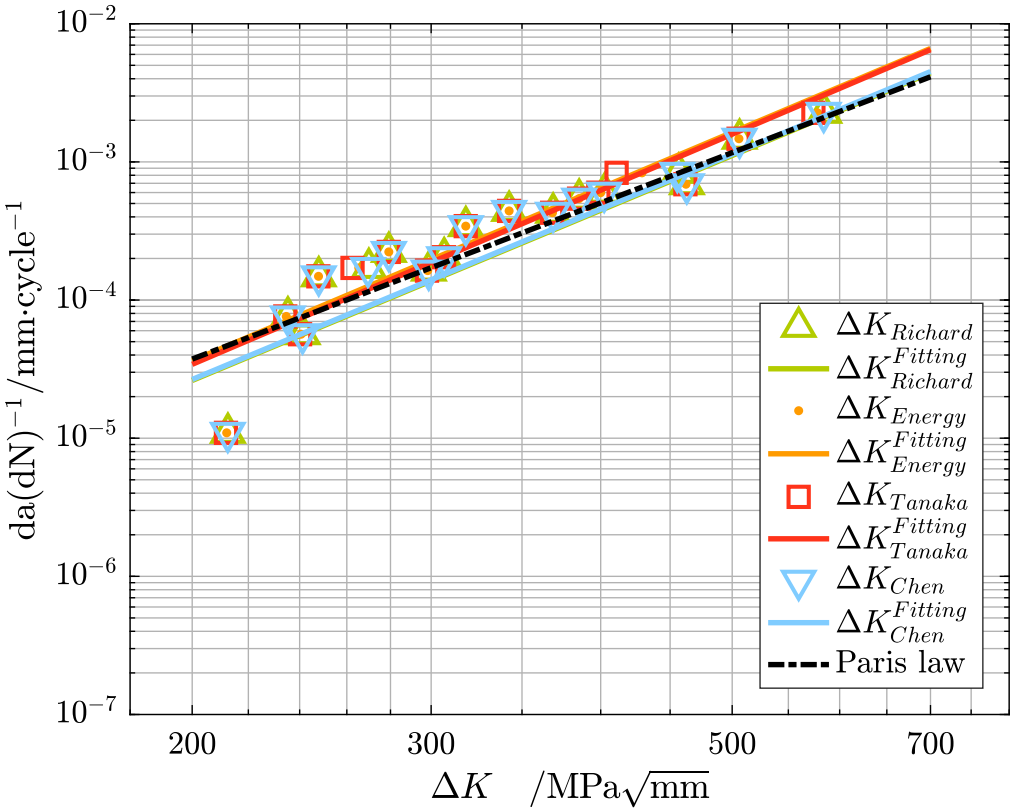

Figure 8.19: Comparison between the Paris law based on the NASGRO database material and the fitting curves of the points obtained for each approach.

From figure 8.19 also can be concluded that for the case that as been analysed the fact of the crack is propagating in plane mixed-mode does not have a great influence on the crack growth ratio.

8.2 Three point bend specimen

The experimental setup, numerical models and the respective results for the three point bend specimen will now be presented. In this case the mode II was induced by loading the specimen out of the symmetry plane and adding holes to the specimens. In order to better understand the influence of the distance between supports and load position on the values of K_I and K_{II} will be performed studied some cases. For each case will determined, using Abaqus software and the J-integral technique, the values of K_I, K_{II} and the value of the propagation angle.

8.2.1 Solid mechanics analysis

Taking into consideration that (i) the relationshipp of the distance between the crack plane and the plane of the applied load, with the distance between supports, is always the same, one quarter and (ii) the crack is always in the middle, of the supports it is possible to

generalize the equation for the bending moment for the cases where the load is applied out of the crack plane. According to the values of the shear diagrams the value of the left reaction will be equal to:

$$R_1^y = \frac{1}{4} \cdot P_{applied} \quad /\text{kN} \tag{8.8}$$

as the specimen is loaded with a concentrated load the shear force will be constant until the load application point, therefore for the shear for takes the following value:

$$V(x) = R_1^y = \frac{1}{4} \cdot P_{applied} \quad /\text{kN} \tag{8.9}$$

where x is the local coordinate and is equal to zero on the support. As a results of the above value for the shear force, the bending moment equation takes the following shape:

$$M_b(x) = \frac{1}{4} \cdot P_{applied} \cdot x \quad /\text{kN} \cdot \text{m} \tag{8.10}$$

For the case where the load is applied on the crack plane, which is coincident to the symmetry plane, the shear force between the left support and the crack will be equal to:

$$V(x) = \frac{1}{2} \cdot P_{applied} \quad /\text{kN} \tag{8.11}$$

therefore the equation of the bending moment will be given by:

$$M_b(x) = \frac{1}{2} \cdot P_{applied} \cdot x \quad /\text{kN} \cdot \text{m} \tag{8.12}$$

With the bending moment equation defined for every studied case, it is possible to determine the value of the bending moment on the crack location for each case. So making use of equations 8.17 and 8.12 the values of the bending moment for each case are:

Load applied on the crack plane (symmetry plane), case 1

Since the load is applied on the symmetry plane,implies that $x = S/2$, therefore,

$$M_b^{crack} = \frac{1}{4} \cdot P_{applied} \cdot S \quad /\text{kN} \cdot \text{m} \tag{8.13}$$

where W is the distance between supports, for the studied situation $S = 230 \cdot 10^{-3}$ m so the bending moment as a function of $P_{applied}$ takes the following value:

$$M_b^{crack} = \frac{1}{4} \cdot P_{applied} \cdot 230 \cdot 10^{-3} \quad /\text{kN} \cdot \text{m} \tag{8.14}$$

Load applied out of the crack plane, case 2

For the cases where the load is applied out the crack plane the distance between the crack plane and the plane of the applied force is equal to $S/4$, since the crack is always in the symmetry plane of the supports means that the distance between the supports and the crack is $S/2$, therefore the distance between the plane of the applied load and the left support, reference point, is $3/4 \cdot S$ which is the value of x for those cases.

Therefore the bending moment equation takes the following shape:

$$M_b(x)^{crack} = \frac{3}{16} \cdot P_{applied} \cdot S \quad /\text{kN} \cdot \text{m} \tag{8.15}$$

For case 1 the value of the S is $230 \cdot 10^{-3}$ m, so the value of the bending as a function of the applied load is:

$$M_b(x)^{crack} = \frac{3}{16} \cdot P_{applied} \cdot 230 \cdot 10^{-3} \quad /\text{kN} \cdot \text{m} \tag{8.16}$$

The corresponding diagrams for this case are shown in figure 8.21.

Load applied out of the crack plane, case 3

Case 2 is very similar to the case 1, the only difference is the value of the distance between supports. In this case the value of S is $120 \cdot 10^{-3}$, as a result the value of the bending moment as a function of $P_{applied}$ is:

$$M_b(x)^{crack} = \frac{3}{16} \cdot P_{applied} \cdot 120 \cdot 10^{-3} \quad /\text{kN} \cdot \text{m} \tag{8.17}$$

The diagrams of shear force and bending moment corresponding to this case are shown in figure 8.22.

Figure 8.20 shows the shear force and bending moment diagrams for the case where the specimen is loaded on the symmetry plane with a unitary load. It can be noticed that for this case there is no shear force on the crack plane, therefore the nominal stress actuating at the crack tip is only due ti the bending moment. for this loading situation for a specimen without holes the value of K_{II} should be nearly to zero.

Figure 8.21 shows the shear force and bending moment diagrams for case 2. For this situation the crack tip is subjected to a bending moment and to a shear force, this shear force will originate the mode II to loading, therefore the value of K_{II} will be different of zero and the crack will propagate in with a determined inclination which function of K_I and K_{II}. Figure 8.22 shows the shear force and bending moment diagrams for case 3. For this case it also exists mode II and the propagation angle will be different of the propagation angle for case 3.

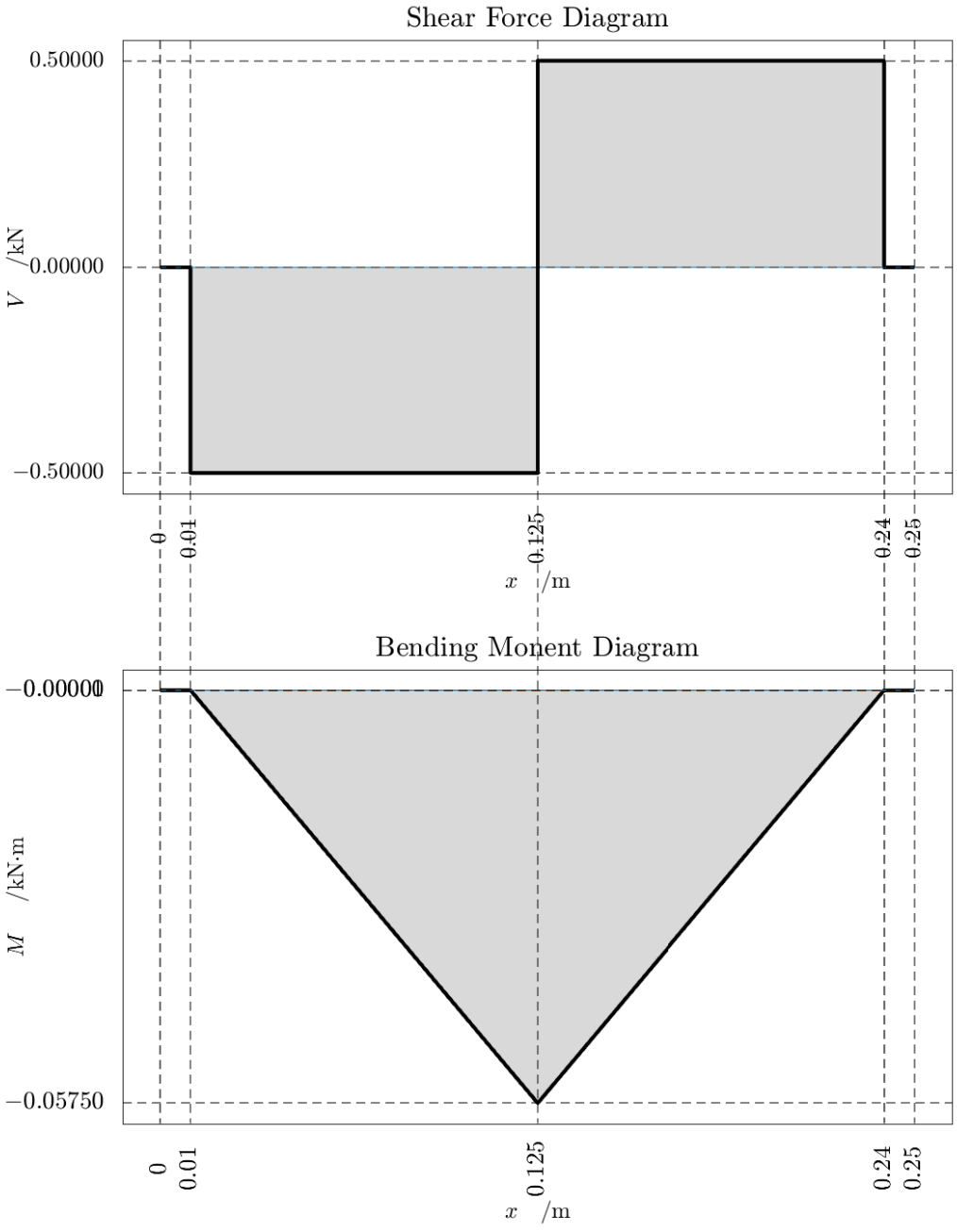

Figure 8.20: Shear force and bending moment diagrams for a symmetric load.

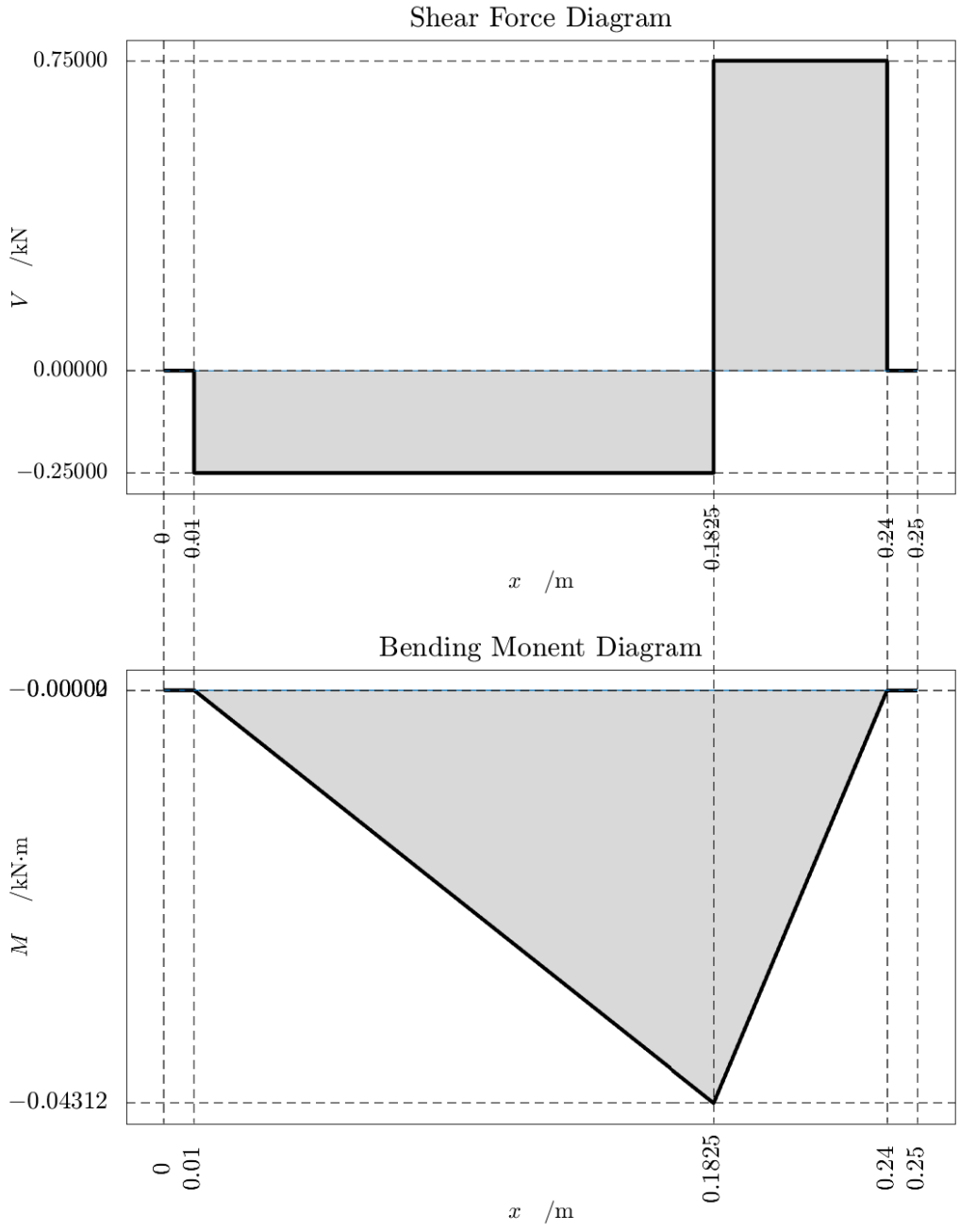

Figure 8.21: Shear force and bending moment diagrams for an asymmetric load.

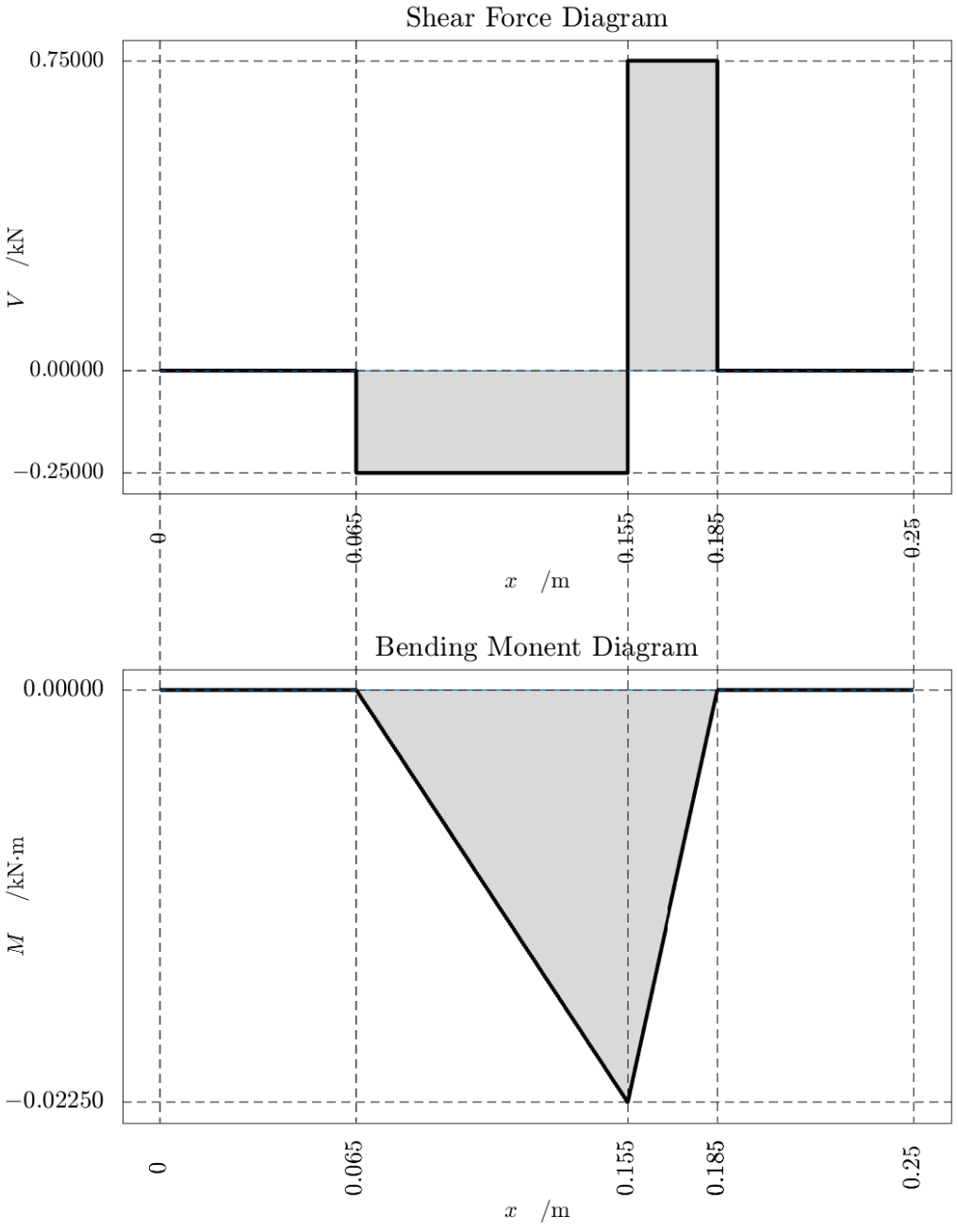

Figure 8.22: Shear force and bending moment diagrams for a distance between supports of 120 mm, with asymmetrical loading.

8.2.2 Determination of K_I, K_{II} and propagation angle

In the previous section the internal efforts diagrams for the different loading situations has been shown. Now for a better understanding of the influence of those values, the values of K_I, K_{II} and propagation angle θ will be determined for each case. To determine those values were used the same crack length, load value and specimen geometry and dimensions. The dimensions of the specimen can be observed in figure 7.2, in the studied cases the crack as total length of 15 mm and the applied load has as value 15 kN. To predict the crack propagation angle for each situation the maximum tangential stress (MTS) was used. The obtained results for each case are shown in the table below.

Table 8.4: Results of K_I, K_{II} and θ for each studied situation.

	K_1 /MPa$\sqrt{\text{mm}}$	K_{II} /MPa$\sqrt{\text{mm}}$	θ Degrees
Case 1	372.3	-0.17	0
Case 2	269	16.2	-6.9
Case 3	112.9	13.1	-12.9

The resulting crack paths for each loading case are shown in figures 8.23a to 8.23c.

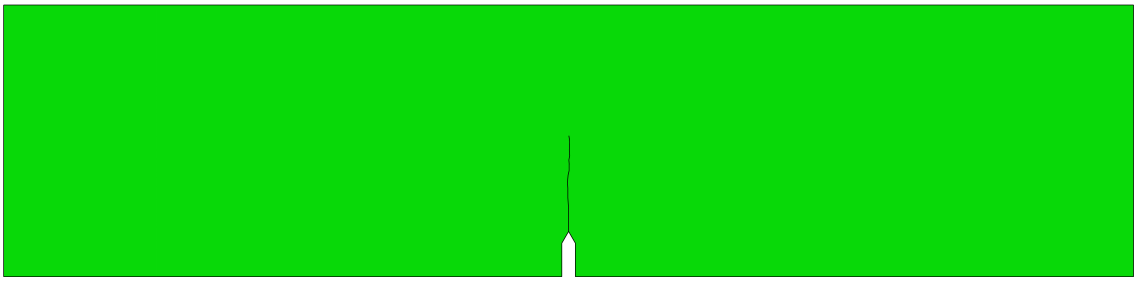

(a) Crack-path for case 1.

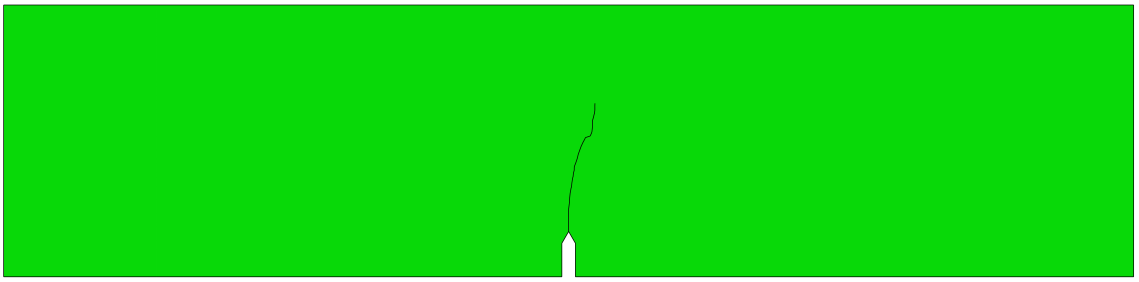

(b) Crack-path for case 2.

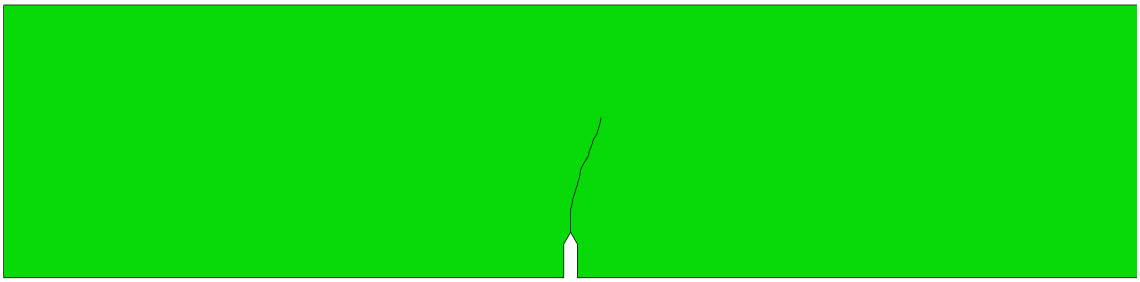

(c) Crack-path for case 2.

Figure 8.23: Crack-path results for each loading situation presented above.

As it is shown in figure 8.23 the results of the crack propagation show a good agreement with the values of the propagation angle presented in table 8.4, for case 1 $\theta_1 = 0$ and for cases 2 and 3 can be observed that $\theta_3 > \theta_2$, where θ_1, θ_2 and θ_3 are the propagation angles for cases 1, 2 and 3 respectively.

The first thing to do is determine the maximum load which can be used during the fatigue test in order to have an approximate crack growth rate. The procedure to determine this load will be similar to the one used in the previous section for the CT specimen.

8.2.3 Determination of the maximum fatigue load during the crack propagation

Tests were preformed in the two configurations mentioned in this thesis, for the 3PB specimen, therefore it is needed to determine two values of the maximum fatigue load during the crack propagation. The two different geometries are shown in figures 6.5 and 7.2 where the difference between them is the specimen width.

Since the specimens are subjected to mixed mode loading, one way to determine the maximum fatigue load is: making use of the Paris law for the used material extract the value of the stress intensity factor for the chosen crack-growth rate, da/dN, value. Subsequently and using the ASTM E399 standard equation for the stress intensity factor calibration curve it is possible determine an approximation of the maximum value for the fatigue test load.
It is important to be noticed that the ASTM E399 standard equation is for pure mode I, therefore applying it to the studied cases is an approximation.

Three point bend specimen with a width of 40 mm

The first used geometry was the specimen shown in figure 6.5 where width (W) is 40 mm, the length of the fatigue pre-crack for this specimen is 6 mm which leads to an initial crack length of 16mm, the distance between supports for this case is 120 mm. For crack growth to be a slow process to make easier the data acquisition, a value of da/dN near to 1 mm per 10000 cycles will be chosen, which the same of the one chosen to the CT specimen, and for this value of crack-growth ratio the value of ΔK is 260 MPa$\cdot\sqrt{\text{mm}}$. Bearing in mind the ASTM E399 standard equation, previously mentioned in equation 7.8 it is now possible to estimate the maximum value for the fatigue propagation load test, P_{max}. As $W = 40$ mm and $a = 16$ mm the value of the non-dimensional stress intensity factor is:

$$\frac{a}{W} = 1.9818 \tag{8.18}$$

Using equation 7.8 is possible to calculate value of P_{max} which is:

$$P_{max} = 61400 \qquad \text{N} \tag{8.19}$$

The calculated load is for mode I; as the specimen is loaded in a mixed mode situation the applied load can be bigger or smaller than the one determined in equation 8.19, this is just a reference value.

Three point bend specimen with a width of 60 mm

For this case the fatigue pre-crack as length approximately of 3 mm which means that the initial crack length is 13 mm, the width of specimen is 60 mm and the distance between supports is 230 mm. Similarly to what has been done to the anterior configuration, it

also will be chosen a determined crack-growth rate and using the Paris law fitting, based on the NASGRO material database, will be determined the corresponding value of ΔK. Considering that a mode I situation the value of P_{max} can be calculated using equation 7.8.

The crack-growth rate will the same as the one used in the precious case so the value of ΔK will be the same, because the used material is the same for both specimens configurations. Before calculate the value of P_{max} it is needed to determine the value of the non-dimensional stress intensity factor, using equation 7.9 and for $a = 13$ mm and $W = 60$ mm results:

$$\frac{a}{W} = 1.2283 \tag{8.20}$$

therefore using equation 7.8 the value of P_{max} is:

$$P_{max} = 9500 \qquad \text{N} \tag{8.21}$$

8.2.4 Experimental setup

The experimental setup is the same for both specimen configurations and can be observed in figure 8.24.

The load is applied by the top support. The bottom support only restricts the displacement on the vertical direction and can be adjusted to any distance between supports since it belongs to the maximum range allowed by the support.

Figure 8.24: Experimental setup for 3PB specimens.

8.2.5 Experimental crack path

Now the experimental crack path results will be presented for the three point bend specimens. For the 60 mm width specimen, two different configuration which are shown in figure 8.25, were studied. The holes where added in order to increase the mode II component.

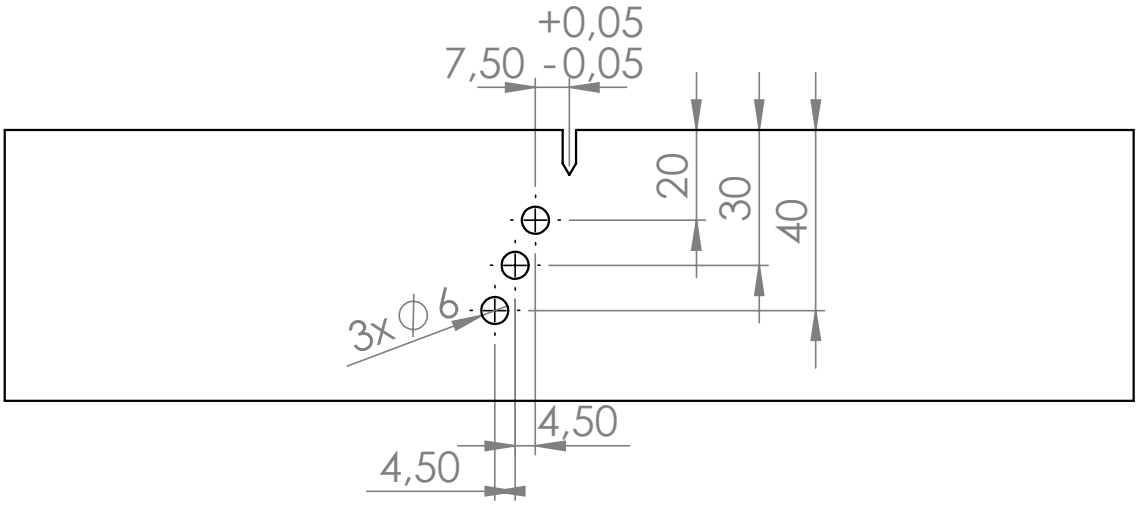

(a) Three point bend specimen with three holes with 6 mm diameter.

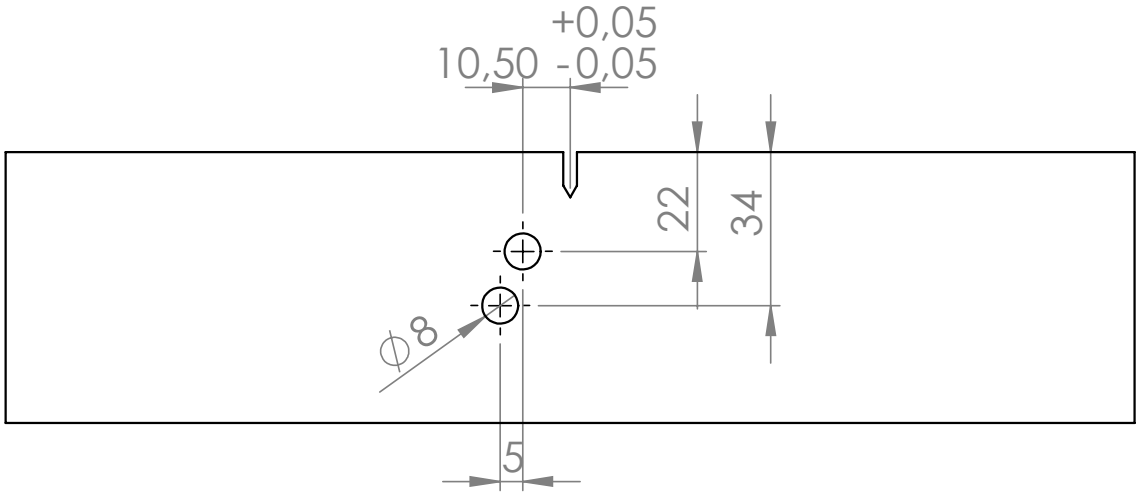

(b) Three point bend specimen with two holes with 8 mm diameter.

Figure 8.25: Three point bend specimen with 60 mm width configuration.

Experimental crack path for the 40 mm width 3PB specimen.

For this specimen the remaining section was too small and could not support the applied load, therefore the specimen broke. This brittle fracture corresponds to the part of the crack path where is visible the effects of plasticity at the specimens surface. In figure 8.26a is shown the crack path result for the experimental test. Figure 8.26b shows the crack surface for the same specimen, it can be observed the appearance of "shear lips" where the brittle fracture occurred which indicates that the crack propagates in plane stress situation.

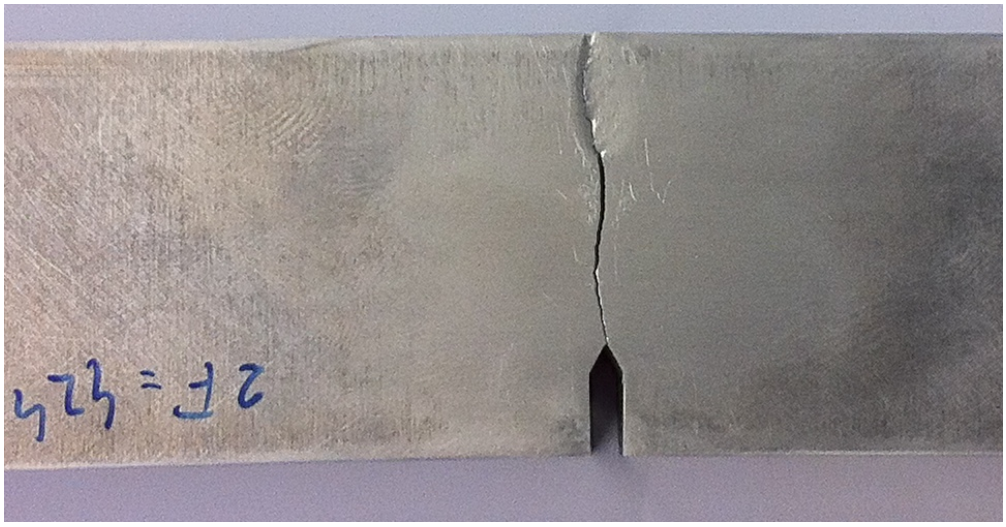

(a) Experimental crack path for the 40 mm width 3PB specimen.

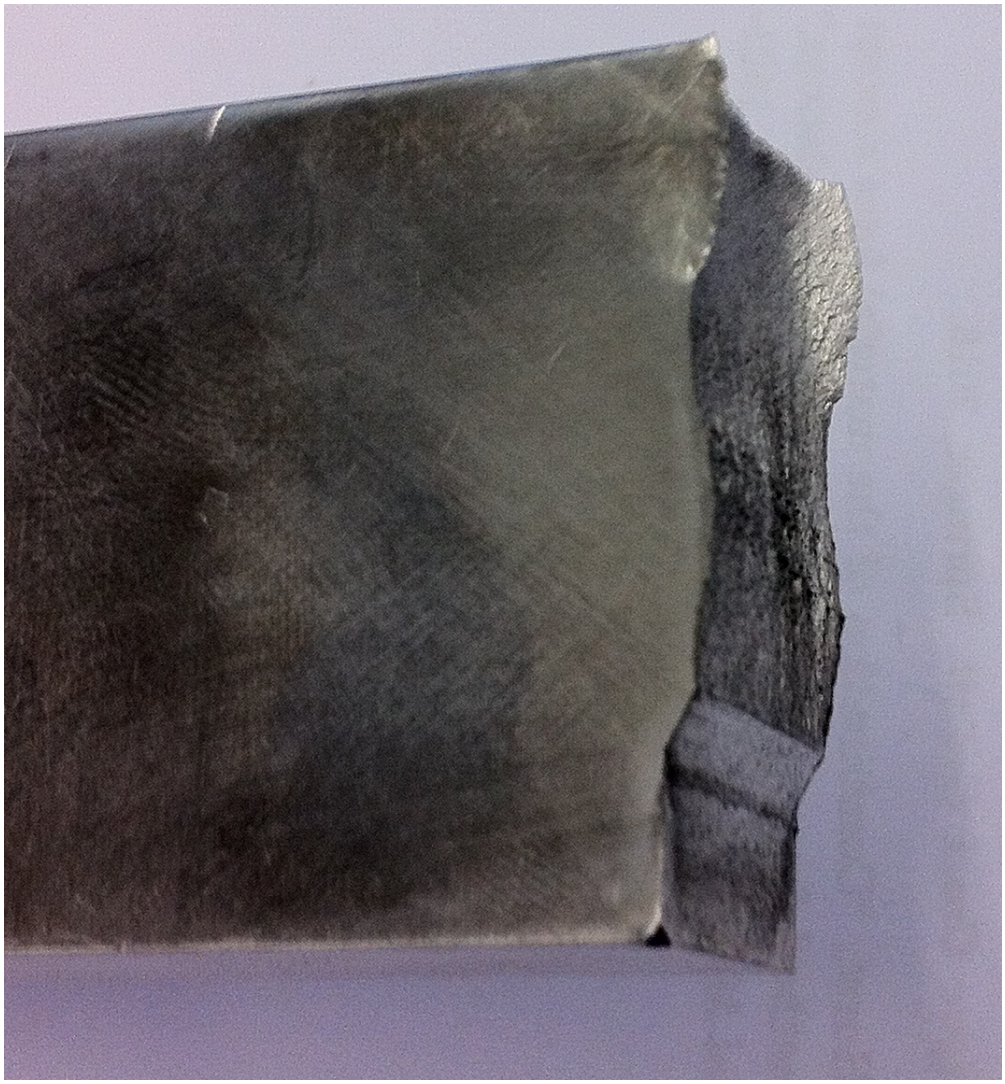

(b) Crack surface for the 3PB specimen with 40 mm width.

Figure 8.26: Three point bend specimen with 40 mm width experimental crack path.

Experimental crack path for the 60 mm width 3PB specimen: 3 holes configuration

The crack path results for the this configuration of the specimen will now be presented. As shown in figure 8.27 the crack path goes through the first hole, in this case the specimen did not break since the remaining section of the specimen were considerable.

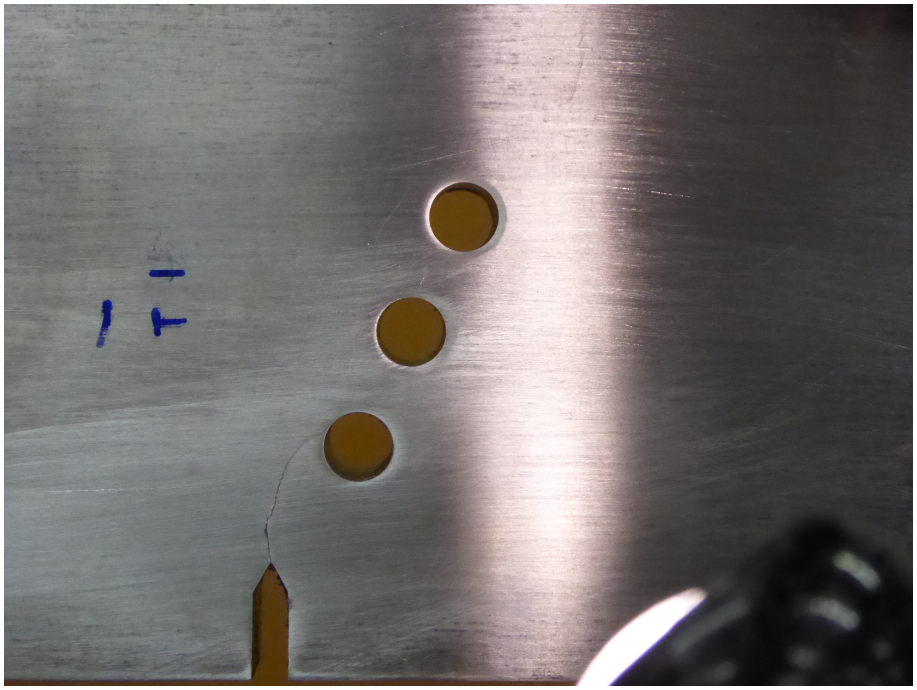

Figure 8.27: Three point bend specimen with 60 mm width and 3 additional holes crack path.

The obtained crack path was not the expected one since it was thought that the crack would propagate and did not intersect any of the three holes.

Experimental crack path for the 60 mm width 3PB specimen: 2 holes configuration

For this configuration the obtained crack path for the experimental tests is shown in figure 8.28. The crack also propagates in the direction of the first hole which - as in the previous case - was not expected.

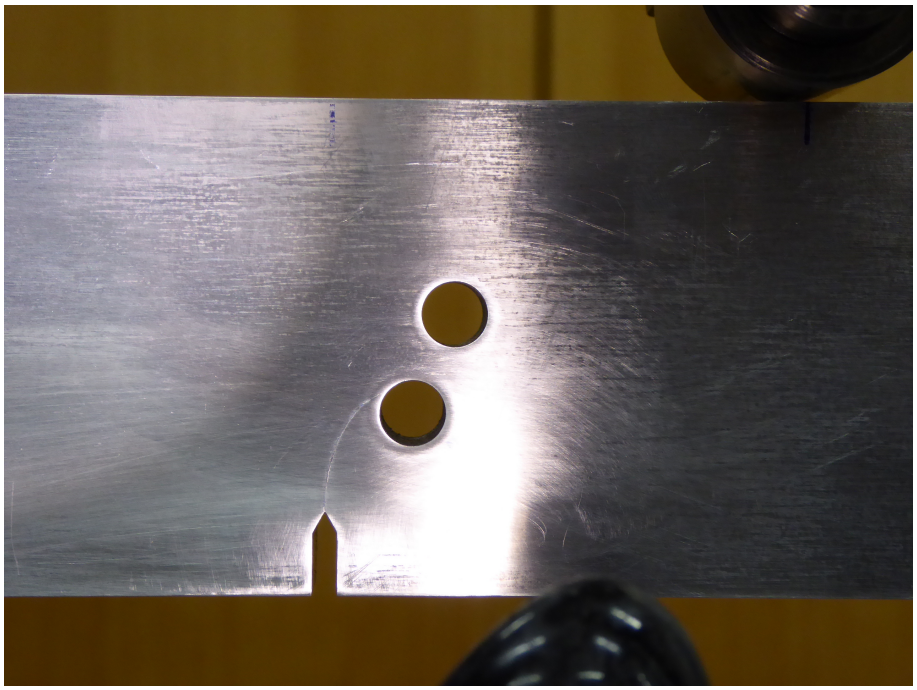

Figure 8.28: Three point bend specimen with 60 mm width and 3 additional holes crack path.

The experimental models where designed based on preliminary numerical results which after the obtained experimental results were corrected.

8.2.6 Numerical models and results

Now the numerical models and results for the three point bend specimens will be presented. Since the numerical results for the CT specimen which has shown better agreement with the experimental results were the ones with a free mesh on the crack domain, for the 3PB specimens only models which are meshed with a free mesh on the crack domain will be studied.

Three dimensional numerical model and results for the 3PB specimen with 40 mm width.

For the 3PB specimen with a 40 mm width the distance between supports is 120 mm and the distance between the crack plane and the load plane is 30 mm. The used mesh for the three dimensional numerical model can be observed in figure 8.29. The used mesh is substantially refined on the crack domain in order to obtain accurate results.

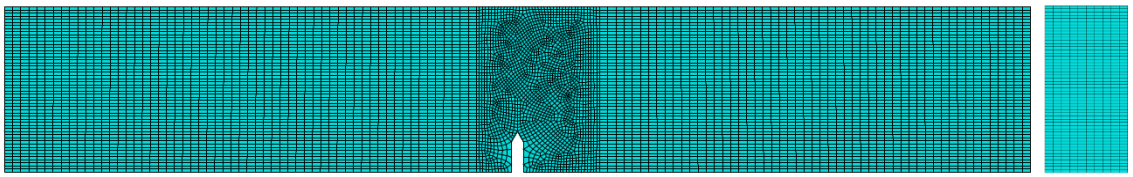

Figure 8.29: Three dimensional numerical model mesh for the 3PB specimen with 40 mm width.

The results obtained for the crack path for the model shown above are presented in figure 8.30.

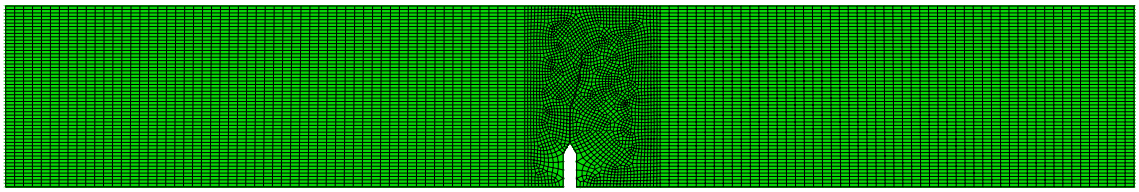

Figure 8.30: Three dimensional numerical model for the 3PB specimen with 40 mm width, crack path results.

Two dimensional numerical model and results for the 3PB specimen with 40 mm width.

Since the numerical results for the three dimensional models has been already presented, now the two dimensional numerical model and the respective results will be presented. Figure 8.29 shows the meshed model used for the two dimensional model.

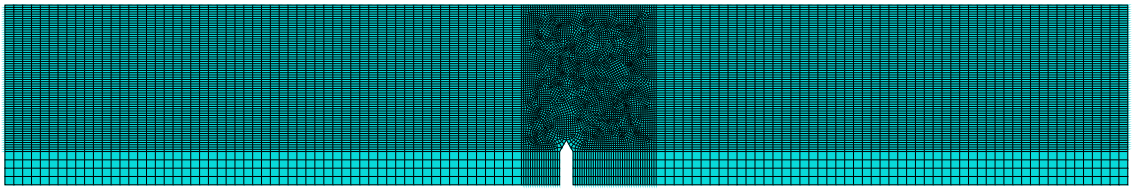

Figure 8.31: Two dimensional numerical model mesh for the three point bend specimen with 40 mm width.

It is to be expected that the obtained results for the three numerical models has to be very similar to the results obtained with 2D models; this agreement has already been shown for the CT specimen numerical models. Figure 8.32 shows the crack path obtained for this numerical model, which as expected very similar to the crack path observed in figure 8.32 for the three dimensional model.

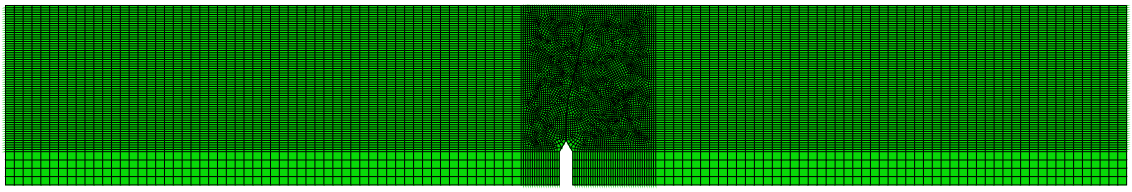

Figure 8.32: Two dimensional numerical model for the 3PB specimen with 40 mm width, crack path results.

Similarly to the comparison made for the CT specimens between the numerical and the experimental results for the crack path, this comparison will not be made for the 3PB specimen with 40 mm width. Since the pre-crack has a considerable inclination and length (around 6 mm), the remaining ligament has a small dimension. This fact has two consequences: i) the mechanical resistance of specimen is comprised, so brittle fracture will occur; ii) the distance traveled by the crack will not be big enough such that the initial inclination of the pre-crack can be negligible. So bearing in mind of the

related consequences the comparison between experimental and numerical results will not be relevant.

Three dimensional numerical model and results for the 3PB specimen with 60 mm width with 3 additional holes.

The 3PB specimen configuration used for the following numerical model is the one presented in figure 8.25a. The meshed model is shown in figure 8.33.

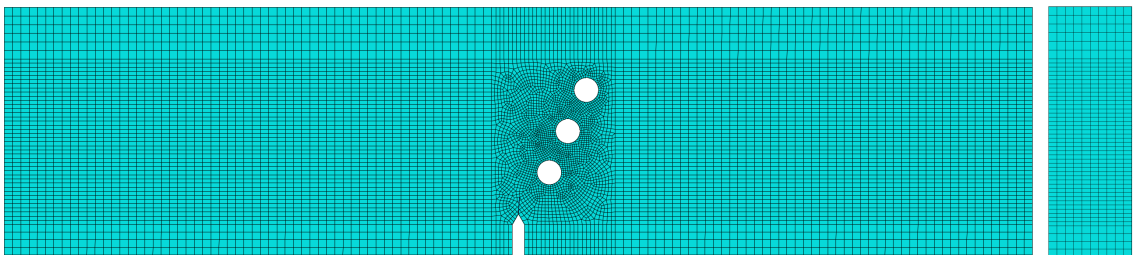

Figure 8.33: Three dimensional meshed model for the 3PB specimen with 60 mm width and 3 additional holes.

The crack propagation path resulting of the numerical three dimensional numerical mode is shown in figure 8.34.

As can be observed in the previous figure, the crack propagation path obtained for the three dimensional model does not intersects the first hole. So the comparison between the experimental and numerical crack path only will be performed for the crack until the experimental path intersects the first hole. The remaining numerical path will be considered insignificant.

Two dimensional numerical model and results for the 3PB specimen with 60 mm width with 3 additional holes.

Now, similarly to what has been done for the other models a two dimensional model and respective results will be presented.

Figure 8.35 shows the meshed model for the 3PB specimen with 60 mm width and 3 additional holes.

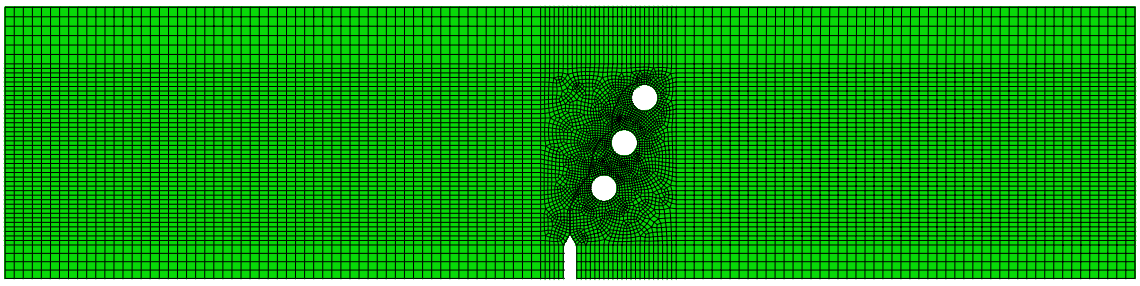

Figure 8.34: Three dimensional model for the 3PB specimen with 60 mm width and 3 additional holes, crack path results.

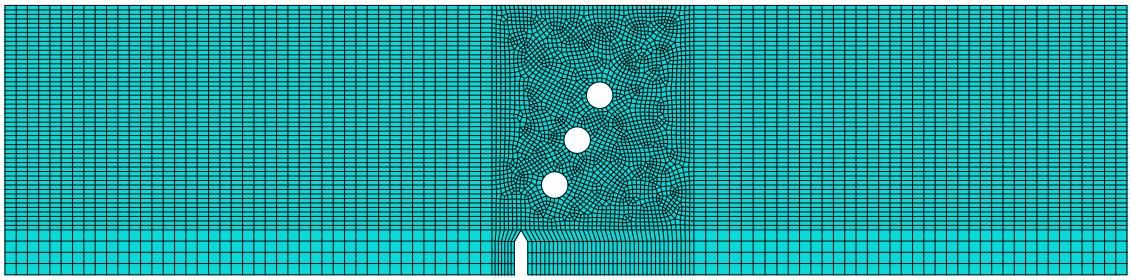

Figure 8.35: Two dimensional meshed model for the 3PB specimen with 60 mm width and 3 additional holes.

The respective results for the crack propagation path are shown in the following figure.

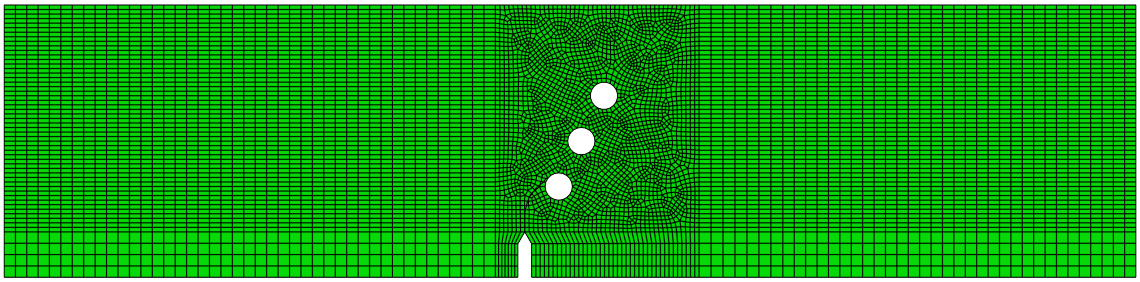

Figure 8.36: Two dimensional model for the 3PB specimen with 60 mm width and 3 additional holes.

Comparison results for the 3PB specimen with 60 mm width and 3 additional holes.

The numerical and experimental crack propagation paths will now be compared. In figure 8.37 are compared the results for the crack propagation path resulting from: the experimental tests and from the two and three dimensional numerical models. The black circumference is a schematic representation of the first additional hole.

As already said, only a part of the crack path for the three dimensional numerical model only has been considered. From the analysis of figure 8.37 can be noticed that the 2D model results show better agreement than the results of the 3D model when compared with the experimental crack path.

The differences between the numerical and experimental crack paths can be justified by the fact that the numerical result is very sensitive to the initial pre-crack length and inclination, those two parameters are hard to measure accurately and have a great influence on the numeric result. Also the material is considered to be isotropic and perfect with no internal flaws or inclusions and this may be not representative of real material which can contain inclusion or internal flaws.

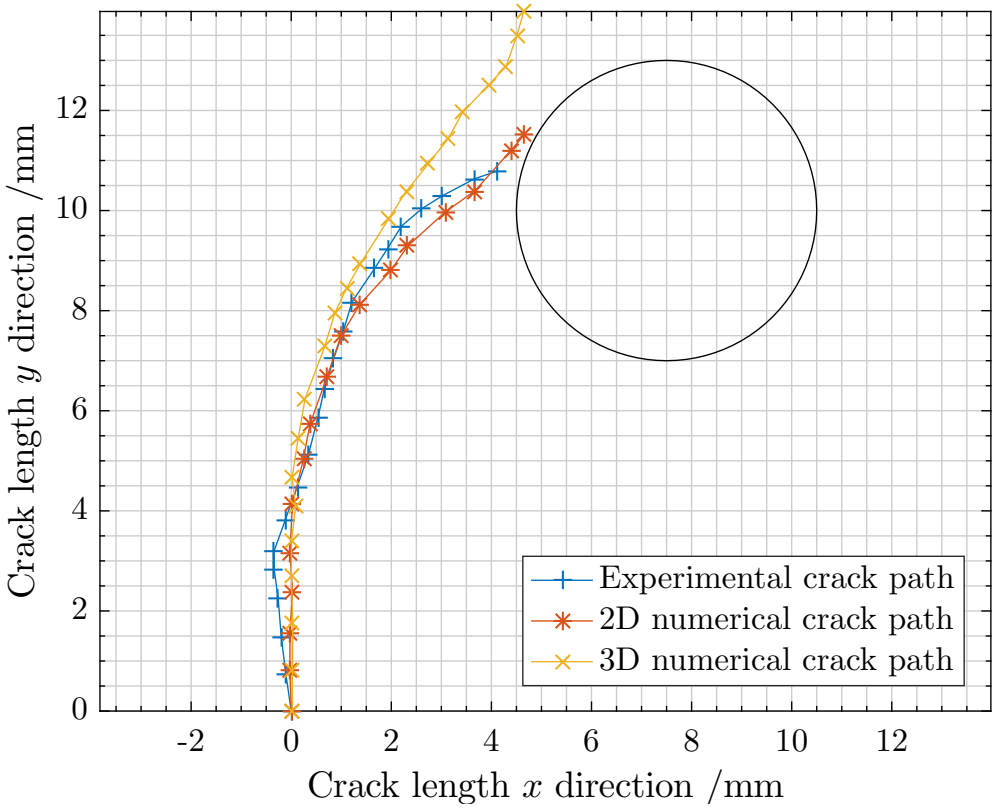

Figure 8.37: Comparison between the experimental and numerical crack paths.

The experimental and numerical results for the configuration of the 3PB specimen presented in figure 8.25a were presented and discussed above. Now the configuration for the 3PB specimen shown in figure 8.25b will be analysed below.

Three dimensional numerical model and results for the 3PB specimen with 60 mm width with 2 additional holes.

The 3D meshed model for the current configuration is shown above. Again a free mesh has used on the crack propagation domain.

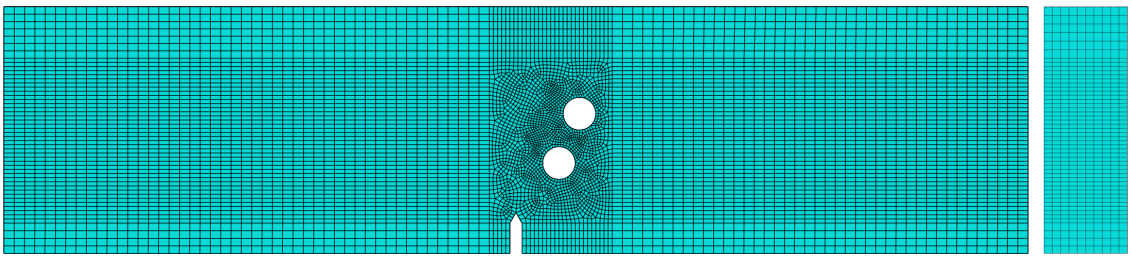

Figure 8.38: Three dimensional numerical model for the crack path for the 3PB specimen with 60 mm width and 2 additional holes.

Figure 8.39 shows the crack propagation path for the model shown in figure 8.38. Again the crack propagation path which is above the first hole influence field does not have interest since the experimental crack path intersects the first hole, since figure 8.39 only shows the crack path until the first hole.

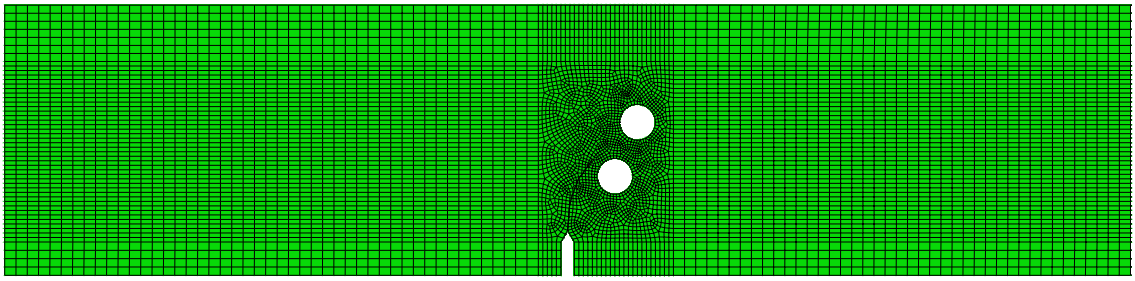

Figure 8.39: Three dimensional numerical model results for the crack path for the 3PB specimen with 60 mm width and 2 additional holes.

Two dimensional numerical model and results for the 3PB specimen with 60 mm width with 2 additional holes.

Now the two dimensional numerical model and respective results will be presented for the configuration being analysed. Figure 8.40 shows the used meshed model for the two dimensional analyses.

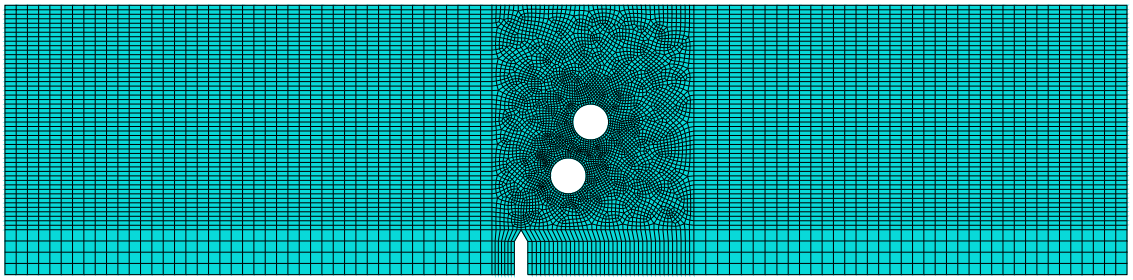

Figure 8.40: Two dimensional numerical model for the crack path for the 3PB specimen with 60 mm width and 2 additional holes.

The corresponding results are shown on the following figure.

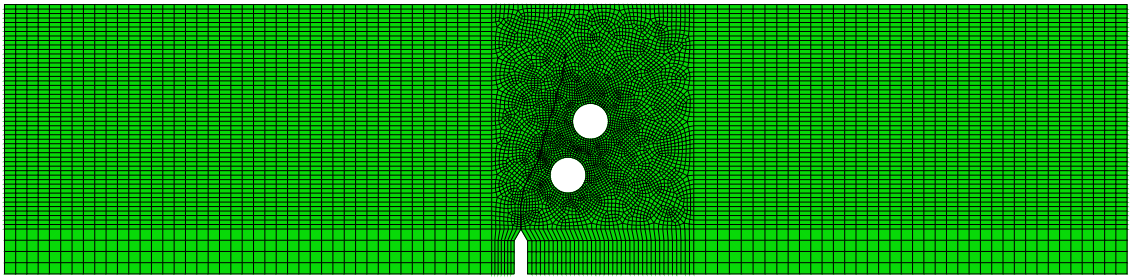

Figure 8.41: Two dimensional numerical model results for the crack path for the 3PB specimen with 60 mm width and 2 additional holes.

Comparison results for the 3PB specimen with 60 mm width and 3 additional holes.

The comparison between the different models and experimental tests will now be performed. Figure 8.42 shows the crack path propagation for the two and three dimensions numerical models and the experimental crack path result. Analysing the figure it can be

noticed that in this case non of the numerical models show a complete agreement with the experimental result. Both show a satisfying agreement at the beginning of the propagation but both models show a lower sensitivity to the added hole than the experimental model.

Again the causes for this difference might be traced to non isotropy of the used material, internal flaws or inclusions and other causes which has been already referred above.

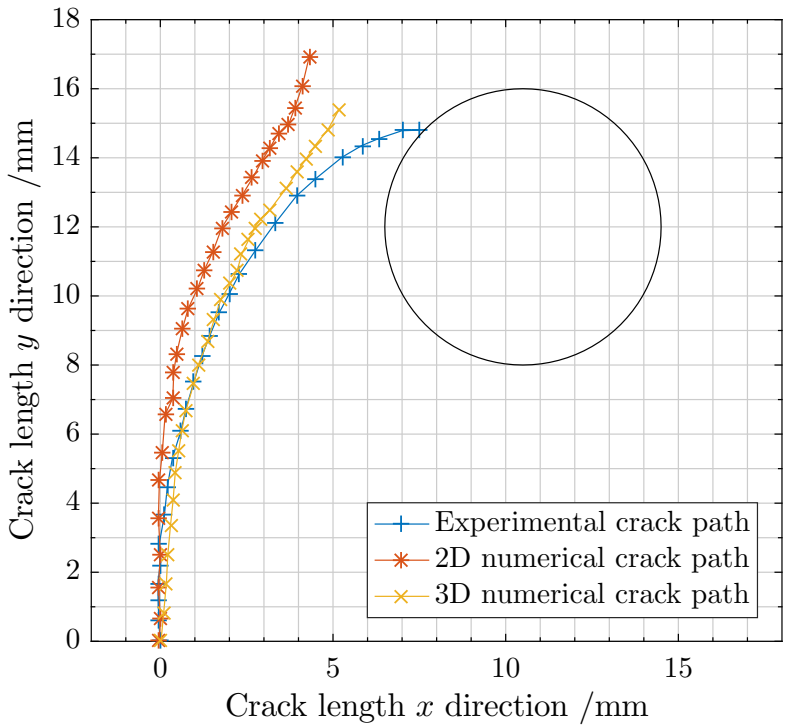

Figure 8.42: Comparison results for the 3PB specimen with 60 mm width and 2 additional holes

Chapter 9

Crack path for brittle fracture situations

In the previous chapter the crack path propagation for fatigue propagation situations has been studied. In this chapter the experimental results of tests preformed in cracked 3PB specimens monotonically loaded up to rupture will be shown, in an attempt to observe if the crack path will be influenced by the propagation velocity.

Therefore the experimental tests consist of loading the specimen, which already contain a fatigue pre-crack, until it reaches its fracture toughness and the propagation is unstable.

The tests were preformed in two different configurations of the specimen. Both have the same length which is 250 mm, and thickness which is 20 mm; the distance between supports also was the same for both (230 mm) and the distance between the crack plane and the load plane is either the same for both configuration which is 57.5 mm. The two configuration only differ on the width which is 40 and 60 mm.

The results are shown in figure 9.1, concentrating in crack surfaces which result form the experimental tests. For both specimens the results for crack path prediction are very complex to obtain due to the appearance of shear lips. Therefore the results will not be treated in the present work.

The shear lips phenomenon is much more expressive in the case of the 60 mm width specimen than in the case of the 40 mm width. A very coarse analysis of the crack path would be to measure the initial slope of the interior crack region, less disturbed by the shear lips phenomenon.

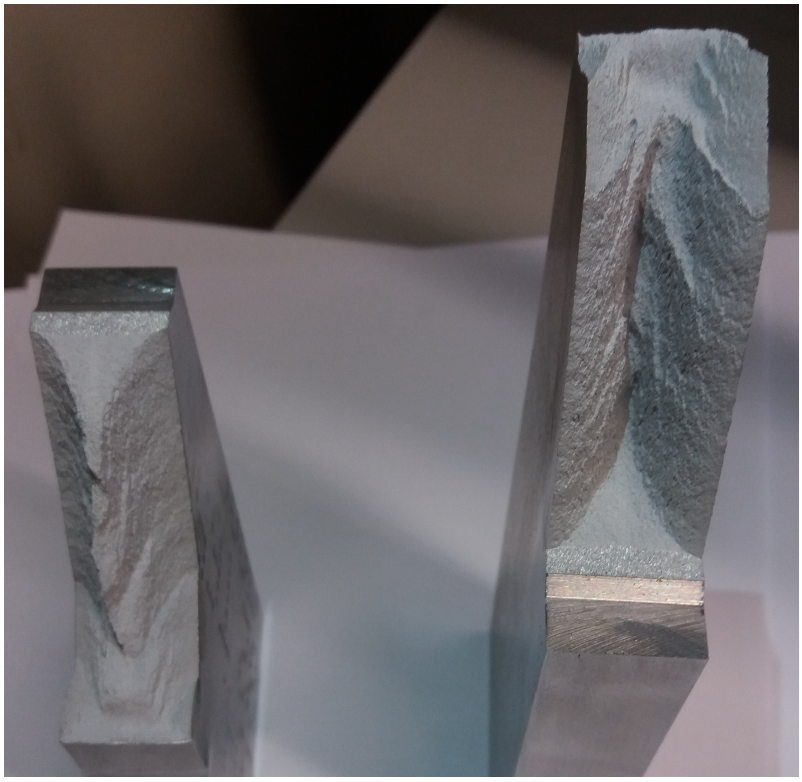

(a) Experimental results for brittle fracture tests for the 60 mm width 3PB specimen.

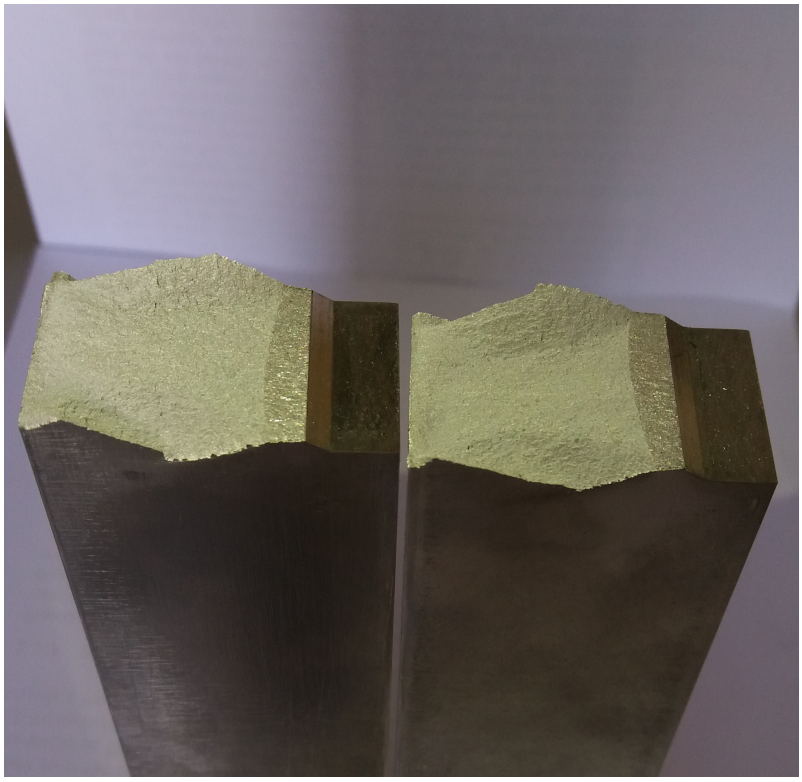

(b) Experimental results for brittle fracture tests for the 40 mm width 3PB specimen.

Figure 9.1: Experimental results for brittle fracture tests.

Chapter 10

Conclusion

10.1 Conclusions

The main conclusion of this work is that the extended finite element method is capable of predicting the crack path under mixed mode loading situations in an acceptable way.

The results extracted from the numerical methods show a better agreement with the obtained experimental results, for the compact tension specimens than for the three point bend specimens. It was found that the NNRPIM application to the present problem needs some refinement in order to give more accurate solutions.

Concerning the results obtained for the three point bend specimens, they do not mean that the numerical model results are wrong, it simply can mean that the input data of the numerical model were not the most correct. As example of these imprecise data are the assumption that the material is perfect and do not contain any internal defects or flaws; that the mechanical and fracture properties are equal in any direction;

All of those variables lead to conclude that the experimental results have a big dispersion so it may occur that using the same setup, material and geometry the results can be different. Therefore validation of the numerical models using experimental data has to be made using a higher number of experimental tests in order to cover the dispersion of the experimental tests.

Another important aspect about the experimental tests on the 3PB specimen is the sensitivity that the numerical models have shown to the pre-crack geometric properties i.e. length, inclination.

The mesh technique used for the crack domain is also an important fact which has to be emphasized. The numerical results of the crack propagation path under mixed mode loading cases are more accurate if the crack domain mesh is completely random. In case of the crack domain mesh is completely structured the results will not be correct.

From the experimental data it was possible to determine the stress intensity factors K_I and K_{II} and consequently calculate the equivalent stress intensity factor using four different approaches. This allow to conclude that the propagation law for the used material is not much different in cases of mixed or in cases of pure mode I. That was possible to conclude comparing the fitting curves for the original Paris law and the fitting curves for each approach used to determine the equivalent stress intensity factor.

10.2 Future Work

It has been proved that the geometries and experimental setups which has been used do not induce a high contribution of mode II. Therefore in future work new geometries and experimental setups should be tests in order to increase the mode II contribution. Also for further work a pure mode II situation will be tested using a completely different geometry and experimental setup. For this situation the fitting curve for da/dN as a function of ΔK_{II} will be compared with the fitting curve using the NASGRO database material experimental data.

An important aspect which also has to be improved in the future is to understand how the used software uses the enrichment functions to predict the crack path and be capable of explain the difference between results when it is used a structured mesh or a free mesh.

A more complete mechanical characterization of the used material should be done and in case of the material have different mechanical properties in different directions, the numerical models should be modified and the correct properties introduced.

References

[1] D. Broek, *Elementary engineering fracture mechanics*. Martinus Nijhoff Publishers, Fourth revised edition ed., 1986.

[2] M. F. Kanninen and C. L. Popelar, *Advanced fracture mechanics*. Oxford University Press, 1985.

[3] P. C. Paris and F. Erdogan, "A critical analysis of crack propagation laws," *Journal of Basic Engineering*, vol. 85, no. 4, pp. 528–533, 1963.

[4] NASA, *Fracture Mechanics and Fatigue Crack Growth Analysis Software*, version 6.1 final ed., July 2010.

[5] J. J. Newman, "A crack opening stress equation for fatigue crack growth," *International Journal of Fracture*, vol. 24, no. 4, pp. R131–R135, 1984.

[6] G. Fajdiga and B. Zafošnik, "Determining a kink angle of a crack in mixed mode fracture using maximum energy release rate, SED and MTS criteria," *Journal of Multidisciplinary Engineering Science and Technology*, vol. 2, pp. 356–362, 2015.

[7] H. Richard, W. Linnig, and K. Henn, "Fatigue crack propagation under combined loading," *Forensic Engineering*, vol. 3, no. 2-3, pp. 99–109, 1991.

[8] H. Richard, M. Fulland, and M. Sander, "Theoretical crack path prediction," *Fatigue & Fracture of Engineering Materials & Structures*, vol. 28, no. 1-2, pp. 3–12, 2005.

[9] L. Borrego, F. Antunes, J. Costa, and J. Ferreira, "Mixed-mode fatigue crack growth behaviour in aluminium alloy," *International Journal of Fatigue*, vol. 28, no. 5, pp. 618–626, 2006.

[10] K. Henn and H. Richard, "Some aspects of fatigue crack growth under mixed mode loading," in *ICF7, Houston (USA) 1989*, 2013.

[11] W.-R. Chen and L. Keer, "Fatigue crack growth in mixed mode loading," *Journal of Engineering Materials and Technology*, vol. 113, no. 2, pp. 222–227, 1991.

[12] K. Tanaka, "Fatigue crack propagation from a crack inclined to the cyclic tensile axis," *Engineering Fracture Mechanics*, vol. 6, no. 3, pp. 493 – 507, 1974.

[13] J. Eshelby, "The continuum theory of lattice defects," *Solid State Physics*, vol. 3, pp. 79 – 144, 1956.

[14] J. R. Rice *et al.*, "A path independent integral and the approximate analysis of strain concentration by notches and cracks," *Journal of Applied Mechanics*, pp. 379–386, 1968.

[15] G. Irwin, "Fracture I," *Handbuch der Physik VI*, pp. 551–590. Flügge Ed., Springer, 1958.

[16] K. Ronald, "irtual crack closure technique: history, approach, and applications," tech. rep., NASA/CR-2002-211628, 2002.

[17] R. Krueger, "Virtual crack closure technique: history, approach, and applications," *Applied Mechanics Reviews*, vol. 57, no. 2, pp. 109–143, 2004.

[18] T. Belytschko and T. Black, "Elastic crack growth in finite elements with minimal remeshing," *International Journal for Numerical Methods in Engineering*, vol. 45, no. 5, pp. 601–620, 1999.

[19] J. M. Melenk and I. Babuška, "The partition of unity finite element method: basic theory and applications," *Computer Methods in Applied Mechanics and Engineering*, vol. 139, no. 1-4, pp. 289–314, 1996.

[20] N. Moës, J. Dolbow, and T.Belytschko, "A finite element method for crack growth without remeshing," *International Journal for Numerical Methods in Engineering*, vol. 46, no. 1, pp. 131–150, 1999.

[21] S. M. Häusler, *Damage tolerance investigations of innovative metallic airframe structures*. PhD Thesis, TU Braunschweig, 2011.

[22] J. Azevedo, "Fracture mechanics using the natural neighbour radial interpolation method," master thesis, Faculdade de Engenharia da Universidade do Porto, 2103.

[23] P. M. G. P. Moreira, T. Santos, S. M. O. Tavares, V. Richter-Trummer, P. Vilaça, and P. M. S. T. de Castro, "Mechanical and metallurgical characterization of friction stir welding joints of AA6061-T6 with AA6082-T6," *Materials & Design*, vol. 30, no. 1, pp. 180–187, 2009.

[24] "Fatigue crack growth in friction stir welds of 6082-T6 and 6061-T6 aluminium alloys: A comparison,"

[25] D. Liu, H. Atkinson, P. Kapranos, W. Jirattiticharoean, and H. Jones, "Microstructural evolution and tensile mechanical properties of thixoformed high performance aluminium alloys," *Materials Science and Engineering-A*, vol. 361, no. 1, pp. 213–224, 2003.

[26] http://www.makeitfrom.com/material-properties/6082 T6-Aluminum, "Aluminum Alloy 6082-T6-Mecahnical Properties."

[27] Dassault Systèmes, "Abaqus 2016 documentation," *Dassault Systèmes Simulia Corporation*, 2015.

[28] A. A. Rubinstein, "Mechanics of the crack path formation," *International Journal of Fracture*, vol. 47, no. 4, pp. 291–305, 1991.

[29] ASTM E399, *Standard method of test for plane strain fracture toughness of metallic materials*, 1971.

[30] British Standards Institution, DD 19:Draft for development *Methods for crack opening displacement (COD) testing*, 1972.

[31] ASTM E647, *Standard test method for measurement of fatigue crack growth rates. Annual book of ASTM Standards*, vol. 3, 2000.

[32] T. Rabczuk and W. A. Wall, "Extended finite element and meshfree methods." 2006/07.

[33] J. Haigh, "The growth of fatigue cracks at high temperatures under predominantly elastic loading," *Engineering Fracture Mechanics*, vol. 7, no. 2, pp. 271–284, 1975.

[34] E. Hedayati and M. Vahedi, "Using extended finite element method for computation of the stress intensity factor, crack growth simulation and predicting fatigue crack growth in a slant-cracked plate of 6061-T651 aluminum," *World Journal of Mechanics*, vol. 2014, 2014.

[35] P. M. S. T. de Castro, "Notas sobre a análise linear elástica do estado de tensão e deformação de sólidos contendo fendas," 2017.

[36] H. A. Richard and M. Sander, *Fatigue Crack Growth*. Springer, 2016.

[37] S. Häusler, K. Lindhorst, and P. Horst, "Combination of the material force concept and the extended finite element method for mixed mode crack growth simulations," *International Journal for Numerical Methods in Engineering*, vol. 85, no. 12, pp. 1522–1542, 2011.